DESIGN AND MICROSCOPIC INVESTIGATION OF THE GROWTH AND ELECTRONIC STRUCTURE OF LOW-DIMENSIONAL HETEROINTERFACES

By

Xi Dong

A DISSERTATION

Submitted to
Michigan State University
in partial fulfillment of the requirements
for the degree of

Physics – Doctor of Philosophy

2022

ABSTRACT

DESIGN AND MICROSCOPIC INVESTIGATION OF THE GROWTH AND ELECTRONIC STRUCTURE OF LOW-DIMENSIONAL HETEROINTERFACES

By

Xi Dong

In the quickly advancing world of material synthesis and processing, finer gauges are being developed for controlling dimensionality and constitutions of the materials. Apart from their bulk counterparts, remarkable physics has been demonstrated with the reduction of dimensionality, such as creation of zero-dimensional quantum dots with designed bandgap, one-dimensional (1D) nanotubes with excellent thermal and electrical conductivity and two-dimensional (2D) monolayer with direct bandgap, etc. Furthermore, incorporations of these materials into heterostructures (HSs) by bringing dissimilar constituents together, not only offers an opportunity to tune the structure and strength of the existing electronic properties of each constituent, but also of the capacity to generate novel electronic properties. Understanding the interfacial interactions holds a crucial role in tackling the origins of these changes which creates a strong desire for controlled synthesis of HSs and local investigation of the interfacial phenomenon.

In the low-dimensional (LD) solid-state systems, depending on the configurations of the HSs (lateral or vertical), interfacial phenomenon that is confined within a few atomic layers, or a few atoms/molecules are readily available for probing by surface-sensitive techniques due to their limited sizes. To properly interpretate the origins of morphological alterations and electronic perturbations in a HS, both high-quality samples and microscopic characterization tools are required. Sample quality must be controlled to reduce the unintentional modification of the sample property. For that, molecular beam epitaxy (MBE) and organic molecular beam epitaxy (OMBE) are employed in our studies. They have excellent control on the growth parameters that fine tune

the growth rate and growth kinetics. They can deposit high-quality thin films with sub-monolayer precision and create HSs from sequential depositions. Later, high-resolution scanning tunneling microscopy/spectroscopy (STM/STS) is utilized to connect the dots between the atomically resolved local morphology and the electronic structure perturbation which improves our understanding of the interfacial phenomenon.

In this dissertation, we will investigate various HSs constructed with inorganic and organic thin films to demonstrate the crucial importance of the interfacial effect in tuning, selecting, and creating of the desired electronic structures in the LD systems. Different phase engineering and property tunning techniques will be revealed and connected to the interfacial influence by our selected studies. The first study will focus on probing the thin film growth morphology from tunning the strength of the interfacial interaction with the substrate. The second study will explore a new technique that incorporate the phase transition with the 2D lateral core-shell HSs construction which creates an interesting topological insulator and superconductor pair for future investigation. The third study will investigate an organic charge transfer complex HS, which offers more microscopic evidence for the macroscopic phase transition in bulk. Better understanding of the interfacial effect from our studies could contribute to the logical choice of the constituents for the HS construction and rational modification of the substrate interactions for high-quality thin film growth. In the last study, we will employ the knowledge of previous studies and aim to create a high-quality HS system which induces superconductivity in a semiconductor thin film.

ACKNOWLEDGEMENTS

My gratitude to all the people who offer constant support to make this work possible.

First, I would like to thank my advisor, Dr. Pengpeng Zhang, for the guidance and the opportunities you provided throughout my graduate school years. Your support and mentoring are invaluable.

I want to thank Dr. Lizhi Zhang, Dr. Mina Yoon, and Dr. Wei Lai for your supports in providing the theoretical calculations and insightful discussions.

I would also like to thank my guidance committee, Dr. Scott Pratt, Dr. Stuart Tessmer, Dr. Kirsten Tollefson, Dr. Chong-Yu Ruan for your helpful guidance and suggestions.

I want to thank Kim Crosslan for helping me navigate the administrative works. I also want to thank Reza Loloee for providing supports and troubleshooting ideas for the equipment. Your help made my life a lot easier.

I want to thank Andrew Tan and Timofey Golubev for navigating the lab and transferring their valuable experiences and knowledge to get me through the research. I am thankful for Tim's great friendship and your companions for those wonderful fishing trips which offered much-needed release from the stress.

I am grateful for the help in coursework and companions of my fellow graduate students, Tong Li, Mengzhi Chen, Heda Zhang, Chunqiang Xu, Alexander Madden, and more.

At last, I would like to thank my family, Biyue Cheng, Baoping Dong, Xiumei Dong, Xiuting Dong and Luke Dong for your love and support throughout my life.

TABLE OF CONTENTS

LIST OF TABLES .... **vii**

LIST OF FIGURES .... **viii**

1 Introduction and Work Layout **1**

2 Experimental Techniques **17**
- 2.1 Experimental Apparatus and Growth Mechanism 17
  - 2.1.1 Experimental Apparatus 17
  - 2.1.2 Thin Film Growth Mechanism 20
  - 2.1.3 Substrate Preparations 23
  - 2.1.4 Organic and Inroganic Thin Film Deposition 26
- 2.2 Scanning Tunneling Microscopy and Spectroscopy 29
  - 2.2.1 Quantum Tunneling 29
  - 2.2.2 Operation Modes for Scanning Tunneling Micrscopy 34
  - 2.2.3 Scanning Tunneling Spectroscopy 36
  - 2.2.4 Differential Conductance Mapping 37
  - 2.2.5 Considerations and Complications in the STS Measurement 38
- 2.3 Density Functional Theory 47
  - 2.3.1 Introduction 47
  - 2.3.2 The Hohenberg-Kohn (HK) Theorems 48
  - 2.3.3 The Kohn-Sham (KS) Equations 48
  - 2.3.4 Exchange Correlation Approximation 50
  - 2.3.5 Structural Relaxation 51

3 The Role of Substrate on Stabilizing New Phases of Two-Dimensional Tin **54**
- 3.1 2D Sn Growth on Ir(111) 58
- 3.2 2D Sn Growth on Pre-deposited h-BN Monolayer on Ir(111) 61
- 3.3 $\sqrt{7} \times \sqrt{7}$ Superlattice – A New Phase of 2D Sn 66
- 3.4 Discussion 70
- 3.5 Conclusion 72

4 Semiconductor to Topological Insulator Transition Induced by Stress Propagation in Metal Dichalcogenides Core-Shell Lateral Heterostructures **73**
- 4.1 Observation of H to T′ Phase Transition in WSe_2 Core 74
- 4.2 Investigation of Charge Transfer Behaviors by STM/S 77
- 4.3 First-principles Calculations of Boundary Morphology and Electronic Structures 82
- 4.4 A New Phase Transition Mechanism in Core-shell Architecture 84
- 4.6 Conclusion 89

5 Spatially Resolved Investigation of Mixed Valence and Insulator-to-Metal Transition in an Organic Salt **91**
- 5.1 Self-assembly and Electronic Structure of TCNQ on HOPG 92

5.2 Self-assembly and Electronic Structure of K-TCNQ on HOPG 95
5.3 TCNQ and K-TCNQ Lateral Heterostructure 96
5.4 Discussion 102
5.5 Conclusion 103

6 Investigation of $SnSe_2$ on $SrTiO_3$ (STO) Surface 104
6.1 Spatially Inhomogeneous Charge Transfer in $SnSe_2$/3 × 3 Reconstructed STO(111) . 105
6.1.1 STO(111) Surface Reconstuction and Local Electronic Variation 108
6.1.2 Growth Morphology of $SnSe_2$ on 3 × 3 RC STO(111) 112
6.1.3 Distance Dependent Evolution of $SnSe_2$ Electronic Structure 115
6.1.4 Strain Effect 118
6.1.5 Discussion and Conclusion 122
6.2 Investigation of $SnSe_2$/WSe_2/STO(111) Vertical Heterostructure 123
6.2.1 WSe_2 Deposition on STO(111) 123
6.2.2 $SnSe_2$ Deposition on WSe_2 Covered STO Substrate and Future Perspectives 127

7 Conclusion and Future Prospects 130

BIBLIOGRAPHY 131

LIST OF TABLES

Table 3-1: Calculated formation energies for different configurations of Sn.............................. 65

Table 5-1: Summary of position and FWHM (full width half maximum) of LUMO peak obtained from Gaussian fitting of the twenty normalized *dI/dV* spectra shown in Figure 5-3................. 101

Table 6-1: CBM variations of the STO(111) surface 111

Table 6-2: Lattice and strain variation on the uneven $SnSe_2$ film.. 120

LIST OF FIGURES

Figure 1-1: Heterostructure arrangements and interfacial effect 2

Figure 1-2: Band structures of monolayer MoS_2 at different lattice constants. Adapted from [19]. 3

Figure 1-3: Various quantized Hall effects 5

Figure 1-4: Energy and structural stability relationship 9

Figure 1-5: Low-buckled stanene crystal structure and electronic property variation from chemical decoration and strain. Adapted from [53] 12

Figure 1-6: Electronic and geometric corrugations of the h-BN on Ir(111) substrate. Adapted from [76] 13

Figure 1-7: The insulating and conducting state of K-TCNQ triggered by electric field. Adapted from [83] 15

Figure 2-1: Experimental apparatus 17

Figure 2-2: Schematic for Molecular Beam Epitaxy chamber 19

Figure 2-3: Kinetic processes and growth modes 20

Figure 2-4: Picture of ion gun setup and borazine leak valve and ion gun ionization module..... 24

Figure 2-5: Moiré pattern from two identical patterns with small rotational angles 25

Figure 2-6: Chemical formula of borazine and ammonia borane and the ammonia borane powder vessel. 26

Figure 2-7: Tunneling mechanisms 30

Figure 2-8: Schematic of STM and two operation modes 36

Figure 2-9: Charge transfer and band bending 39

Figure 2-10: Extraction of VBM and CBM from the STS curves 42

Figure 2-11: Negative Differential Resistance (NDR) 44

Figure 2-12: Example superconducting STS spectrum of Pb and vortex imaging of $NbSe_2$ 47

Figure 3-1: Side views of the charge density differences for Sn adlayers on different substrates 56

Figure 3-2: The integrated charge density differences for Sn/h-BN, Sn/h-BN/Ir(111) and Sn/Ir(111) systems 57

Figure 3-3: Electronic band structures projected onto the Sn atoms on three different substrates, Ir(111), h-BN, and h-BN/Ir(111) 58

Figure 3-4: Sn growth morphologies and electronic property on Ir(111) 59

Figure 3-5: Top and side view of bilayer stanene on Ir(111) surface 61

Figure 3-6: Morphology and electronic properties of h-BN/Ir(111) 62

Figure 3-7: Sn growth morphologies on h-BN/Ir(111) and band structure 63

Figure 3-8: Buckled square-like (b-square) Sn on h-BN/Ir(111) at different imaging biases 64

Figure 3-9: Registry and continuity of $\sqrt{7} \times \sqrt{7}$ Sn on h-BN/Ir(111) 65

Figure 3-10: Size and temperature dependent of Sn phases on h-BN/Ir(111) 66

Figure 3-11: $\sqrt{7} \times \sqrt{7}$ Sn on h-BN/Ir(111) at different bias voltages 67

Figure 3-12: Representative STS curves at various locations of Sn adlayer on h-BN/Ir(111) 69

Figure 3-13: Band structure evolution of $\sqrt{7} \times \sqrt{7}$ Sn with strain 71

Figure 4-1: Phase transition in $SnSe_2$-surrounded WSe_2 islands 75

Figure 4-2: Bias-dependent apparent height measurements on the same core-shell structure 76

Figure 4-3: STS spectra taken on the interiors of 1H-WSe_2 and 1T-$SnSe_2$ on HOPG 78

Figure 4-4: Electronic structures and band bending behavior near boundaries of 1H-WSe_2 and 1T-$SnSe_2$ 79

Figure 4-5: Impacts of misfit dislocation on morphologies and electronic states of 1H-WSe_2/1T-$SnSe_2$ and 1T′-WSe_2/1T-$SnSe_2$ boundaries 81

Figure 4-6: Theoretically extrapolated band alignment from PDOS analysis in Figure 4-5(e) 83

Figure 4-7: Mechanism of stress propagation for phase transformation of WSe_2 85

Figure 4-8: Topological edge state of 1T′-WSe_2 87

Figure 4-9: Topological edge state on the 1T′-WSe_2/1T-$SnSe_2$ boundary with structural perturbations from misfit dislocations 89

Figure 5-1: Morphology and electronic structures of TCNQ self-assembly on HOPG 93

Figure 5-2: Morphology and electronic structures of K-TCNQ self-assembly on HOPG 96

Figure 5-3: Morphology and electronic structures of TCNQ:K-TCNQ heterostructure on HOPG 97

Figure 5-4: Assignment of molecule and K locations in K-TCNQ assembly and TCNQ : K-TCNQ heterostructure. Bias-dependent STM images of K-TCNQ.. 98

Figure 6-1: Crystal structure of STO(001), STO(110) and STO(111). Adapted from [241] 106

Figure 6-2: Polar compensation mechanism by surface reconstruction and 4 × 4 surface reconstruction of STO(111). Adapted from [253] 107

Figure 6-3: Substrate morphology and work function variations on this substrate 109

Figure 6-4: Temperature dependent four-probe resistance measurement for UHV treated STO(111) samples.. 111

Figure 6-5: Sub-monolayer growth morphology and layer dependent growth rate.................... 113

Figure 6-6: Characterization of growth morphology of $SnSe_2$ on STO(111)............................ 113

Figure 6-7: Charge transfer and band bending evolution at a partially connected island........... 116

Figure 6-8: Strain variation on the as grown $SnSe_2$ film within the same terrace...................... 119

Figure 6-9: Lattice constant measurement... 120

Figure 6-10: Surface reconstruction after Ar sputter and annealing... 124

Figure 6-11: Temperature and coverage evolution of WSe_2 morphology on STO(111)............ 125

Figure 6-12: Electronic structure of different phase of WSe_2 on STO(111) 126

Figure 6-13: $SnSe_2$ deposition on WSe_2 covered STO substrate... 127

Figure 6-14: Emerging of local CDW on $SnSe_2$ on WSe_2/STO(111) 128

1 Introduction and Work Layout

In the goal of shrinking technologies, there is a strong desire to incorporate more functions into smaller packages to create devices of lower cost and power consumption. Immense attention has been drawn towards researching materials in nanoscale size which have triggered fast technological advancement in material synthesis and processing. As the dimensions of a device shrink, quantum mechanics becomes more essential in determining the material's properties. Organic and inorganic materials with their essential properties that cannot be described by semiclassical particles and low-level quantum mechanics are categorized as "quantum materials".[1] Quantum materials could present strong electronic correlation or ordering (e.g. superconducting/magnetic ordering) or non-generic quantum effects (e.g. topological matters), and genuine quantum effects (e.g. ultra-cold atoms) which significantly enrich the physical properties for fundamental research and functionalities in device fabrications.[1]

In solid state systems, the devices are often empowered by the interface which is typically limited to a few atomic layers or a few atoms with their properties generally different from their bulk counterparts. This spawned new subfields in solid state physics focusing on the study of the surfaces and interfaces. As low-dimensional (LD) materials are essentially the interface, their properties are crucially dependent on the interfacing materials (e.g. substrate or another LD material from heterostructure (HS) construction).[2, 3] In contrast to the conventional bulk HS where the interface is buried deep, the surface and interface in the LD systems are exposed, enabling direct and microscopic investigation of the interfacial phenomena which provides a basis for the understanding of the origins of the novel properties arising from rational HS design.[3]

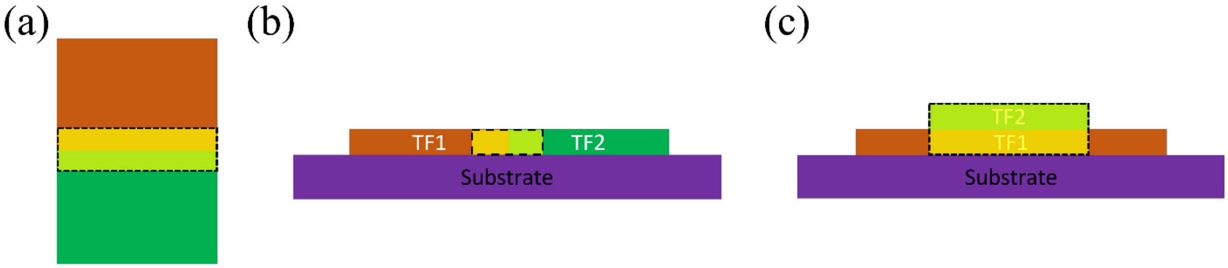

Figure 1-1: Heterostructure arrangements and interfacial effect
(a)Bulk HS with buried interface (b) Lateral HS constructed from two thin films: TF1 and TF2 placing on top of a bulk substrate. (c) Vertical HS constructed from two thin films. The dash line approximately outlines the interfacial effect regions without considering the substrate effect. The interfacial effect region is buried deep for (a). In (b-c), the region is more accessible. The physical "interface" for the 2D lateral HS refers to the edge boundary.

In the lateral HS, we can conveniently investigate the distance dependent electronic structure evolution near the interface as shown in Figure 1-1. On the contrary, only discrete increments can be achieved from the vertical HS by increasing the number of layers which could also change materials' electronic properties. For example, in some TMDs, the bandgap structure changes from direct to indirect as the thickness increases beyond a monolayer which has a significantly impact on their optical properties.[4] Weak substrate interaction can be achieved from the usage of van der Waals (vdWs) layered materials. These layered materials have weak interlayer coupling and strong intralayer coupling (covalently bonded), such as graphene, h-BN and TMDs. They are usually easy to exfoliate. Due to weak substrate interactions, stacking them vertically form an atomically smooth interface which significantly reduces the properties perturbations induced by strain and interfacial defects. Consequently, vertical HSs are intensely explored in device applications.[5] For the same reasons, current interests for the lateral HSs are focused on achieving coherent boundary from materials with similar lattice constants to prevent electronic perturbations from local strain or local defect states.[3]

The novel properties generation from rational HS design are valid for both organic and inorganic materials. For the inorganic system, an archetypal example is the emerging of conductivity, superconductivity, magnetoresistance, or ferromagnetism at the interface of non-magnetic oxides insulators.[6-9] Meanwhile, organic systems constructed from single molecular species that are typically unipolar and semiconducting could exhibit rich properties ranging from Mott insulator, metal, superconductor, ferroelectric, to (anti) ferromagnetic, after staking the donor and acceptor molecular species in mixed or segregated fashions into charge transfer complexes (CTCs).[10-13] At interfaces, structural modification and electronic intertwining, such as strain,[14] charge transfer,[15] Moiré pattern,[16] electron-phonon coupling,[17] and proximity effect[18] can play both beneficial and detrimental roles on harnessing the desired properties. It is crucial to control and study the interfacial effects in the systems of interest. Figure 1-2 shows an example of quasiparticle band structure evolutions with strain.

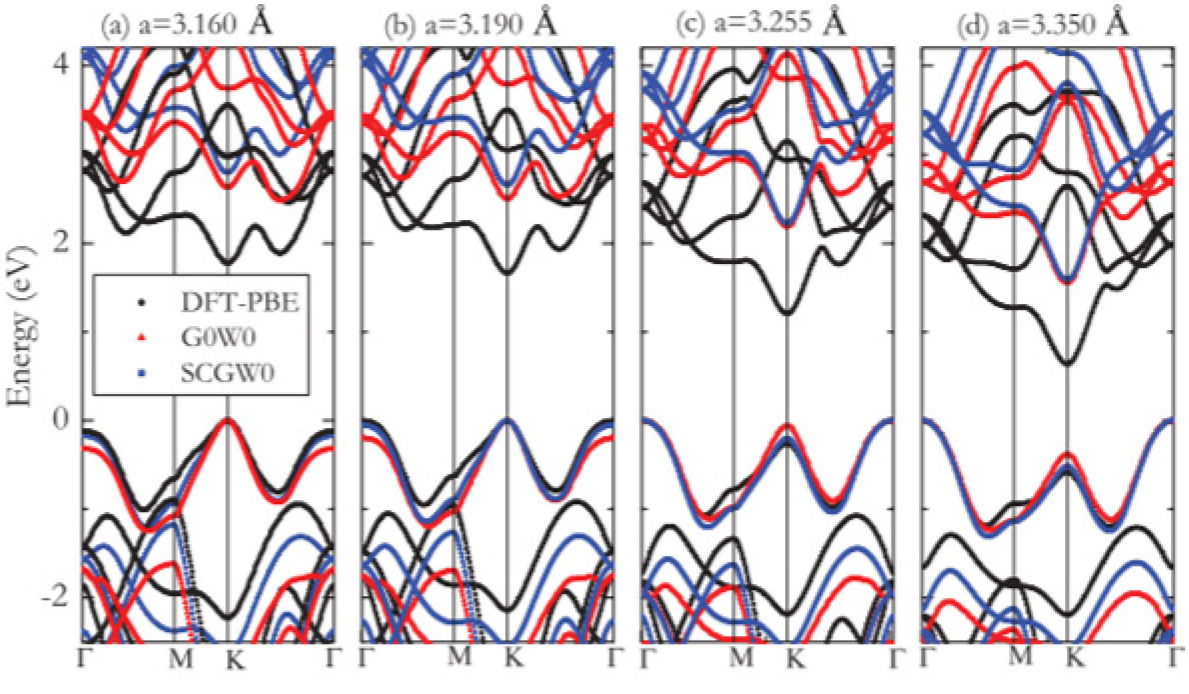

Figure 1-2: Band structures of monolayer MoS_2 at different lattice constants. Adapted from [19]

(a)0%, (b)1%, (c) 3% and (d) 6% tensile strained MoS_2 electronic band structure calculated by DFT, G_0W_0, and $SCGW_0$, respectively.

Recently, immense attention has been drawn to newly emerging topological materials for the inorganic systems. In this group of materials, fundamental properties are determined by a topological invariant, which includes gapped materials like topological insulators,[20-22] topological crystalline insulators,[23] and gapless materials like Dirac and Weyl semimetals,[24] etc. In topology, topological equivalence implies some macroscopic observable properties are not changed within the same order. For example, the 2D surface in a 3D object can be classified topologically. Two surfaces are topologically equivalent if they can be smoothly deformed into each other. An orange and a bowl are topologically equivalent because an orange can be shaped into a bowl by squishing it. Similarly, a donut is topologically equivalent to a coffee cup where the hole in the middle of the donut can become the handle after smooth deformation. However, an orange cannot be deformed into a coffee cup without cutting a hole. Cutting a hole is not a smooth deformation, therefore, they are topologically inequivalent. Across the boundary of materials with different topological invariants, the observable properties must change which induce exotic phenomena that are promising in the applications of dissipationless electron transport, spintronic devices and quantum information technology in the solid-state systems.[25-31]

The first example of a topological phase is the integer quantum Hall effect (QHE) which is a quantized version of the Hall effect. The QHE was first observed by K. von Klitzing. et al. in 1980 which won him the Nobel Prize in 1985.[25] In a high-quality sample possessing two-dimensional electron gas (2DEG) that is under extremely low temperature and high magnetic field perpendicular to it, the Hall conductivity is quantized proportionally to e^2/h, where “e” is the elementary charge and “h” is the Planck constant.[25, 26] For simplicity, this QHE can be understood by a toy model as shown in Figure 1-3(a). In the bulk of the 2DEG, it is insulating due to the Landau levels arising from the cyclotron motions under the strong perpendicular magnetic field. At the edges, unidirectional chiral edge states are formed from the skipping orbitals at the boundary to the vacuum. The number of quantized conduction channels at the edge are proportional to the number of crossings between the Fermi Level (FL) and the Landau levels as well as the quantum invariant known as the Chern number.[26, 32] In the topological point of view, the exotic quantized phenomenon is a result of the crossing between the sample and vacuum which have different topological orders. With the discontinuity of topological order at the boundary, the macroscopic properties (i.e. the bandgap) must change, which results in a conducting edge. Although the unidirectional chiral edges enable the possibility for electron transportation without dissipation, the requirements of these extreme conditions including high sample quality, low temperature, and high magnetic field have severely limited its applications.

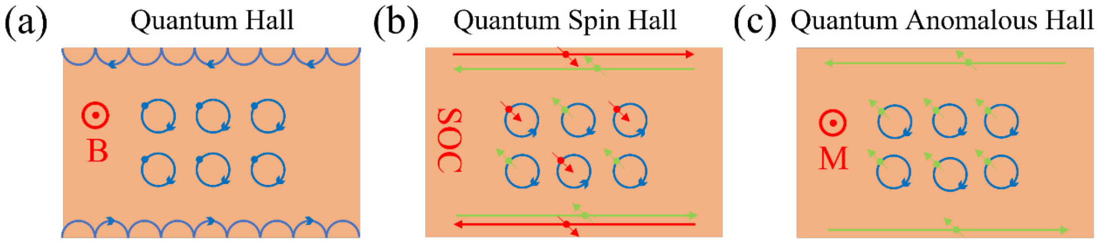

Figure 1-3: Various quantized Hall effects
(a) Quantum Hall Effect (b) Quantum Spin Hall Effect (c) Quantum Anomalous Hall Effect

Based on the model of the QHE, the concept of topological insulator (TI) was introduced by C. Kane and E .J. Mele’s group and B. A. Bernevig and S. C. Zhang’s group separately in 2005 and 2006.[27, 28] Similar to the effect of a high magnetic field in a clean sample with 2DEG, the spin-orbit coupling (SOC) acting as an “effective magnetic field” is responsible for both bulk bandgap opening and band inversion. In its boundary with a conventional insulator, helical edge states are expected with the spin up and down electrons traveling in opposite directions due to SOC induced spin-momentum locking and the protection by time reversal symmetry (TRS). With a single Kramer pair, TRS prevents electron backscattering by nonmagnetic impurity (i.e. the elastic transition between k to -k momentum), as it would involve flipping the spins simultaneously. One year later in 2007, the first TI was realized in HgTe/CdTe semiconductor quantum wells by M. Konig et, al.[20] They observed a quantized conductance of $\sim 2e^2/h$ in a two-terminal transport measurement, confirming the existence of the helical edge states.[20] This spin version of the quantum Hall effect is then referred to as the quantum spin Hall effect (QSHE) with its toy model shown in Figure 1-3(b). The concept of a TI was expanded into 3D by L. Fu. et, al. in 2007.[21] In 3D, the boundary changes from a 2D edge to the 3D surface. At the surface of a 3D TI, massless helical spin polarized surface states that disperse linearly in the momentum space form a Dirac cone.[22] This phenomenon was first observed in $Bi_{1-x}Sb_x$ alloy by D. HSiet et, al. in 2008.[22] It is important to notice that to properly use the boundary states of TI for electron transport, the electrons should not leak into bulk bands. As a counterexample, graphene was predicted to be a topological insulator with inclusion of the SOC.[33] Nonetheless, SOC is very small with carbon element (~4meV) which opens up a gap of $\sim 10^{-3}$meV at the Dirac point.[34] Thus, experimental realization of QSH effect in graphene is nearly impossible. Ideally, for room temperature application, the bandgap of a TI needs to be much larger than the room temperature (RT) thermal fluctuation (~26meV). A large gap also helps locate the FL well inside the bandgap to prevent activating the bulk conducting states that overwhelms the boundary state contribution in transport.

Interfacing the exotic boundary states of a TI with another topological trivial phases of matter provides both an opportunity and a challenge. It can produce more novel and exotic electronic states and quasiparticles, which are difficult to access in a topologically trivial system.[35-39] Meanwhile, although TI is robust under adiabatic perturbation without “closing of the bandgap”,[27, 28] the structural and electronic effect due to the interfacial interactions that are mentioned earlier should not be neglected. For example, if a significant strain is present, the bandgap can be closed which changes its topology.[14, 19, 40] Charge transfer can also shift the FL outside the bandgap to activate the bulk conducting states.[15]

It is easy to see the opportunities. For example, a long-ranged ferromagnetic ordering can be introduced to the QSHE to keep only one set of chiral edge states of a particular spin to realize the Quantum Anomalous Hall Effect (QAHE) as shown in Figure 1-3(c).[41] Similar to the QHE, the QAHE can quantized charge and spin hall conductance without the requirement of a strong external magnetic field, where in QSHE only have quantized spin hall conductance and zero charge hall conductance. The QAHE was first achieved from the chromium-doped $(Bi,Sb)_2Te_3$ alloy that effectively formed a 3D magnetic topological insulator.[42] Meanwhile, achieving a long-range magnetic order by doping in 2D is challenging, since the Mermin-Wagner theorem prevent the long-range ordering of spin in an isotropic 2D system.[43, 44] Other than doping, this long-range magnetic coupling can be also introduced into TIs via the proximity effect through interfacing with a topological trivial material with well-defined magnetic properties.[45, 46] Nonetheless, the experimental realization of QAHE based on HS construction remains difficult due to perturbations from previous mentioned interfacial effects.[47-49] .

Moreover, interfacing the TI with a conventional superconductor could induce superconductivity in the TI by the proximity effect, which can lead to novel topological phases like topological superconductivity, Josephson effect and unconventional Pearl vortices.[35-37] Intriguingly, Majorana bound states were predicted from the proper HS design from both 3D and 2D TIs.[38, 39] The Majorana fermion is its own anti-particle introduced by E. Majorana in 1937. It was predicted and measured in different 3D TI and s-wave superconductor HS systems,[50] while the experimental realization of chiral Majorana edge mode constructed from a QAHE and superconductor HS system remains controversial.[51, 52] Due to the non-abelian nature of the Majorana fermion, it is predicted to be an important ingredient for fault-tolerant quantum computing.[30, 31]

In 2D HSs, structural modifications originating from the interfacial interactions are more prominent.[40, 53] In addition to the strain effect mentioned earlier, structurally, thin films are more prompt to assume metastable phases that were previously difficult to access.[54, 55] Owing to the different crystal structures, materials with different phases vary significantly in both physical and electronic properties, i.e., structure control is property control. A paradigmatic example of phase structure is bulk carbon, which in its diamond form (space group $Fd\bar{3}m$) is an insulator and in its graphite form (space group $P6_3/mmc$) is a conductor.[56] Different phases have different energies, some are nearly degenerate, some are almost experimentally infeasible.[54, 55] The notion of stability is important for the discussion of the structural phases as shown in Figure 1-4. Under the right conditions, it is possible to observe some long-lived metastable phase that has higher energy than the ground state phase. In the case of carbon, the metastable diamond having higher energy than graphite can be formed under high pressure.[57] Once enough time and energy are given to overcome the energy barrier, it can revert back to its graphite form. In general, in the process of phase transition (e.g. switching between stable and metastable structure), various methods can be employed to overcome the energy barrier, such as charge transfer, external irradiation, thermal treatment and external stress.[54, 55] Due to being lowest in energy, the thermodynamically stable phases are typically most abundant in nature.

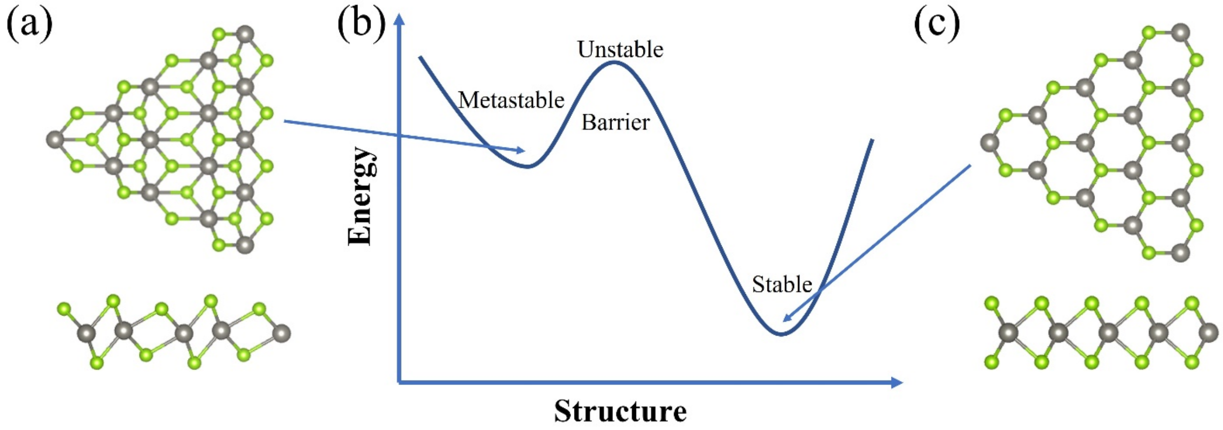

Figure 1-4: Energy and structural stability relationship
In terms of energy, the stable phase of a materials sits at the global minimum. A metastable phase sits at local minimums. To generate phase transition, the energy barrier between the phases will need to be overcome. (a,c) top and side views of the crystal structures of 1T′-WSe_2 and 1H-WSe_2, respectively. In this layered TMD, the metal atoms are sandwiched in between the chalcogenides by covalent bonding. As no dangling bonds exist, the interlayer interactions are mainly Van der Waals like. The 1H-WSe_2 more thermodynamically stable while the 1T′-WSe_2 is metastable.[58]

Similar to its bulk counterparts, phase engineering in 2D systems can be exerted via controlling related processing environments such as temperature, pressure, reaction atmosphere, etc.[54, 55] But surface effects (e.g., substrate interactions, thickness influence) will start to play more significant roles. Strain (i.e. pressure) induced from lattice mismatching and charge transfer from work function misalignment are two examples of stabilizing factors for the emergence of rich metastable phases. These metastable phases offer many novel and exotic electronic properties derived from rich physical structures. [54, 55] Recent theoretical predictions have shown that some group IV (Si, Ge, Sn) graphene-like sheets and metastable T′ phase of single layer TMD are 2D TIs.[53, 59-64] Among them, stanene which is the Sn analogue of graphene, and 1T′-WSe_2 are most interesting due to their relatively larger bandgap (~100 meV).[53, 60-64] However, accessing these metastable phases while preserving their intrinsic properties is still challenging. Experimentally, it is challenging to synthesize large high-quality sample of metastable phases for transport (i.e. Hall conductivity) measurement. [54, 55] Nonetheless, main evidences of QSHE such as band inversion and observation of linearly dispersive edge states inside bulk bandgap that are robust against non-magnetic perturbations can still be verified from combined investigations of STM/S, angle-resolved photoemission spectroscopy (ARPES) and Density functional theory (DFT) calculation for the samples with limited sizes.[62, 63, 65-67] However, a proper choices of the substrate is still needed in the latter case. For example, the first experimental realization of stanene was grown on Bi_2Se_3 substrate, the film became metallic due to a slight compressive strain.[65, 66] For the 1T′-WSe_2 monolayer on weakly interacting graphene substrate, the combined investigations have revealed a ~2nm spatial extension of the topological edge state inside the bulk bandgap. [62, 63, 67]

While there is no upper limit for the film size, the lower limit for the observation of the QSHE is mainly determined by the spatial extension of the topological edge states. Depending on the materials the extension of the topological edge states can vary significantly from material to material and scales inversely with the momentum space edge state dispersion.[68, 69] Therefore, if the edge states are more localized (extended) in momentum space, then the edge state spatial extension in real space is very long (short). For example, the edge state is very localized in momentum space for the HgTe system which result in a real space edge state extension of ~50nm.[68] On the other hand, the edge states extended over the entire Brillouin Zone for the Bi(111) 1-bilayer system and, the spatial extension is limited to only a few lattice constants.[68] This behavior is oddly different for the electronic states originating from the defects and impurities which are subjected to Anderson localization.[70] If the spatial extension of the edge states is very large, then the sample dimension needs to be large to prevent the bandgap opening by hybridization of the topological protected states from the opposite sides.[69] For practical observation of the edge state in experiment, the island domain size and the thickness will need to be large enough in the 2D TI and 3D TI systems, respectively, which gives additional constraints for the sample preparation.

For the purpose of devices design comprised of HS of LD materials, in additional to the selection of the desired functionalities, the quality of the films and heterointerfaces are also crucial. Thus, the main challenge of this study is to control the synthesis of desired thin film phases while pursuing favorable electronic properties. Both high-quality sample preparation methods and microscopic characterization tools are needed for the proper investigations of intrinsic interfacial phenomena. Molecular beam epitaxy (MBE) is employed to establish inorganic thin film HS growth with sub-monolayer precision while establishing fine control on the growth parameters to maximize the possibility of phase control. Organic samples are created in a similar manner by the evaporation and self-assembly of high purity organic molecules under UHV onto a substrate. After growth, the sample is transferred *in-situ* to a scanning tunneling microscope for non-invasive and high-resolution investigations of local morphology and electronic properties. These main experimental techniques and sample preparation methods are introduced in Chapter 2.

The substrate is indispensable for LD material systems. In fact, if the interaction strength with the substrate can be controllably tweaked, a phase selection of the thin film growth could be established. This effect is often more dramatic for materials with high structural adaptability (i.e. different phases has nearly degenerate energies). 2D Sn thin film is a material with high structural adaptability. Low-buckled honeycomb stanene[53] and dumbbell stanene,[71] are examples of theoretically proposed Sn structures. The physical properties of the Sn thin films are expected to be sensitive to interfacial charge transfer, strain, etc. For the low-buckled honeycomb stanene, theoretically, it is predicted to be a large gap TI.[53] Experimentally, its electronic property has been found to be very different from experiment to experiment, with some are metallic [65, 72] and others are trivial insulators.[73] Factors like substrate hybridizations, strain,[53, 66] and thickness[74] are all found to modulate the electronic property of Sn films, sensitively. Figure 1-5 shows effects of the strain and chemical decoration on the electronic structure of low-buckled honeycomb stanene.

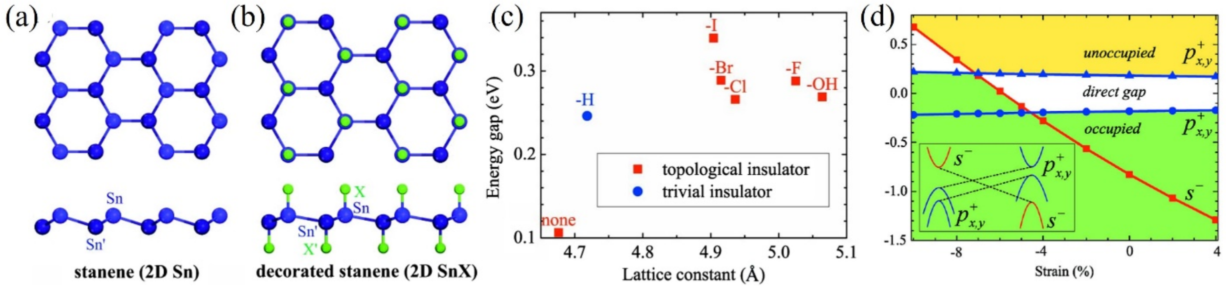

Figure 1-5: Low-buckled stanene crystal structure and electronic property variation from chemical decoration and strain. Adapted from [53]

(a) Theoretically calculated low-buckled stanene crystal structure. The structure is slightly buckled due to structure stabilization by the mixture of sp^2-sp^3 hybridization. (b-c) Decoration of the stanene with different chemical elements and its effect to lattice constant and topology. (d) The effect of the strain on band inversion and change of topology.

From the transport point of the view, the supporting substrate for a 2D TI, should be insulating to prevent overwhelming of the substrate conducting channels. In Chapter 3, we will investigate the role of substrates in determining the morphologies and electronic structures of two-dimensional (2D) Sn. The monolayer h-BN with ~6eV bandgap is utilized to mediate interfacial interaction which tunes the structure and electronic properties of the Sn thin film overlayer. h-BN on metals are highly versatile templates for site-selective absorption and electronic patterning of atoms, molecules, and nanostructures.[75] The geometry and electronic corrugation of the h-BN/metal systems depend critically on the choice of the metal substrates and the h-BN and substrate interaction strength.[75] Substrates like Iridium, which is in the regime of the intermediate interaction strength, a platform that is both electronically and geometrically corrugated will be created. A schematic of such corrugations is shown in Figure 1-6.[76]

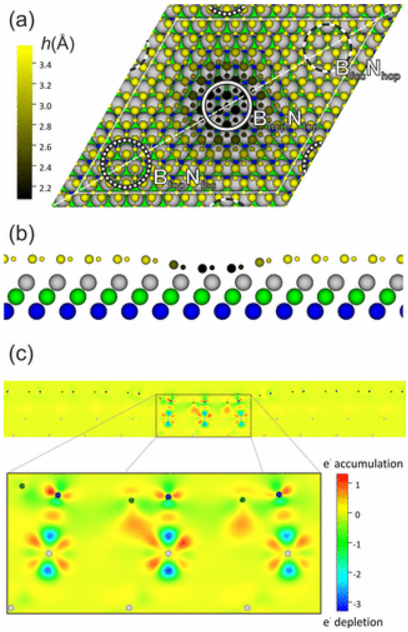

Figure 1-6: Electronic and geometric corrugations of the h-BN on Ir(111) substrate. Adapted from [76]
(a-b) Top and side view of the h-BN/Ir(111) substrate. The surface is geometrically corrugated with the pore area sitting more closely to the metal substrate than wire areas. In the pore and wire areas, the degree of charge transfer is significantly different as shown on (c). In the pore area, the h-BN is also commensurate to the Ir surface due to structural distortion.

In Chapter 3, we will demonstrate a new 2D Sn phases stabilized by the h-BN/Ir(111) substrate and explain the origins of this structural changes with the aid of the theoretical DFT calculations. In this pathway, a vertical h-BN/metal HS is constructed to manipulate the interaction strength between the Sn film and the substrate. Although physical structure and electronic structure tuning are demonstrated in this experiment, it remains difficult to control the delicate balance between them to achieve a topologically non-trivial system.

To minimize the substrate interactions which may perturb the electronic structures, in Chapter 4 and 5, we will study both organic and inorganic lateral HSs on a weakly interacting substrate (HOPG).

In fact, the lattice mismatching and the correlated strain are not always detrimental in a lateral HS. In Chapter 4, we will demonstrate a beneficial application of the strain in the field of phase transition from investigating the $WSe_2/SnSe_2$ lateral core-shell architecture on HOPG substrate. A new phase transition mechanism will be proposed based on the evidence provided by the experimental results and theoretical calculations. The topological edge state inside the 1T′-WSe_2 core will be shown to be robust against periodic local interfacial perturbations. With the directly exposed heterojunction and the superconductivity properties of $SnSe_2$ induced by interfacial charge transfer with HOPG, we now have a unique template for future investigations of superconducting proximity effect at the topological edge of a 2D TI which warrants further study. This mechanism is presumably applicable to other vapor deposition methods and offers new insights into TMD phase transition from the rational design of heterostructures. Additionally, the shell structure also offers additional protection to the core edge in ambient applications.

At last, interfacial interactions are also capable of inducing dramatic effects on organic molecules, such as previously mentioned exotic properties in CTCs. CTC molecular crystals with effective half-filled bands, including those with native quarter filled bands but strong dimer structure, are correlated electron systems due to strong on-site Coulombic repulsion (U).[77-84] When U is larger than the bandwidth W, localization of electrons on respective molecules gives rise to the Mott insulating state. These correlated CTC systems can undergo Mott insulator-to-metal transition (IMT) triggered by bandwidth-control, for instance, via hydrostatic pressure as revealed in κ-$(BEDT\text{-}TTF)_2X$, a quasi-two dimensional CTC composed of BEDT-TTF dimer layers separated by insulating X layers, or by external electric or optical field as demonstrated in K-TCNQ, a quasi-one dimensional CTC with segregated-stacked TCNQ anions and alkali K cations bounded by ionic interaction.[80, 83-85] BEDT-TTF, X, and TCNQ stand for bis(ethylenedithio)tetrathiafulvalene, $Cu[N(CN)_2]Br$ or $Cu[N(CN)_2]Cl$, and tetracyanoquinodimethane, respectively. In these systems, phase separation occurs on the macroscopic scale near the Mott transition, originating from the bistability of insulating Mott and correlated metal in free energy.[80, 83, 84] In K-TCNQ, specifically, this phase segregation is highly periodic with stripe-like patterns of alternating carrier-rich and carrier-poor domains as shown on Figure 1-7.[83] Intriguingly, beyond phase separation, mixed valence of neutral TCNQ molecules ($TCNQ^0$) and TCNQ radical anions ($TCNQ^{-1}$) is also discovered in the high-conductance state of K-TCNQ.[78, 83, 86] In inorganic Mott systems like oxides, it is known that such valence change involves the migration of oxygen vacancy or ions, resulting in local electronic inhomogeneity which plays a crucial role in IMT.[87-89] This paragraph is partially adapted from (*X. Dong et al., J. Phys. Chem. Lett. 2020,* ***11****, 8352−8357).*

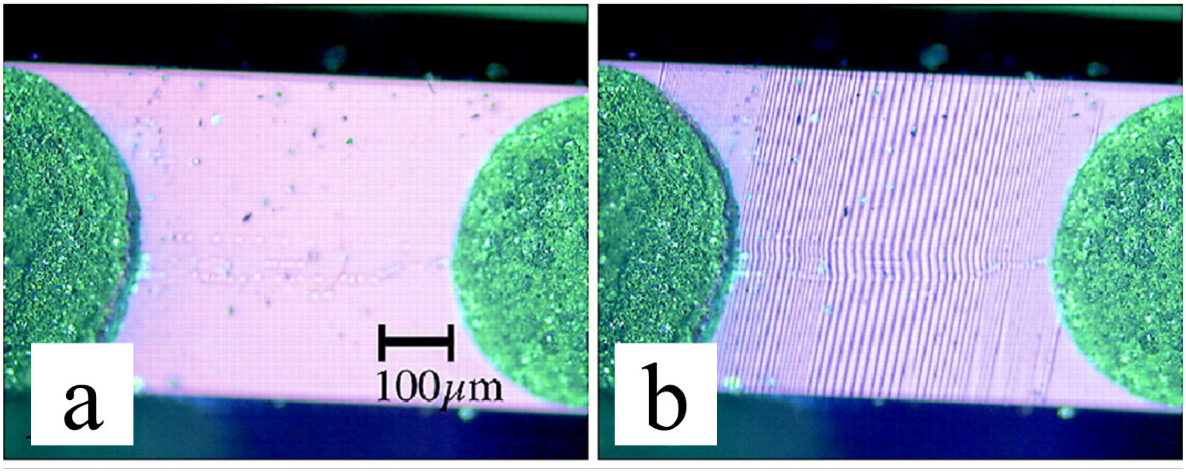

Figure 1-7: The insulating and conducting state of K-TCNQ triggered by electric field. Adapted from [83]
Image of the K-TCNQ projected on the CCD camera at insulating state (a) before application of the electric field and at conducting state (b) after a large electric field is applied. In the conducting state, it forms the carrier-poor and carrier-rich regions with mixed valency.

In Chapter 5, we will tackle the origins of the Mott insulator to metallic phase transition of K-TCNQ, an alkali metal CTC from investigating the spatial dependent electronic structure evolution with HS created from TCNQ ($TCNQ^0$) and K-TCNQ ($TCNQ^{-1}$) by STM/S. This work was pioneered by A. Tan who focused his study on organic molecular self-assembly on weakly interacting substrate. From the observation of the continuum metallic like state near the boundary and the band bending even near the boundary, we were able to connect the dots between the microscopic local electronic perturbation to the macroscopic phase transition observed in the bulk.

Overall, we will demonstrate different phase engineering techniques from the construction of different inorganic HSs, which are extremely relevant for electronic structure tuning, selecting and creation in the LD inorganic systems, revealing the crucial importance of the heterointerface. Our studies will show some insights for the logical choice of the constituents for the HS construction and rational modification of the substrate interactions. In addition, from the investigation of the microscopic interfacial effects in the organic lateral HS the interfacial effects will be shown to be essential for the macroscopic property phase transition in organic CTC. Finally, in the last chapter, motivated by the possibility of enhancing the interfacial superconductivity on $SnSe_2$ HSs, we will discuss the on-going work focused on the investigation the morphology and electronic structure tuning of $SnSe_2$ by $SrTiO_3(111)$ substrate.

2 Experimental Techniques

Throughout the course of this thesis, both organic and inorganic heterostructures (HSs) are constructed using bottom-up approaches. Substrates are the bottoms and thin films are deposited on top. HSs are created by consecutive deposition of the materials under ultrahigh vacuum (UHV) conditions. Inorganic thin films were grown by Molecular Beam Epitaxy (MBE), except for the monolayer h-BN on metal (e.g. Iridium), which was prepared by UHV-chemical vapor deposition. The organic thin film was deposited by thermal evaporation. The sample is then transferred into the Scanning Tunneling Microscope for characterization without breaking the UHV condition. Section 0 will introduce the experimental apparatus and discuss the main deposition techniques and sample preparation methods: MBE and UHV-CVD. Section 2.2 will discuss the main principles of STM/S. Section 2.3 will discuss the computational methods used in this dissertation: data analysis of the STS spectra and density functional theory (DFT).

2.1 Experimental Apparatus and Growth Mechanism

2.1.1 Experimental Apparatus

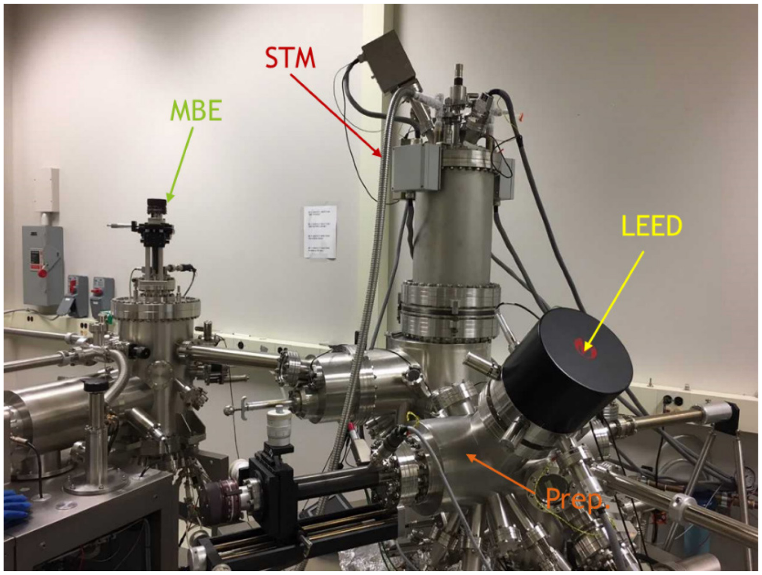

Figure 2-1: Experimental apparatus

Figure 2-1 (cont'd)
MBE – Molecular Beam Epitaxy Chamber, STM – Scanning Tunneling Microscopy Chamber, Prep.- Preparation chamber, LEED – Low Energy Electron Diffraction.

Sample growth and characterization were carried out in interconnected MBE and STM systems separated by the gate valves from Scienta Omicron GmbH as seen in Figure 2-1. Base pressure within the UHV system is below 1 x 10^{-9} mbar maintained by a series UHV pumps. The thin films were deposited by aiming one or more atomic or molecular beams toward a substrate heated to various temperatures, as illustrated in Figure 2-2. The substrate heating is done in two ways: 1. Direct heating method, by passing a current through conducting samples directly. This method does not work for insulators. 2. Radiative heating method, by radiated heat from the tungsten filament mounted at the sample holder. This method works for both conducting and insulating samples. The temperature is measured by a thermocouple mounted at the sample holder with calibration curve provided by Omicrons, or directly by a pyrometer if the temperature is high enough that the sample glows.

The atomic and molecular beams are generated by evaporation of high purity sources from thermal evaporators. Materials with low melting point and high vapor pressure (e.g. organic molecule and selenium) are typically evaporated by the Knudsen cell developed by Martin Knudsen.[90] In lower temperature, selenium tends to evaporate in a large cluster,[91] thus a secondary Cracker cell with higher temperature is equipped near the aperture to favor the formation of single atomic vapor. Metals with high melting point and low vapor pressure (e.g. tungsten, W) are better evaporated from focused e-beam bombardment from e-beam evaporators. UHV condition grants the mean free path of the atom and molecule to be larger than the physical size of the chamber to create a focused beam and avoid impacts from the ambient on growth and characterization.[92, 93]

To prevent cross contamination, gate valves are used to separate the growth chambers and the characterization chamber. The inorganic sample, such as TMD heterostructure and the 2D Sn are deposited in the MBE chamber The organic sample and the h-BN/metal substrate preparation were done in the Prep. chamber. The sample transfer is done via a magnetic transfer arm. The system is supported by vibrational dampeners to isolate the mechanical vibration from the building. The load-lock chamber allows the introduction of the sample without compromising the UHV condition in the main chamber. Layered materials can be mechanically cleaved under UHV in the load-lock before introduction to the main system to avoid exposure of the fresh surface to the air.

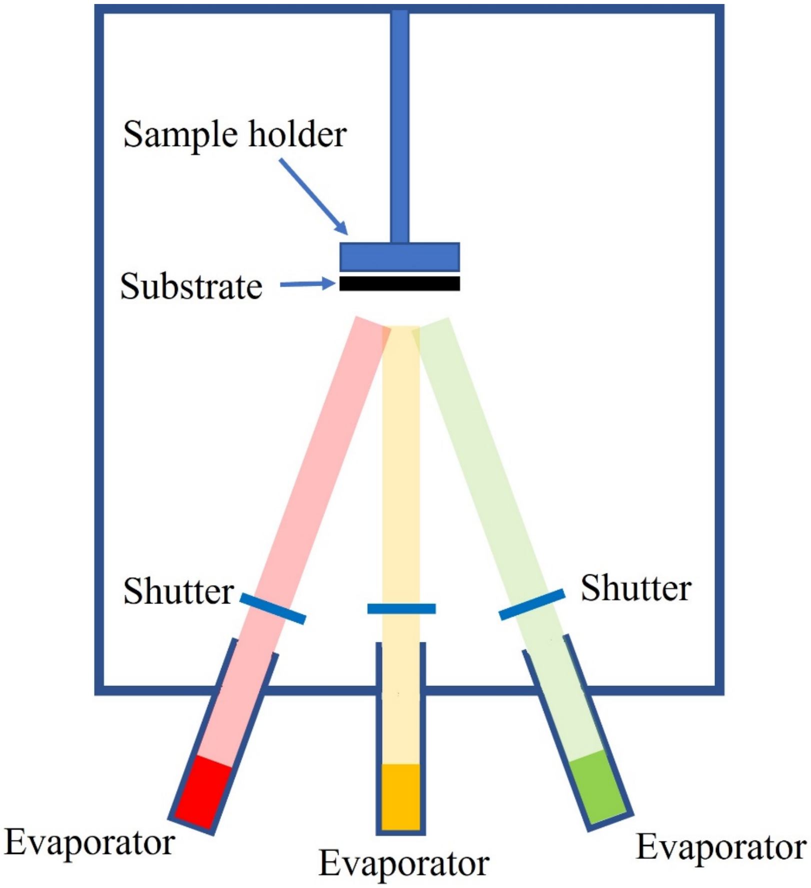

Figure 2-2: Schematic for Molecular Beam Epitaxy chamber

2.1.2 Thin Film Growth Mechanism

After the atomic/molecular species land on the substrate, their interactions with the substrate and each other begin the thin film growth. The growth mode is determined by the considerations of thermodynamic and kinetic processes. Organic molecules and inorganic atoms share many similar fundamental kinetic processes upon landing on a substrate. Absorption and reflection are both possible and their ratio determines the sticking coefficient. Now the absorbed atoms and molecules begin process of the diffusions (e.g. surface diffusion, diffusion across/along the edge) to search for energetically favored locations (e.g. at a terrace step edge) or run into each other to begin the nucleation of an island or to be desorbed, as shown in Figure 2-3(a).

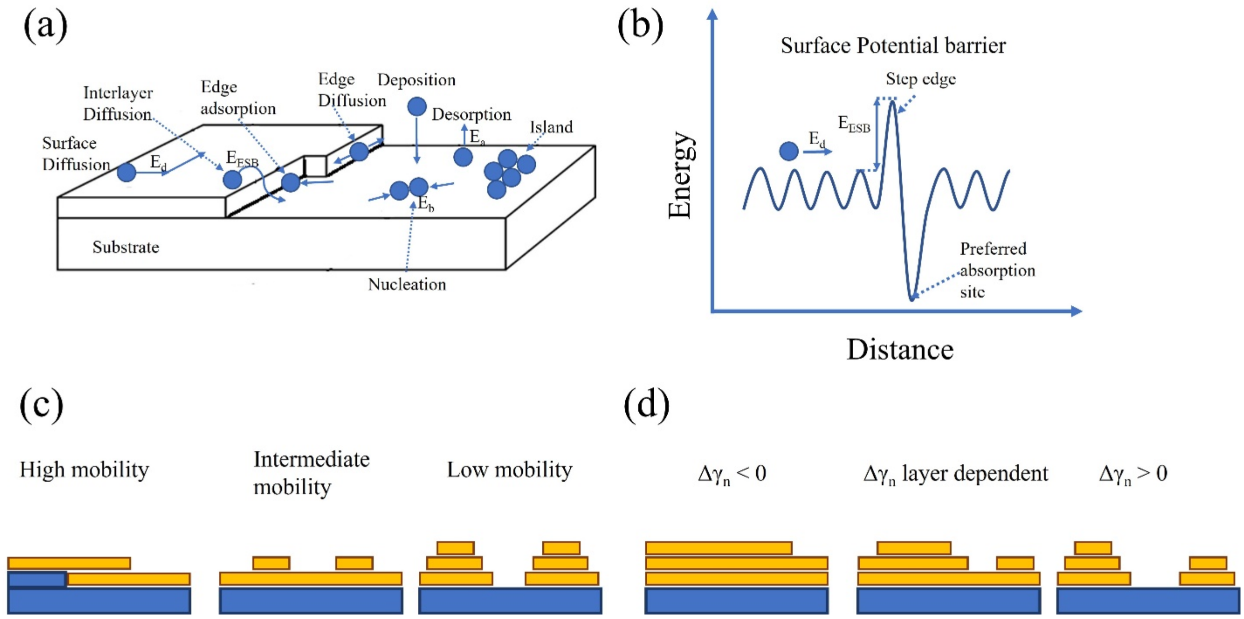

Figure 2-3: Kinetic processes and growth modes
(a) Kinetic processes of atom/molecule landing on a substrate surface. E_d is the surface diffusion barrier, E_{ESB} is the interlayer diffusion barrier. (b) Surface potential landscape with various diffusion barriers, with preferred absorption site at the step edge labeled. (c) Three thin film growth modes in kinetic considerations (d) Three growth modes in thermodynamic consideration.

Diffusivity and deposition rate can be effectively controlled by the substrate temperature and the flux rate which is adjusted by the evaporator settings. These processes are thermally activated where each is associated with an activation barrier. Higher substrate temperature increases the possibly to overcome these barriers which increase the diffusivity while reducing the deposition rate with the increased possibility of desorption. Better diffusivity on the surface favors 2D growth with larger diffusion length. For example, interlayer diffusion that particles diffuse down across the substrate or self-edges is dictated by the activation barrier known as the Ehrlich-Schwöebel barrier (ESB). The ESB originated from the loss of coordination during interlayer mass transport.[94-99] Overcoming the barrier prevents the aggregation of the particles in the upper step edge, and thus favors 2D growth. Similarly, a higher flux rate will increase the deposition rate, particles nucleated before they are able to fully explore the surface's potential landscape which creates kinetic roughing (i.e. formation of 3D clusters). Under the kinetic consideration, there are three growth modes depending on the diffusivity (i.e. particle mobility) as shown in Figure 2-3(c).

After careful calibration of the substrate temperature and growth rate, the kinetic limitation can be overcome with the thin film deposited at near equilibrium regime. In this regime, the thin film growth mode is dominated by the thermodynamics which considers the balancing of the energies of the static states. These energies include the surface energy of the substrate (γ_{subs}), the surface energy of the overlayer ($\gamma_{\text{film},n}$, where (n) represents the number of the layer) and the interface energy between them($\gamma_{\text{interface}}$). The interfacial energy considers the impacts of the interfacial effect such as strain and hybridization. In the thermodynamic considerations, there are also three growth modes defined by checking of the Bauer Criteria of the wettability ($\Delta\gamma_n = \gamma_{\text{film},n} - \gamma_{\text{subs}} + \gamma_{\text{interface}}$).[100] If $\Delta\gamma_n < 0$, the film desires to increase the energy gain by minimizing the substrate surface area, thus creating a layer by layer 2D growth mode, a.k.a Franck-van der Merwe mode. If $\Delta\gamma_n > 0$, the interface and film surface area are forced to be minimized which forms 3D island growth mode, a.k.a Vollmer-Weber growth mode. If $\Delta\gamma_n$ is layer dependent, initially $\Delta\gamma_n \leq 0$, but the sign flips with increasing thickness, the film exhibits a sequential 2D to 3D growth mode, a.k.a. Stranski-Krastanov mode. It is important to note that 3D island growth could be realized under near equilibrium regions due to the thermodynamic consideration or kinetic roughening, and it is important to distinguish their difference.

The same materials or different materials can be deposited on top of a substrate and are referred to as homoepitaxy and heteroepitaxy, respectively. In the scenario of heteroepitaxy with a large lattice constant difference and strong interfacial interaction ($\gamma_{\text{interface}}$ large), due to the large strain, the thin film structure can be significantly altered in additional to the growth mode change. The film quality is typically limited due to the formation of defects associated with strain relaxations.[101, 102] The changes in both film morphology and the growth mode both serve to minimize the total energy of the system. Hence, the most logical choice of a substrate for heteroepitaxy of single crystal thin film will have small lattice mismatching and fulfills the $\Delta\gamma_n < 0$ condition in this situation. In parallel, if the interfacial interaction is only van der Waals (vdWs) like ($\gamma_{\text{interface}}$ is nearly zero), the requirement of the lattice matching is significantly relaxed.[5] Deposition of one layered material on top of another layered material fits well in this category, the epilayer can generally grow with its own lattice due to the weak interactions. This method is later extended to layered material deposition onto other weakly interacting bulk substrates and is known as vdWs epitaxy, collectively.

Due to the complications mentioned earlier in the introduction including the possible hybridization of the edges state., the growth of the possible 2D TI inorganic materials used in Chapter 3 and 4 are typically carried out as close to the 2D growth mode as possible to achieve a large 2D domain on atomically smooth substrates.

2.1.3 Substrate Preparations

The proper substrate treatment is important since the surface defects (e.g. vacancies, adatoms and other structural and electronic defects) can impact the surface potential landscape and interface energy. They can act as preferred nucleation sites, which create additional barriers that limit film size and/or provide sources for creation of screw dislocations that triggers 3D growth. Surface defects could play more significant roles for the organic molecules as the organic materials growth and self-assembly are governed by both molecular-substrate and intermolecular interactions.[103-109]

The methods for obtaining an atomically smooth and contaminant free substrate are very different for layered materials and covalently bonded materials. The layered materials are typically mechanically cleaved to expose the fresh surface due to weak interlayer coupling and strong intralayer interaction. They can be cleaved in air if the surface is chemically inert. If the surface degrades fast in air, the cleaving will need to be done under UHV in the load-lock as mentioned previously. In our experiments, we use HOPG for our weakly interacting substrate which is chemically inert and thermally stable. HOPG can be directly cleaved in ambient conditions by the Scotch tape method,[110] then sonicated in high purity acetone and isopropanol alcohol to remove possible tape residue. Then it is immediately transferred into the UHV and degassed by annealing up to about 650K for several hours to obtain an atomically smooth surface.

On the other hand, the metal substrates like Cu(111) and Ir(111) were treated differently as cleaving is difficult. Single crystal metals were purchased from Princeton Scientific. A surface oxide layer formed at the metal's surface due to the prolonged air exposure with the intrinsic metal layers protected underneath. To remove the oxide layer, an ion gun from SPECS Surface Nano Analysis was used to sputter the surface layers away. In this ion gun, Argon (Ar) gas is used due to its inert nature, so it will not chemically react with the newly exposed surface. After controllably leaking Ar gas into the ion gun chamber by a leak valve, the Ar gas is bombarded and ionized by the electrons with about 100eV energy emitted from the ion gun filament and accelerated between the filament and the cathode cage. Then the Ar ions are accelerated by an electric field of 500-5000V, shooting a high-energy focused beam at the metal substrate. The argon ion bombardment removes the metal oxide on the surface due to kinetic energy transfer. Typically, an acceleration voltage of 2kV and a ~20-30μA beam current are sufficient. During the sputtering events, the pressure inside the preparation chamber rose to around 1-2 x 10^{-6} mbar. After the process of oxide removal, the surface became relatively rough. The metal substrates are subsequently annealed to enhance surface diffusion to reestablish an atomically flat surface. For the Cu(111) and Ag(111) substrate, the annealing temperature is typically around 773K, but Ir(111) needs to be annealed up to about 1500K to remove the trapped Ar bubbles.

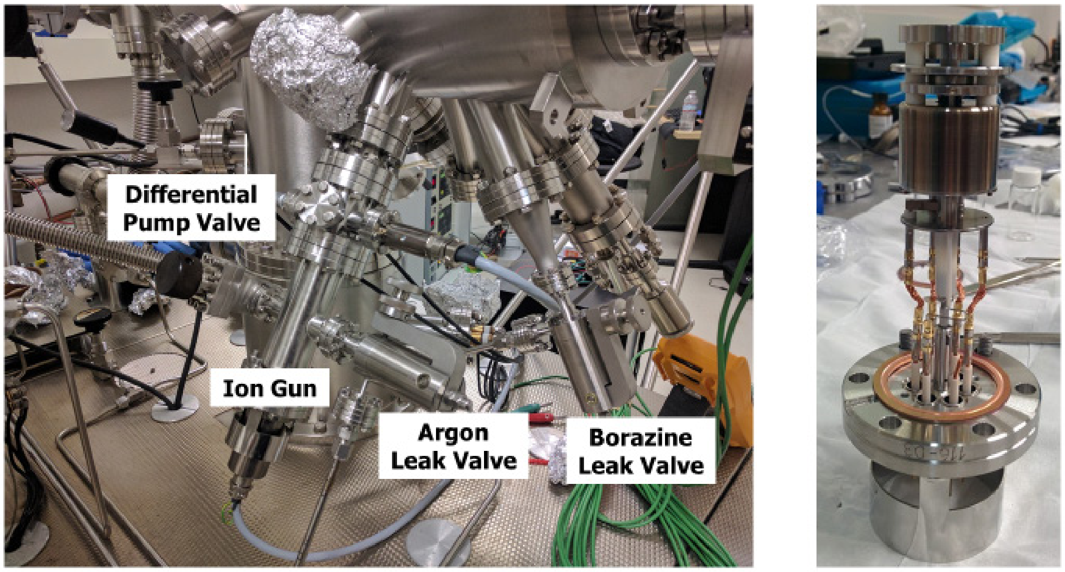

Figure 2-4: Picture of ion gun setup and borazine leak valve and ion gun ionization module. Image Courtesy of Andrew Tan.

To modify the interfacial interactions between the overlay and the substrate, the hexagonal boron nitride (h-BN) is grown on the metal substrate by UHV-CVD. h-BN/metal substrate contains

Moiré patterns with varying binding strength between h-BN and metal,[75] making it an interesting substrate for studying the substrate influence on thin film growth used in Chapter 3. A Moiré pattern describes a large-scale periodic pattern produced by overlaying two similar periodic pattens over each other that have different rotational angle or periodicity as shown in Figure 2-5. In thin film epitaxy, the Moiré pattern are typically originated from the mismatch of lattice and rotational angles.[111, 112]

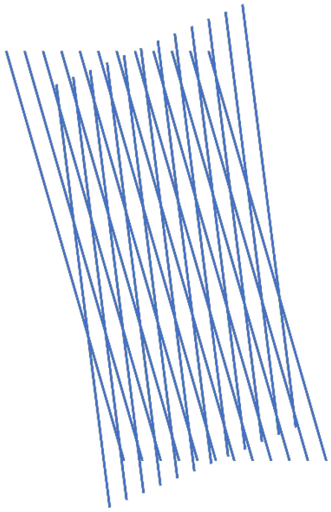

Figure 2-5: Moiré pattern from two identical patterns with small rotational angles

Borazine gas was introduced onto the Ir(111) substrate kept at ~1350K via a leak valve, with the chamber pressure maintained at $\sim 5\times10^{-7}$mbar. The borazine molecules are catalytically dissociated by the metal surface into boron and nitrogen atoms and hydrogen gases. Boron and nitrogen atoms organized into a hexagonal lattice in the form of h-BN with the hydrogen gases evaporated.[113] This growth process is self-limited as the catalytic activity of Ir(111) is significantly reduced after the surface is covered by a complete h-BN monolayer.[113] Ammonia borane powder was used as a precursor to borane as it is more thermally stable than the pure borazine liquid. To prevent degradation the pure borazine liquid requires storage in a fridge below 268K, whereas the ammonia borane powder can be kept at room temperature. In addition, borazine molecules react with air to form a white oxidized borazine residue which can be detrimental to pump integrity and vacuum. Thus, thermal decomposition of ammonia borane was utilized to derive borazine. Initially, ammonia borane powder is loaded into a stainless-steel vessel for pumping and degassing. After degassing, the vessel is raised to ~423K to slowly decompose the ammonia borane into borazine and hydrogen gas, and a solid polymer residue. The ammonia borane powder is so stable that its residue can be left for months within the vessel without noticeable issue. The borazine and ammonia borane chemical formula and the ammonia borane powder vessel is shown in Figure 2-6.

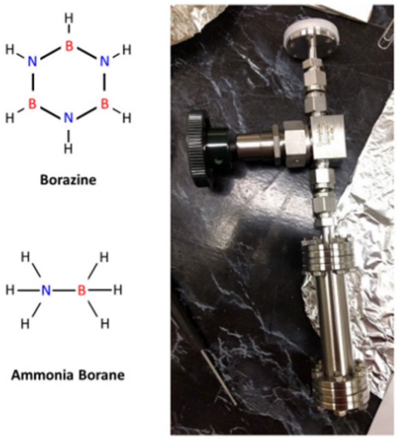

Figure 2-6: Chemical formula of borazine and ammonia borane and the ammonia borane powder vessel.
Image Courtesy of Andrew Tan.

2.1.4 Organic and Inroganic Thin Film Deposition

To prevent the accidental introduction of the foreign elements and for high-quality thin film growth, high purity sources are required for both organic inorganic thin film growth. Different purification techniques are employed for the organic and inorganic materials. The organic molecules are typically purified by a vacuum sublimation technique. Molecules are typically baked to ~413K for 3 days with the temperature accurately controlled by a Createc Fisher and Co GmbH low temperature effusion cell with a Knudsen based boron nitride crucible. Then the temperature is further increased for additional degassing. This process slowly sublimates the impurity and some molecules while preventing the chamber pressure from reaching too high. A mechanical shutter is used to prevent unwanted deposition during temperature ramping and degassing. Before switching of the molecular sources, the crucibles are emptied and sonicated in trichloroethylene, acetone and isopropyl-alcohol baths to remove the leftovers. After that the crucible is loaded back to the UHV chamber and annealed at a temperature that is much higher than the molecule's sublimation temperature to further remove any molecular residues. For the investigation of the K-TCNQ CTC in Chapter 5, a potassium dispenser from SAES was installed for potassium (K) atom deposition. The potassium atoms are released into the chamber without directional control when the dispenser is heated by a DC power supply with ~5A of current to trigger the decomposition of potassium-carrying salt in the dispenser. These processes are carried out in the Preparation chamber attached to the STM.

The inorganic materials growth is carried out in the MBE chamber to avoid cross contamination. Similar to the purification process used for the organic sources. The evaporator and sources are degassed by heating to the temperature in which the sublimation occurs to remove undesired oxide or other containments. As the temperature needed for this system is significantly higher than in the organic chamber, the evaporators are water cooled and the chamber wall is liquid nitrogen cooled to reduce the resorption of the materials from the walls and the evaporator body. For the tungsten (W) and Tin (Sn) sources, they are controllably evaporated by the e-beam evaporator EFM3 from FOCUS GmbH with precision flux current monitoring. As small fraction of evaporated source material will naturally be in ionized state so the current in the beam can be measured. The flux current tells us information about the flux rate.

The operation principle of the e-beam evaporation is fairly similar to the ion gun. After heating the filament with direct current, electrons are generated. Then these electrons begin to bombard the source target due to the high voltage different between the filament and the target. This electron bombardment heats up the target locally that prevent the introduction of excessive heat into the chamber which may compromise the chamber pressure. Due to the high melting point and low vapor pressure nature of W, a thin W rod (1.3mm diameter) and a high voltage (2kV) are used. The rod is locally heated at the tip and slowly sublimates. The Sn source has low melting point, it is placed inside a tantalum crucible and heated with e-beam with relatively low voltage (800V). The tantalum crucible is used due to its high melting point and low vapor pressure at the temperature of Sn sublimation. During the evaporation, heating power is controlled from the emission current, then the flux current is read to gauge the flux of the source atoms. Different materials have different degree of ionization thus, we may have different flux current reading for the same source flux rate. For the selenium (Se) source, Createc CRC-40 effusion cell is used. In additional to the heating source for the source directly, it is equipped with a Cracker filament at the aperture to favor the generation of a single atomic beam. In our normal operation, the Se source is heated up to ~433K and the cracker temperature is maintained at ~773K. At this setting, the chamber pressure increased up to $\sim 1\text{-}2\times10^{-8}$mbar. The Se vapor is supplied with excessive amount due to the relatively low sticking coefficient where the metal dichalcogenides thin film deposition rate is generally controlled by the flux of the metals.[114]

After the growth, the sample is transferred "*in-situ*" to the STM chamber for characterization with its working principle discussed in the next Chapter. The growth mode and the growth rate can be estimated from the growth morphology and the coverage estimation. For example, if $SnSe_2$ is deposited on the HOPG substrate with the Sn flux current of ~100nA for

20mins, and the STM scan reveals a total coverage of 0.5 monolayer (ML), then the growth rate is 1.5ML/hr. In each experiment, multiple trials need to be conducted for the best growth parameters including substrate temperature and the source flux tuning, until the best growth mode and morphology are achieved. For Sn thin film deposition in Chapter 3, ultra-high purity Sn source was evaporated from an e-beam evaporator with flux rate of ~2 ML/hr with the substrate temperature controlled by radiative heating ranging from ~473K to ~1073K. For metal dichalcogenides HS deposition on HOPG in Chapter 4, the pristine H-phase WSe_2 was grown at a rate of ~1.33ML/hr by co-evaporation of pure W and Se. The substrate was kept at ~723K during the deposition. $SnSe_2$ was subsequently deposited at a rate of ~0.5ML/hr by co-evaporation of pure Sn and Se. To avoid decomposition of $SnSe_2$, the substrate was kept at ~438K. Chamber pressure of $\sim 1\times10^{-8}$ mBar was recorded during the MBE growth.

2.2 Scanning Tunneling Microscopy and Spectroscopy

2.2.1 Quantum Tunneling

In surface science, scanning tunneling microscopy (STM) is an imaging technique that offers non-destructive imaging which gives information for both the topology and the electronic structure of the metallic and semiconducting samples with remarkable atomic scale resolution. STM has been widely used for the study of fundamental properties of the surface since its development in 1980s by G. Binnig and H. Rohrer.[115] Later it is expanded for the usage of “atomic manipulation”, where position of single atom on a substrate can be moved by a STM tip.[116] Recently, spin polarized STM have been invented to probe the information about the spin in a sample.[117, 118] Nonetheless, STM is commonly used to correlate local morphology and electronic properties.

The STM working principle is based on quantum tunneling. For simplicity, let’s first consider the quantum tunneling phenomenon in 1D. In classical mechanics, if a particle’s kinetic energy (E) is less than the potential barrier (U), it cannot move across the potential barrier. At a small enough dimension, the quantum mechanics become relevant. This particle can tunnel through the barrier with a finite possibility. The 1D quantum tunneling phenomenon can be described by the Schrödinger Equation:

$$-\frac{\hbar^2}{2m}\frac{d^2\psi}{dz^2}+U\psi=E\psi \tag{2-1}$$

where m and ψ are the mass and wave function of the particle, respectively, and $\hbar$ is the Plank constant.

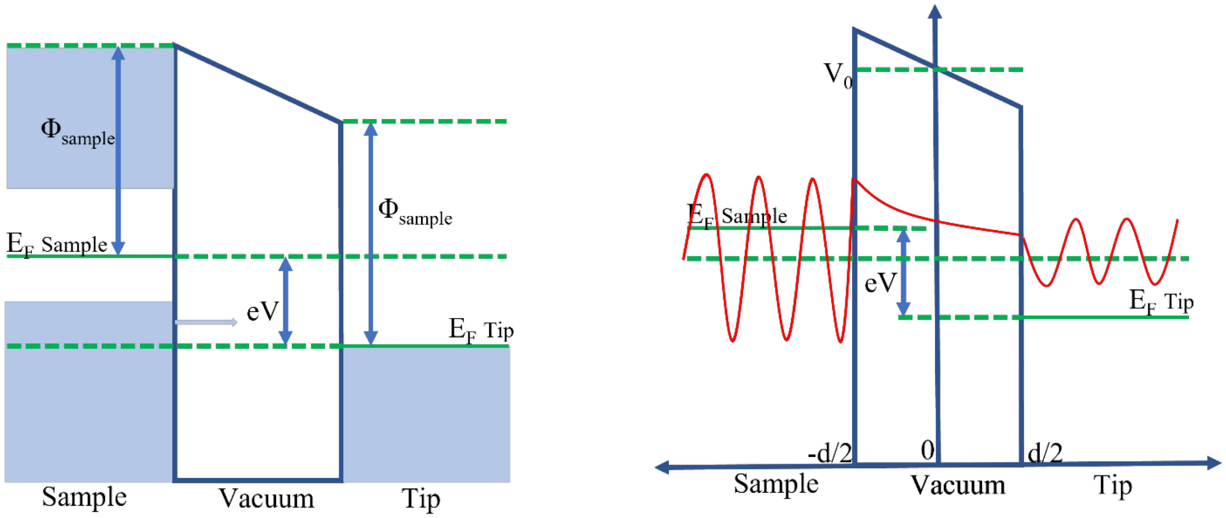

Figure 2-7: Tunneling mechanisms
(a) Schematic for electron tunneling between tip and sample with a vacuum gap in between. With applied bias, the Fermi level (FL) of the sample is shifted to create an energetic separation of *eV*. (b) Schematic for evolution of electron wavefunctions of tip and sample across a vacuum barrier of width, d. The sinusoidal wavefunctions exponentially decay across the vacuum barrier.

For the STM, electron tunneling is established by placing the metallic STM tip (e.g. W, or PtIr) a few angstroms away from the sample where the system initially reached electronic equilibrium with the two Fermi levels (FLs) aligned. After applying bias voltage, *V*, between the tip and sample, the FLs are shifted with an energy difference of eV where e is the elementary charge of an electron. Depending on the sign of the bias voltage, electrons can tunnel from the sample to the tip and vice versa. In Figure 2-7, under this bias condition, tunneling current is established by electrons flowing from the occupied states of the sample with higher FL into the unoccupied states of the tip with a lower FL. In this sense, this technique cannot be used for an insulator which offers no available density of states for electrons tunneling. However, if the insulator is thin enough (a few angstrom) and placed on top of conducting substrate, electron tunneling can still be established.

In this system where the bias voltage is small in comparison to the work functions of the tip and the samples, the vacuum barrier can be effectively described as a rectangular potential barrier:

$$U = \left\{ \begin{array}{ll} 0, & z < -\frac{d}{2} \\ V_o, & -\frac{d}{2} < z < \frac{d}{2} \\ 0, & z > \frac{d}{2} \end{array} \right\} \tag{2-2}$$

where V_o represents the barrier height with the work functions are defined as:

$$\phi = V_o - E_F \tag{2-3}$$

E_F is the FL energy. Then, the generalized solution for the Schrödinger equation will be:

$$\psi = \begin{Bmatrix} Ae^{ikz} + Be^{-ikz}, & z < -\frac{d}{2} \\ Ce^{\kappa z} + De^{(-\kappa z)}, & -\frac{d}{2} < z < \frac{d}{2} \\ Fe^{ik(z-d)}, \ z > \frac{d}{2} & \end{Bmatrix} \tag{2-4}$$

In here, k and κ are:

$$k = \frac{\sqrt{2mE}}{\hbar} \ ; \ \kappa = \frac{\sqrt{2m(V_o - E)}}{\hbar} \tag{2-5}$$

The particles wave function exponentially decayed at the classically forbidden region at $(-\frac{d}{2} < z < \frac{d}{2})$ (See Figure 2-7), with the transmission coefficient τ calculated by the ratio of particles on both sides of the barrier:

$$\tau = \frac{|F|^2}{|A|^2} = \frac{1}{1 + \left[1 + \left(\frac{\kappa^2 - k^2}{2k\kappa}\right)^2\right] \sinh^2(kd)} \tag{2-6}$$

Under the assumption that energy of the particles is much less than the barrier, $V_o \gg E$, we have $\kappa d \gg 1$, transmission coefficient become:

$$\tau => \frac{16k^2\kappa^2}{k^2 - \kappa^2} \ e^{-2\kappa d} \tag{2-7}$$

Therefore, the tunneling current I will be exponentially proportional to the tip-sample distance which allows the extreme sensitive of STM. [119-121]

$$I \propto \tau \propto e^{-2\kappa d} \tag{2-8}$$

The tunneling current ratio due to the small change in tip sample distance Δd will be:

$$\frac{I_{final}}{I_{initial}} = e^{-2\kappa \Delta d} \tag{2-9}$$

The work function of the tip and samples investigated in a typical STM study range ~4-5 eV, thus $\kappa \sim 1\ \text{Å}^{-1}$. For 1 Å decrease in the tip sample distance, the tunneling current will increase by a factor of $\sim$7.41, which is nearly an order of magnitude higher. For the STM tips, the tunneling current will be dominated by the current flow through the atomically sharp tip apex which allows the atomic resolution of the sample features.[119-121]

Beyond 1D modeling, Tersoff-Hamnn model and Bardeen's tunneling matrix which describes the tunneling process of an arbitrary three-dimensional geometry offers a more complete understanding of the quantum tunneling process.[122-124] Bardeen introduced a first order perturbation model of the quantum tunneling in 1961 that includes a tunneling matrix M that describes the wave function overlap between the tip and sample.[124] The transition probability is then described as

$$\tau = \frac{2\pi}{\hbar}|M|^2\delta(E_\mu - E_\nu) \tag{2-10}$$

where E_μ and E_ν are energies of the tip and sample respectively. With small bias V, it is reasonable to assume that the electron wavefunction and the tunneling matrix are unchanged. Thus, the tunneling current is then describable by the convolution of the sample and tip density of states as shown below.

$$I = e\frac{2\pi}{\hbar}|M|^2\int_0^{eV}\rho_\mu(E_F - eV + \varepsilon)\rho_\nu(E_F + \varepsilon)\,d\varepsilon \tag{2-11}$$

where ρ_μ and ρ_ν are density of state (DOS) of the tip and sample respectively. In other words, tunneling current requires the integration over all the contributing DOS with energies between E_F and $E_F - eV$ from both tip and sample. It is important to note that the occupied states with lower energy than the E_F, do not contribute to the tunneling due to the Pauli exclusion principle. The Bardeen's approach was later expanded by Tersoff and Hamnn in 1985 to include the effect of the tip geometry and the electronic structure of the sample.[122, 123] This helps to explain the high lateral resolution in the STM as tip and sample are no longer considered as two planar electrodes. The tip was considered as a geometry point (spherical) which helps to disentangle the tip properties from the sample properties. The STM tips are typically made of W and PtIr alloy, they have nearly flat DOS near the FL, thus the tunneling current variation are nearly tip independent, leaving the tunneling current primarily effected by the tip sample distance (d) and local DOS variation. The tunneling current is then proportional to integral DOS of the sample as shown below:

$$I = e\frac{2\pi}{\hbar}|M|^2\rho_\mu(0)\int_0^{eV}\rho_\nu(E_F+\varepsilon)\,d\varepsilon \tag{2-12}$$

If the quantities in front of the integral are all constants, then the current is proportional to the integration of the sample DOS over the energy between E_F and $E_F - eV$.

$$I \propto \int_0^{eV}\rho_\nu(E_F+\varepsilon)\,d\varepsilon \tag{2-13}$$

2.2.2 Operation Modes for Scanning Tunneling Micrscopy

Consequently, STM measurement produces images with the combination effect of the geometrical corrugation and local DOS. To achieve atomic resolution images, precision control of the tip scanning is required. The piezoelectric materials are highly sensitive to the applied voltage that a shape change with angstrom scale precision can be obtain via the piezoelectric effect. The piezoelectric elements control movement of the STM tip in the x,y and z directions, where the x-y plane is defined as parallel to the sample and the z direction is orthogonal. The z component records the changes of free tunneling parameters (I or d), depending on the operation modes.

Typical STM images are acquired in constant-current mode where the tip with the bias voltage and tunneling current are fixed to be a constant. The STM tip is controlled by a feedback loop that changes tip-sample distance to keep the tunneling current constant. Small tunneling current values (pA and nA range) requires the usage of a high gain and low noise amplifier to convert the signal into a voltage which is then compared to a preset value that corresponds to the desired tunneling current. Then a feedback voltage is subsequently generated and sent to the piezoelectric to change tip-sample distance that keep the tunneling current fixed. The change in z is recorded with respect to its position in the xy plane as the tip scans across the surface, creating an STM image.[119-121] This mode is commonly used for scanning of large surface with large surface inhomogeneity, as the feedback loop can prevent the tip from crashing into the surface, if tall features are present.

Otherwise, for a small and clean surface, the scanning speed can be increased by using the constant height mode without slowing down by the feedback. In this mode, the bias voltage and tip-sample distance are fixed while allowing the tunneling current to change. With the feedback disabled, the sample scans over an area with constant tip sample distance d, while generating a tunneling current map that can be converted to z(x,y). This mode allows the imaging of the surface without the introduction of the feedback induced artifacts. Neither the constant current nor constant height mode can be interpreted as pure topology due to the effect of the local DOS. A detailed schematic of STM operation is shown in Figure 2-8.

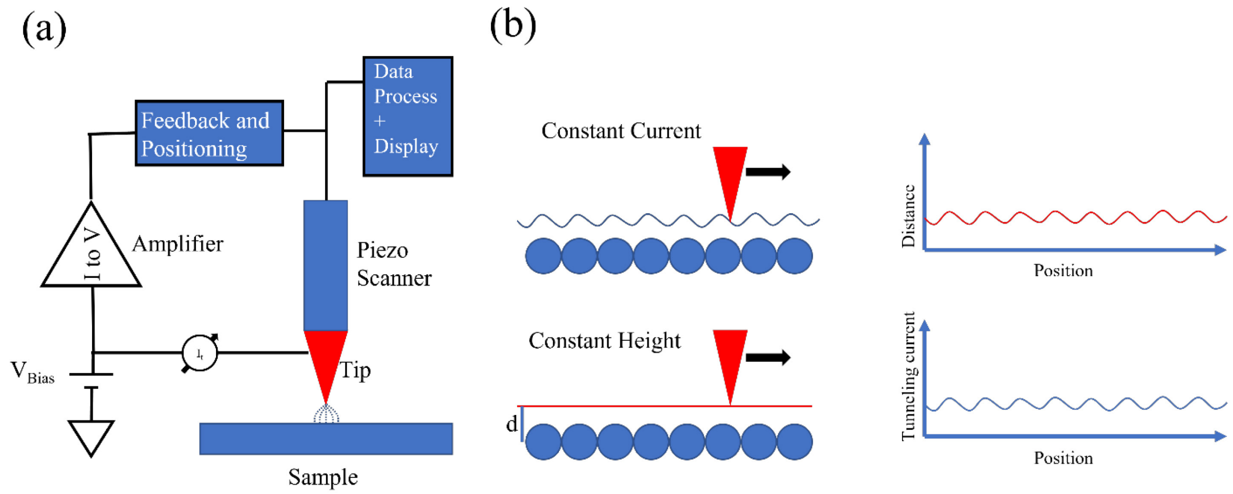

Figure 2-8: Schematic of STM and two operation modes
(a) Schematic of STM. (b) Constant current mode operates with feedback loop on, and d is the free tunneling parameter. Constant height mode operates with the feedback loop off and I is the free tunneling parameter.

2.2.3 Scanning Tunneling Spectroscopy

In comparison to other spectroscopy techniques, one of the biggest advantages of the STM is the ability of obtaining local spectroscopy with atomic precision. The local electronic structure can then be interpreted from scanning tunneling spectroscopy (STS). In this process, the tip is located at the point of interest in the xy plane, then the sample bias is swept across a desired range and the response in the tunneling current is recorded with the feedback loop disabled. An *I(V)* curve is generated in this process according to Equation (2-12). Taking the numerical derivative of the *I(V)* curve results in

$$\frac{dI}{dV} \propto \rho_v(eV) \qquad (2\text{-}14)$$

which is implying that that *dI/dV* is proportional to the DOS of the sample at the given energy. Nonetheless, obtaining the derivation numerically can often be noisy, thus a lock-in amplifier is often used to circumvent this problem. [119-121]

To implement the lock-in amplifier method, AC modulation is applied to the bias voltage with the sample bias taking the new form:

$$V = V_o + \delta V \cos \omega t \tag{2-15}$$

To the first order of δV the tunneling current will be given by:

$$I(V) = I(V_o) + \left(\frac{dI}{dV}\right)_{V=V_o} \delta V \cos \omega t \tag{2-16}$$

Here, the DC response corresponds to the baseline tunneling current before the modulation and the AC response which can be isolated and detected using a lock-in amplifier. Thus, STS (or *dI/dV*) spectrum can be generated concurrently with the $I(V)$ spectrum. The STS spectrum provides a signal proportional to the DOS of the sample at a specific location of the sample. This allows spatially resolved determination of the electronic structure of the sample.

2.2.4 Differential Conductance Mapping

Upon the observation of an interesting DOS feature in the STS spectrum, a differential conductance mapping can be performed for direct comparison of the STM image with spatial distribution of the DOS at the specific energy level. To do this, the AC modulation voltage is applied while scanning for STM image at a preset bias. The differential conductance signal is obtained at each point across the entire surface by lock-in amplifier, then plotted in the mapping images. The complementary STS images are also obtained simultaneously in the constant current mode to help to decouple the electronic structure from the topology. STS acquisition of these many points can take longer time which requires more extensive sample-noise isolation. At the same time, STM tip drifting need to be considered carefully.

2.2.5 Considerations and Complications in the STS Measurement

Previously, the transmission coefficient τ was regarded as a constant. However, in the system with large band dispersion, the parallel momentum $k_{||}$ is likely non-negligible and, the following form of the effective tunneling decay constant must be considered:

$$\kappa = \sqrt{\left(\frac{2m_e\Phi}{\hbar^2} + k_{||}^2\right)} \qquad (2\text{-}17)$$

where m_e is the electron mass, and Φ the tunneling barrier height. It is expected that tunneling into bands with smaller $k_{||}$ such as Γ ($k_{||}$=0) will be stronger than that into the bands of larger $k_{||}$.[122, 125, 126] This is very important for the accurate determination of the band edges which is indispensable for the discussion of semiconductors in this thesis. If the tip sample distance is too large and the conduction band minimum (CBM) and the valence band maximum (VBM) of the sample is located at large parallel momentum, the signals may be too weak to identify their onsets.

In a heterostructure system, either by placing a thin film or organic molecule assembly on top of a substrate or vertically stacking vdws layer materials or sticking layer materials laterally, modification to the electronic structures is often expected, especially at the locations near the interfaces. As mentioned earlier, charge transfer, substrate hybridization, strain, electron screening and defects could all contribute to the band structure changes. [14, 15, 127, 128] For a semiconductor, the band structure modification is often tied with the change of the bandgap size.[40, 129] The quasiparticle bandgap is defined to be the energy difference between the CBM and VBM which represents the energy range with zero DOS for a semiconductor. The combination of the spatially resolved STS and STM morphology can provide many clues to understand their roles on electronic structure modifications.

The correlation between electron doping and electronic band bending is one of the simplest examples. For the undoped semiconductor, in energy range, the FL is sitting at the center of the

CBM and VBM. If the sample is electron doped (n-doped), the electric field from the excessive electron will push the band downward causing a rigid downward shifting of the CBM and VBM. On the other hand, if the sample is hole doped, the electric field from the excessive hole will shift the CBM and VBM upward rigidly. This band bending phenomenon is an important gauge for us to determine the thin film doping level and understand the possibly of the charge transfer in the system. A schematic is shown below to illustrate the band bending effect with respect to (w.r.t.) different charge transfer direction in Figure 2-9.

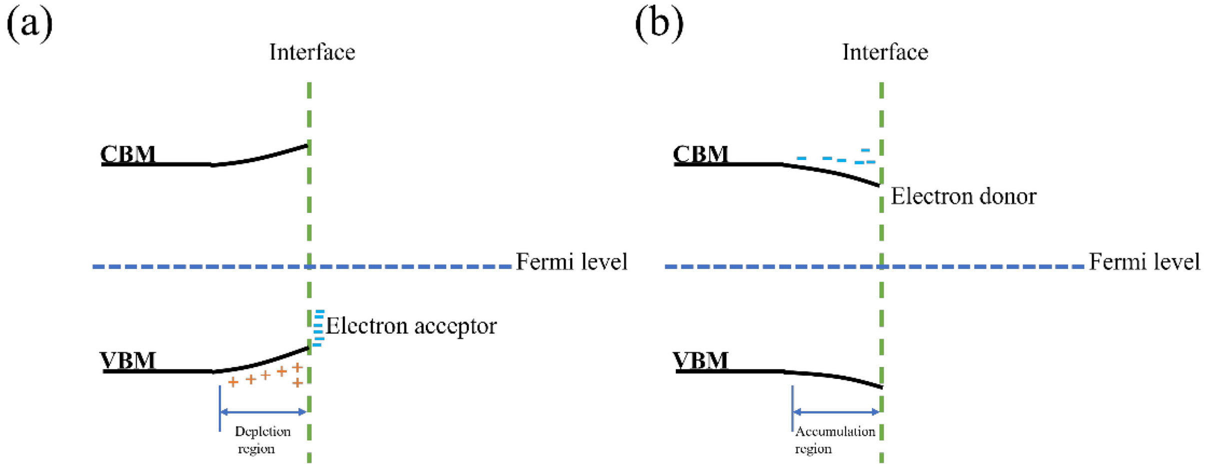

Figure 2-9: Charge transfer and band bending
(a) The electron acceptor states are typically near the VBM which is responsible for trapping the electron. The depletion region in the semiconductor will show an upward band bending. In contrary as shown in (b), the electron donor states are near the CBM which donates electrons to the sample and cause a downward band bending in the accumulation region.

In STS, the FL is located at zero energy. If a charge neutral semiconductor has a 2eV bandgap, then the CBM and the VBM should be sitting at ±1V. If the electrons are transferred to the thin film, the CBM and the VBM should be shifted rigidly downward. The higher the doping level, the closer the CBM will be to the FL. Although in actual experiment, the situation is often more complicated. For example, local defects are often observed for the MBE grown sample.[40, 74] For TMDs, metal and chalcogenide vacancies are common each providing a different doping effect for the film. Typically, the metal vacancies will provide p (hole) doping and the chalcogenide vacancies will provide n (electron) doping.[128, 130] Local STS spectrum taken on top of these vacancies will see both the localized defect states as well as the band bending. For example, STS taken on top of chalcogenide vacancies of TMD often shows localized donor-like state that is responsible for donating the electrons while manifesting an downward band bending due to the electron accumulation near the defect.[130] In the nearby locations, from taking spatial dependent STS, the width of the accumulation region can be found. With the degree of the rigid shifting in V and the width of the accumulation region (w), a local electric filed strength can be estimated by $E = V/w$. This again signifies the important exposed heterointerface in a lateral HS, where spatial resolved STS will provide a lot more information about the influence of the heterointerface to the nearby regions. Vice versa, if an unknown vacancy or unknown lateral heterointerface is found, we can also look at its electronic structure and DOS distribution and try to understand its origins. This is often more complicated as it often required to be compared to theoretical calculations and simulations that are often carried out by Density Functional Theory (DFT) which will be briefly introduced in the next chapter.

STS spectra are analyzed using a MATLAB program which performs the following functions. Initially, *I(V)* and *dI/dV* signal acquired from lock-in amplifier are imported into MATLAB. The *dI/dV* signal is normalized by the |I*(V)*| signal to minimize the contribution from the tip-sample distance. To prevent the occurrent of singularity from the bandgap in the substrate which may prevent normalization, an offset is applied. The spectra are then averaged after renormalization. Due to the influence of electronic noise in the system, a baseline offset can occur with the intensity of the bandgap no longer being at 0. This is countered by shifting the STS spectra to 0 at the baseline which is defined as the DOS intensity at the FL.

The tunneling process is often considered to be elastic between the tip and sample where electrons tunnels without energy lost. However, in a molecular system, phonons within the molecules can be excited if the electron energy is greater than the molecular orbital energy. These phonon excitations open new pathways for electron tunneling and are revealed as peaks and/or bumps in the DOS.[131-133] The excitation resonance peaks maybe convoluted due to the small energetic spacing between the excited vibrational modes $\hbar\omega_i$ where ω_i corresponds to the frequency of the vibrational modes.[131-133] For STS spectra of organic molecules with a convolution of multiple peaks, the energetic positions of these peaks are deconvoluted by fitting the STS curves with a series of Gaussian peaks by the built-in MATLAB fitting function.

To extract the bandgap and onsets of CBM and VBM, STS spectra are plotted in log scale, where a baseline was found from the linear fit within 2 standard deviations of the noise floor. Two tangent lines of the valence band edge and conduction band edge are plotted by a linear fitting from the voltage at which the change of signal strength becomes greater than 2 standard deviations from the baseline to a number of the points beyond. The number of these points may change according to different STS profiles. The CBM and VBM are defined by the intersections of the tangent lines with the baseline (noise floor). Finally, the bandgap is extracted from the energy difference. An example of the bandgap extraction from STS spectra is shown in Figure 2-10. This MATLAB software is developed from the combination of codes from both Andrew Tan and Timofey Golubev.

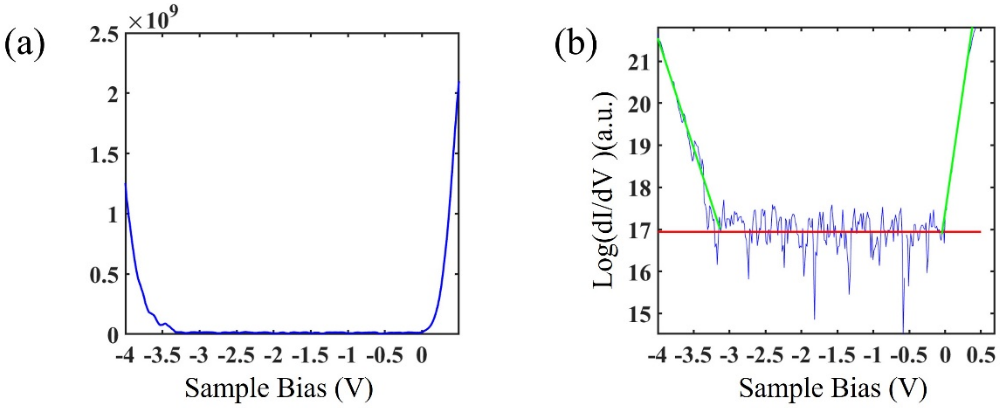

Figure 2-10: Extraction of VBM and CBM from the STS curves
(a) Normalized STS spectrum ($V_s = 0.5V$, $I_t = 200pA$) taken at the 3 × 3 reconstructed $SrTiO_3(111)$ surface. In (b), the STS spectrum is plotted in log scale, where the red line was found from the linear fit within 2 standard derivations of the noise floor. The green lines are from the linear fits at the valence band edge and conduction band edge, beginning from change of signal strength that is greater than 2 standard deviations. The CBM and VBM are defined by the interceptions of the linear plots between green lines and red line (noise floor). The VBM and CBM are extracted to be located at -3.13V and -0.04V respectively, deducing a bandgap of 3.09V for the 3 × 3 reconstructed $SrTiO_3(111)$ surface which is slightly smaller than the 3.20V found earlier for the unreconstructed surface.

For each sample, multiple STS curves need to be taken at different tip sample distances and ranges to make sure that we pick up the DOS features at larger momentums. In addition, when possible, the STS curves are compared to previous experimental and theoretical results for verifications. It is important to be cautions when comparing the experimental results obtained from different means. For example, the quasiparticle bandgap obtained from the difference in energy between the CBM and VBM may be significantly different from the optical bandgap. In a direct bandgap TMD, the quasiparticle bandgap often equals to optical bandgap plus the exciton binding energy.[134]

For a 2D TI, once the domain island is large enough that the edge states are not hybridizing with each other, the bulk (interior) and the edge DOS can be separately identified. STS tip landing on the interior should show a bulk bandgap near the FL while a conducting edge state will emerge at/near the edge (boundary to vacuum) or the boundary to a trivial insulator. Although the relative position of the FL can be shifted due to the previously mentioned doping effect. The extension of the topological edge states can be revealed from taking multiple spatial dependent STS spectra from the edge toward the interior or taking the difference conductance mapping at the sample bias of the edge state. The latter is typically more challenging as a constant current STM image is being taken simultaneously and the edge state may land inside a gap of a nearby semiconductor which could potentially crashes the tip. At last, as mentioned previously, the edge states of 2D TI are robust again non-magnetic defects which should also be verified to provide additional evidence for the topological nature of the states. Both spatial extension and robustness of the edge state are revealed in our 1T′-WSe_2 core in Chapter 5.

When investigating samples with small bandgap, it is important to consider the factors that contribute to the broadening effects. The thermal broadening is one of them. In a finite temperature, the signal broadening can be estimated by $\Delta E_T \sim 3k_BT$, where k_B is the Boltzmann constant, T is temperature in kelvin.[135] In additional, with the STS spectra taken by the lock-in amplifier, the energy resolution is further reduced by $\Delta E_{LI} \sim 2.5eV_{mod}$.[136] Considering both effects, the energy resolution of the STS spectra taken by the lock-in amplifier will be

$$\Delta E \approx \sqrt{(3k_BT)^2 + (2.5eV_{mod})^2} \tag{2-18}$$

It is important to choose proper temperature and modulation setting to optimize the energy resolution while dealing with small bandgap and small variations. Our experiments are typically carried out in liquid nitrogen temperature at ~77K. The energy resolution is predominately limited by the temperature. For a modulation amplitude set at 26mV in the lock-in amplifier, the energy resolution is ~68meV at 77K. Or in terms of the energy location of a peak in an STS spectrum, the uncertainty is ± 34meV. Meanwhile, non-measurement related electron lifetime broadening effects should also be considered such as broadening that arises from a combination of defect-based, electronic, vibrational scattering and coupling to the substrate. [62, 63]

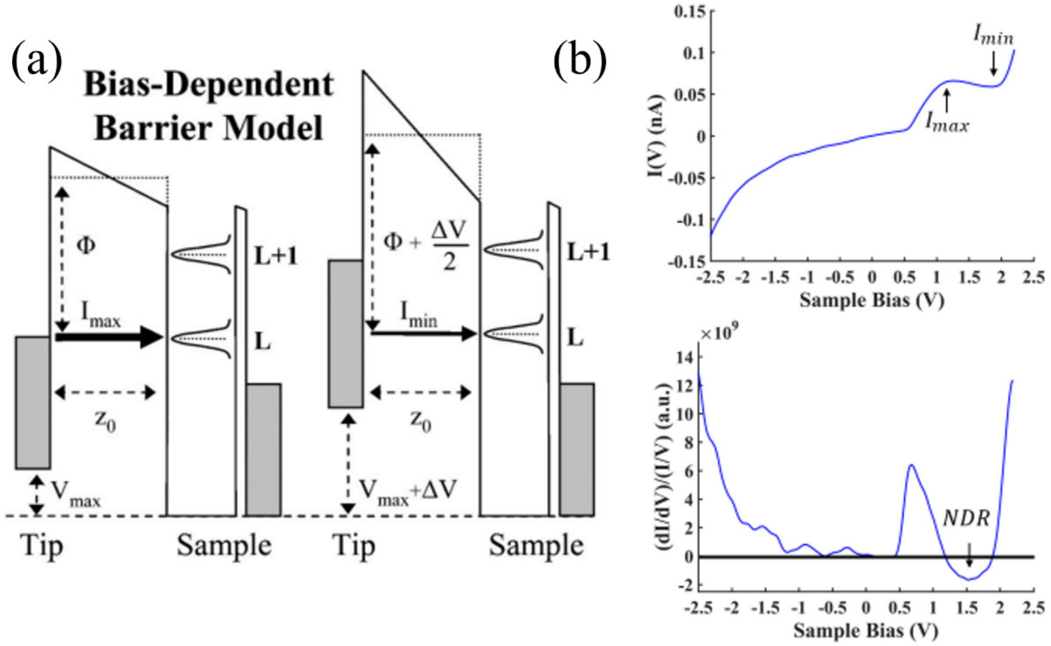

Figure 2-11: Negative Differential Resistance (NDR)
(a) Schematic diagram of the tunneling junction of a C_{60} bilayer on a weakly-interacting substrate. At fixed tip-sample distance z_o, but the two panels have applied sample bias difference of ΔV. I_{max} and V_{max} correspond to the maximum tunneling current and sample bias. I_{min} is location at the NDR regime (dips). L and L+1 label energetic position of molecule's lowest unoccupied orbital (LUMO) and LUMO+1 orbitals. Adapted from [137]. (b) Example *I(V)* and STS spectra of organic molecules on weakly interacting substrates showing NDR, image courtesy of Andrew Tan.

Other than the considerations mentioned earlier, there are more considerations specific to the STS spectra taken on organic molecules on weakly interacting substrates. The molecular orbital features are often well preserved when deposited onto weakly interacting substrates.[137-139] Molecular orbitals have well defined energetic positions, where no DOS from the molecules are present in between, as shown in Figure 2-11. A important signature of the weak substrate interaction and well preservation of the electronic structure of organic molecule is based on the observation of a negative differential resistance (NDR) regime.[137-139] In this region, negative differential resistance is shown, the *dI/dV* signal dips despite the increase in the sample bias which is originated form voltage dependence of the tunneling barrier height as shown on Figure 2-11.[137]

To see the voltage dependent barrier height, we need to rewrite the the transmission coefficient τ in Equation (2-6) as:

$$\tau \propto e^{-c\int_0^{z_o} dz\,\sqrt{\Phi_\mathrm{o}-E+eV\frac{z}{z_o}}} \qquad (\ 2\text{-}19\ )$$

where Φ_o is the work function and $\mathrm{z_o}$ is the tip-sample distance,$\mathrm{c} = 2\frac{\sqrt{2\mathrm{m_e}}}{\hbar}$. After simplification, we get:

$$\tau \propto e^{-cz_o\sqrt{\Phi_o-E+\frac{eV}{2}}} \qquad (\ 2\text{-}20\ )$$

Under the same assumption of $V \ll \Phi_o$, Equation(2-20) agrees with Equation (2-7). When the V is no longer much less than Φ_o, Equation(2-20) should be used. For example, when comparing tunneling current from V that shifted the FL of the tip to align with the energy level of one of molecular orbital $E_L = eV_L$ and $V > V_L$. The ratio of $\frac{I(V)}{I(V_L)}$ derived from Equation (2-8)(2-20) shows:

$$\frac{I(V)}{I(V_L)} = e^{-cz_o\left(\sqrt{\Phi_\mathrm{o}-\frac{E_L}{2}+\frac{eV}{2}}-\sqrt{\Phi_o-\frac{E_L}{2}}\right)} \qquad (\ 2\text{-}21\ )$$

This ratio is always less than 1 and contributing to the observation of NDR at $V > V_L$.[137] The NDR can be overwhelmed by the present of a highly conductive metallic substrate that contribute a continuum of state that eliminates the NDR. [137-139]

At last, the future perspective of the experiment heavily involves the superconductivity and superconductivity proximity effect. The signature of the superconductivity in STM will be explained briefly here. In temperature below the superconducting transition temperature (T_c), twin superconducting coherence peaks outside the superconducting gap will be observed in the STS spectra as shown in Figure 2-12(a). The size of the superconducting gap reflects the maximal pairing strength which is also related to the T_c. The large the band gap, the more energy is required to break the pairing, and the higher the T_c. Meanwhile, by fitting the STS spectrum, a possible pairing mechanism can be asserted. In Figure 2-12(a), the STS curves can be reasonably described by BCS Dynes expression with a single isotropic s-wave gap.[140, 141] Thus, the Pb single crystal is most likely a conventional s-wave superconductor.[140] Of course, a high T_c superconductor may have different pairing mechanism which will requires different fitting.[142] As the superconducting gap is usually very small (less than 1meV), the temperature and the modulation amplitude of the lock-in amplifier need to be very small to have a good enough resolution.

In case of type II superconductor, quantized vortices will emerge with the application of a magnetic field above the lower critical field.[143] The superconductivity is suppressed in the vortex with its radius comparable to the superconducting coherence length. A quasiparticle then developed in the zero bias from the coupling of normal electron inside the vortex to the superconducting electron outside. [144-146] In STS, it will be reflected as a sharp peak at zero bias as shown in Figure 2-12(c). From zero-bias imaging of the magnetic vortex (Figure 2-12(b)), the coherence length of the superconductor can be estimated which will be critically tied to the proximity effect when it is coupled with other non-superconducting materials.[147] Pioneered by R. Holm and W. Meissner,[148], the superconducting electron pairs cannot make abrupt change in contact with normal metal. The pairing state can penetrate the normal metal which is eventually destroyed by the scattering event. The length of the penetration depends on the both the intrinsic coherence of the materials and the property of the normal materials. For the STS investigation, both vertical and lateral heterostructure can be constructed to probe the proximity effect, where the lateral heterostructure will provides the most convenient platform for the spatial dependent investigation of this effect. However, the boundary defects from lattice mismatched materials may provide more source of scattering, which need to be considered carefully.

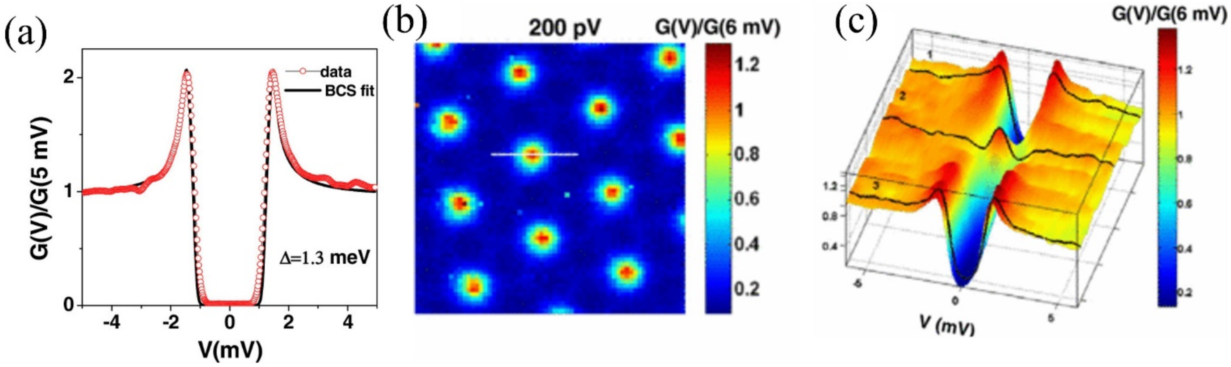

Figure 2-12: Example superconducting STS spectrum of Pb and vortex imaging of $NbSe_2$
(a) STS spectrum showing superconducting coherence peaks. The data points are labeled by red dots. The black line is based on single-BCS s-wave gap fitting. (b) Zero-conductance imaging of the magnetic vortex at magnetic field of 200 mTesla and T=350mK. (c) STS spectrum across the white line in (b). This image is adapted from [140]

2.3 Density Functional Theory

2.3.1 Introduction

As mentioned in the previous chapter, theoretical calculations are often required to make the connection between our experimental results and our hypothesis. From the STM/S, the local electronic structure can be correlated to the local variations in the STM image. As the STM image reveals the local convolution of the topology and the local density of state, theoretical calculation of the electronic structure will help to deconvolute these effects. Electronic structure calculation can be achieved by solving the Schrödinger Equation numerically. This calculation is first principle in nature, as it requires no external parameter other than a basic description of the system, such as the structure of a crystal. Density functional theory (DFT) is currently one of the most popular techniques in used to solve the Schrödinger Equation which describes the quantum behaviors of the solid-state system in a microscopic level. In the consideration of the computational resource requirements, DFT has the advantage of describing an interacting many-body system with

3N degree of freedom by its particle density, which only has 3 spatial coordinates. The main principle of the DFT is based on the famous Hohenberg-Kohn (HK) theorems,[149, 150] which pointed out that all properties of a system can be described as a functional of the ground state density.

The basic principle of DFT and some minor complications will be briefly discussed in this chapter.

2.3.2 The Hohenberg-Kohn (HK) Theorems

HK theorems [149, 150] consists of two separate parts as summarized below:

Part I: For a system of interacting particles, the ground state particle density $n_o(r)$ *is uniquely determined by an external potential* $V_{ext}(r)$ *up to a constant.* In other words, all properties of a system with interacting particles can be uniquely determined by the ground state particle density.

Part II: The electron density $n(r)$ *that minimized the energy functional* $E(n(r))$ *is the ground state density* $n_o(r)$ *and the* $E(n_o(r))$ *corresponds to the ground state energy of the system.* In other words, the ground state density and the ground state energy are in one-to-one correspondence.

Together, ground state properties of a system can be described as a functional of the ground state density.

2.3.3 The Kohn-Sham (KS) Equations

Originating from the HK theorem, the Kohn-Sham ansatz transform the many-body system into an independent particle system with the same ground state density.[149, 150] The interacting potential is mapped into the non-interacting KS potential $V_{KS}(r)$. The ground state can be obtained by solving the N independent single particle KS equations in atomic units:

$$(\frac{1}{2}\nabla^2 + V_{KS}(r)\psi_i(r)) = \varepsilon_i\psi_i(r) \tag{2-22}$$

where $\psi_i(r)$ is the single particle wavefunction with lowest eigenvalue ε_i.

The density of the system will be

$$n(r) = \sum_{i=1}^{N} |\psi_i(r)|^2 \tag{2-23}$$

The energy functional can be written as

$$E_{KS}\big(n(r)\big) = T_s\big(n(r)\big) + E_H\big(n(r)\big) + \int d^3r V_{ext} n(r) + E_{xc}(n(r)) \tag{2-24}$$

where T_s represents the kinetic energy of the N single particle

$$T_s\big(n(r)\big) = -\frac{1}{2}\sum_{i=1}^{N}\int d^3r\psi_i{}^*(r)\,\nabla^2\psi_i(r) \tag{2-25}$$

and E_H represents the Coulomb self-interacting energy

$$E_H\big(n(r)\big) = \frac{1}{2}\int\int d^3r d^3r'\frac{n(r)n(r')}{|r-r'|} \tag{2-26}$$

At last, $E_{xc}(n(r))$ is the exchange correlation term that account for the different between the extract kinetic energy of the interacting system with T_s and electron-electron interaction energy that is not described by the simple E_H. It is the only unknown that includes all the quantum mechanical effects. The accurate description of the real interacting system depends critically on the exchange-correlation energy functional.

The ground state energy of the interacting system can be solved by minimizing the $E_{KS}\big(n(r)\big)$, which is typically carried out in a self-consistent numerical calculation. The KS potential can be expressed as

$$V_{KS}(r) = V_{ext} + \int dr' \frac{n(r')}{|r - r'|} + \frac{\delta E_{xc}(n(r))}{\delta n(r)} \qquad (2\text{-}27)$$

The numerical calculation is typically performed by varying electron density n and the effective potential V_{KS} to achieve self-consistency.

Step 1: Guess an initial value of electron density n(r).

Step 2: Calculate the $V_{KS}(r)$ using Equation(2-27).

Step 3: Solve for the single particle wave function using Equation(2-22).

Step 4: Solve for new density n(r) based on the wave function using Equation(2-23).

Step 5: Check if the new density is consistent with the initial guess. If they are not consistent, go back to Step 2 and begin new interaction. If they are consistent, the process is done.

2.3.4 Exchange Correlation Approximation

The most critical component in this calculation is still the correlation exchange equation, the better it can describe the quantum mechanical effects, the more accurately DFT can describe the system. In practice, E_{xc} is often approximated by local or semi-local functional: local density approximation (LDA) and generalized-gradient-approximation (GGA). LDA approximate the exchange correlation functional to a system with homogeneous electron density (HEG).[149, 150] This approximation will best describe a system that is similar to HEG, such as a metal surface, but not very good for system with strong electron correlations. In fact, the LDA approximation is surprisingly successful in practical use, as most the exchange and correlation effects in solid-state systems are short ranged.

On the other hand, the fact that only local density is used, the non-physical self-interaction with electron acting on itself in the Hartree operator cannot be exactly cancelled. The remaining energy push up the energy of the occupied states but does not contribute to the unoccupied states as there is no self-interaction for them. Consequently, for a semiconductor the valence band is moved upward then reducing the bandgap. Thus, it is often referred as self-interaction error (SIE).

In the next level of the approximation, GGA consider both the local electron density and the gradient of the density which makes the exchange correlation semi-local.[151-153] The non-locality in this approximation depends on the electron density. The exchange will dominate for high density which is true in real systems. The correlation will become comparable to the exchange at low density and eventually, equals to the locality of the LDA as the density approaches to zero. In comparison to LDA, GGA typically is better for calculation for the inhomogeneous system. Subjected to the same SIE, GGA determination of the bandgap can also be unreliable. Later hybrid functionals were developed to try to cancel the SIE effect by mixing part of the Hartree-Fock exchange.[154-156] Nonetheless, they are computationally more expensive. In this thesis, a generalized gradient approximation in the form of Perdew–Burke–Ernzerhof (PBE) was adopted for the exchange-correlation functional.

2.3.5 Structural Relaxation

Structural relaxation is important to make sure the inter-atomic interaction is optimized. The initial guess of the structure of a system is based on the experimental observations. Then the guessed structure is feed to the DFT calculation software to minimize its inter-atomic force, which optimizes the overall structure in which total energy is minimized. The structure is optimized if each atom experiences less forces than a user-defined minimum threshold. This optimization needs to be done for all the structures hypothesized in our experiments to make sure the guessed structure is feasible. Multiple initial structures were constructed and optimized in each of our experiments. Then, the electronic calculations such as formation energy, density of state (DOS) and projected density of state (PDOS) and STM simulation are carried out for comparison to the experimental results to deduce the most possible configuration. For example, when placing a thin film on a substrate, the formation energy is an important criterion for understanding the stability of the system. The formation energy was defined as: $E_F = (E_{tot} - E_{sub} - \mu At * n)/n$, where E_F is the formation energy of single atom in the thin film, E_{tot} is the total energy of the model, E_{sub} is the total energy of the substrate, and μAt is the chemical potential of single atom. If we have multiple structures, the one with lowest formation energy will be most stable. Next, the STM simulation can be directly compared to our experimental STM image to verify our structure. STM/S provides spatially resolved DOS at atomic scale. The local STS spectra can be compared to the PDOS from the atoms in the same region from the calculations. If they agree, then the structure can be confirmed with better confidence. Although in this process, exact agreement between them maybe difficult as DFT description of the system is not completely accurate. As mentioned previously, the bandgap can be reduced due to the SIE. But the main feature and the general trend associated with structural and electronic evolutions can still be observed which provides strong evidence to support the experimental observations.

Theoretical calculations in Chapter 3 are done in collaboration with Dr. Lizhi Zhang from department of Physics and Astronomy, University of Tennessee and Dr. Mina Yun from Center for Nanophase Materials Sciences, Oak Ridge National Laboratory. All theoretical calculations were performed using density-functional theory (DFT) implemented in the Vienna ab initio simulation package (VASP)[157] with the projector augmented wave (PAW) method.[158] The energy cutoff of the plane-wave basis sets was 400 eV, and a k-mesh with k-spacing of $\sim 2\pi \times 0.02 Å^{-1}$ was used for the self-consistent total energy calculation. In the calculation, a generalized gradient approximation in the form of Perdew–Burke–Ernzerhof was adopted for the exchange-correlation functional,[151] a vacuum layer of 15 Å was used, and all Sn atoms were relaxed until the net force on every atom was smaller than 0.01 eV/Å. To consider the van der Waals interactions, the dispersion correction by using Grimme's DFT–D3 scheme was considered.[159] This paragraph is partially adapted from (*X. Dong et al. 2D Mater. 2021,* ***8,*** *045003).*

Theoretical calculations in Chapter 4 are done in collaboration with Dr. Lai Wei from department of Chemical Engineering and Materials Science, Michigan State University. DFT calculations were performed by the cp2k[160, 161] package that employs mixed Gaussian and plane wave basis sets. The valence electron configurations were Sn ($5s^2 5p^2$), W ($5s^2 5p^6 5d^4 6s^2$), and Se ($4s^2 4p^4$) with Goedecker–Teter–Hutter (GTH) scalar-relativistic and norm-conserving pseudopotentials.[162, 163] The plane wave cutoff was 400 Ry and Gaussian basis sets were DZVP-MOLOPT-SR.[164] The exchange-correlation functionals was the dispersion-corrected revised Perdew-Burke-Ernzerh of with Becke-Johnson damping (revPBE-D3BJ).[152, 153] Monolayer simulation cells, including both unit cells and their supercells, had 20 Å vacuum space in the *c* direction, where the band structures and density of states of monolayers were calculated based on the unit cells and supercells, respectively. 1H-WSe_2/1T-$SnSe_2$ and 1T′-WSe_2/1T-$SnSe_2$ HSs (~300 atoms with Γ k-point) were formed by joining two azimuthally aligned nanoribbon domains with periodic dislocation cores along the boundary as well as at least 25 Å vacuum space in the *b* direction. The initial structures were constructed in Visualization for Electronic and Structural Analysis VESTA) program[165] based on the STM observation, then optimized until the force was below 0.02 eV/ Å, while keeping the coordinates in the *c* direction fixed. This paragraph is partially adapted from (*X. Dong et al. Mater. Horiz. 2021,* ***8,*** *1029-1036).*

3 The Role of Substrate on Stabilizing New Phases of Two-Dimensional Tin

The rapid advances in two-dimensional (2D) materials of various crystalline symmetry and elemental compositions have generated rich functionalities.[166, 167] Artificially stacking or stitching dissimilar materials via construction of heterostructures further offers an unprecedent potential for tailoring the properties of each constituent.[168] While van der Waals (vdWs) stacking significantly reduces the requirement of lattice matching[3, 168] and diminishes interface electronic states, intriguing physics could emerge from features such as strain or charge transfer at strongly interacting interfaces.[127, 169-171] For instance, FeSe monolayers grown on $SrTiO_3$ substrate exhibit drastically enhanced superconducting transition temperature owing to interfacial charge transfer and phonon coupling.[169] Additionally, a metastable phase of transition metal dichalcogenide monolayers with nontrivial topological properties could potentially be stabilized by interfacial interaction with metal substrates.[170] On the other hand, a "strong" interaction with the substrate could deteriorate the inherent topological properties of monolayers.[127] So a delicate balance needs to be reached for obtaining substrate tuning as well as film quality. A promising route towards modification of interfacial interaction has been demonstrated recently via remote epitaxy assisted by monolayer graphene that separates the single-crystalline film from the otherwise strongly interacting substrate.[172]

Hexagonal boron nitride (h-BN) monolayers with ~6eV bandgap, formed in a self-limiting fashion on metal substrates, may be utilized to mediate interfacial interaction and to stabilize the desirable phases in thin films adsorbed above.[75] To explore this effect, 2D tin (Sn) is selected as the adlayer, which is a highly interesting class of quantum materials. Sn is known to exhibit two allotropes, α and β phases, with drastically different properties in its bulk form.[173] β-Sn (body-centered tetragonal structure) has been long investigated for its superconducting property,[174] whereas semi-metallic α-Sn (face-centered diamond cubic structure) has attracted increasing attention due to its intrinsic parity inversion near FL which relates to non-trivial topology.[175, 176] Few-layer α-Sn was shown to transform from ordinary semimetal to topological insulator (TI) and to topological Dirac semimetal within 2% of in-plane strain[176]. Recent experiments have also revealed superconductivity in few-layer α-Sn,[177, 178] which, combining with the TI properties, offers a potential template for the search of Majorana fermions.

Down to the monolayer regime, stanene, a single layer of α-Sn(111), has been predicted to be a 2D TI with large electronic bandgap, which holds promise for room temperature applications of quantum spin hall (QSH) effect.[53, 179] Nonetheless, unlike its inert graphene counterpart that is arranged in planar honeycomb structure, freestanding stanene is buckled due to the mixed sp^2-sp^3 hybridization and thus not mechanical exfoliable.[53] As pointed out in Chapter I, Molecular beam epitaxy (MBE) deposition of monolayer stanene has been explored on various substrates, where the sensitivity of stanene's electronic and topological properties to strain and chemical passivation renders the proper control of interfacial interactions crucially important.[65, 66, 73, 180, 181]

In this chapter, we report the growth morphology of Sn on Ir(111) substrate with and without h-BN decoupling layer. We confirm that the substrate plays a key role in determining 2D Sn with distinct structural and electronic properties. Most intriguingly, a new phase of Sn monolayer, corresponding to the $\sqrt{7} \times \sqrt{7}$ superlattice of Ir(111), is identified on h-BN/Ir(111). In conjunction with first-principles calculations, we unravel the critical role of substrate on stabilizing the $\sqrt{7} \times \sqrt{7}$ phase. This study demonstrates the ability to remotely tune the structure and strain of 2D Sn through h-BN monolayer. With the wide variety of choices on metal substrates including its *d*-orbital occupancy and the intercalation of noble metals that tailor the strength of interaction between h-BN and substrate, it potentially opens a new route for engineering the physical properties of Sn films. This chapter is adapted from Reference[182]: *X. Dong et al. 2D Mater. 2021,* ***8,*** *045003).*

The drastic changes in Sn growth morphology were identified by STM upon incorporation of the h-BN monolayer. Our first-principles DFT calculations support that this observation is strongly associated with the strength of the interfacial interaction, as manifested by the degree of charge transfer between Sn and the various substrates such as h-BN, h-BN/Ir(111) and Ir(111) (Figure 3-1). The amount of transferred charges is smallest on the free-standing h-BN substrate, which increases with the presence of Ir(111) beneath h-BN and becomes largest on bare Ir(111) (Figure 3-1,Figure 3-2).

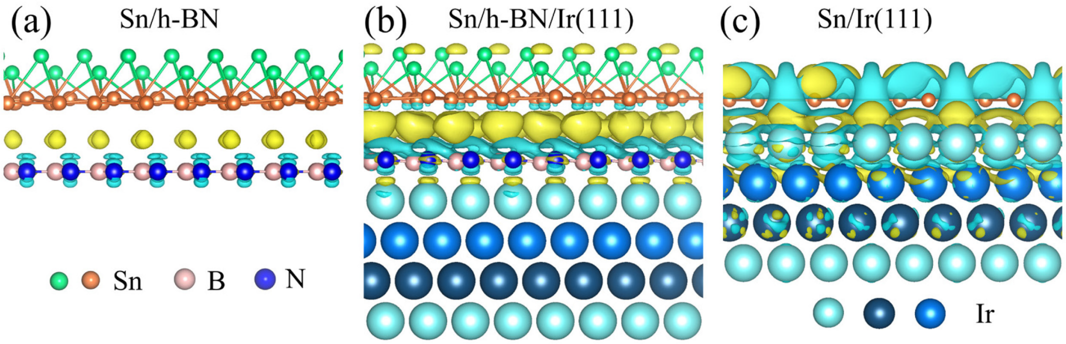

Figure 3-1: Side views of the charge density differences for Sn adlayers on different substrates
(a) Sn/h-BN, (b) Sn/h-BN/Ir(111) at the Moiré pore location, and (c) Sn/Ir(111). The iso-surfaces are 0.0004 e/bohr3. Light yellow and light blue correspond to positive and negative, respectively.

It is clear that the interaction between Sn adlayer and substrate is weaker for Sn/h-BN and Sn/h-BN/Ir(111) systems, and the charge in-between Sn and substrate mainly comes from the substrate (0.006 e/Sn for Sn/h-BN and 0.02 e/Sn for Sn/h-BN/Ir(111)). For Sn/Ir(111), because of the strong chemical bonding between Sn and Ir substrate, the charge in-between comes from Sn and Ir together (0.04 e/Sn from Ir substrate, and 0.11 e/Sn from Sn film) (Figure 3-3). To unambiguously quantify the degree of hybridization between Sn and the substrates, we also evaluate the electronic band structures projected onto Sn atoms on different substrates (Figure 3-3). Here, the color code represents the contribution of Sn states normalized to the states fully contributed by Sn, which means that Sn states with stronger red color indicate more contribution from Sn atoms. For Sn on Ir, the states are dominated by the metallic states of Ir, making the hybridization strong, while Sn on h-BN shows nearly no states from the substrate. Finally, Sn on h-BN/Ir(111) displays similar band structure contour as Sn on h-BN, supporting that h-BN serves as a buffer layer to significantly reduce the interaction between Sn and the metal substrate, but there is still good hybridization between the substrate and Sn atoms.

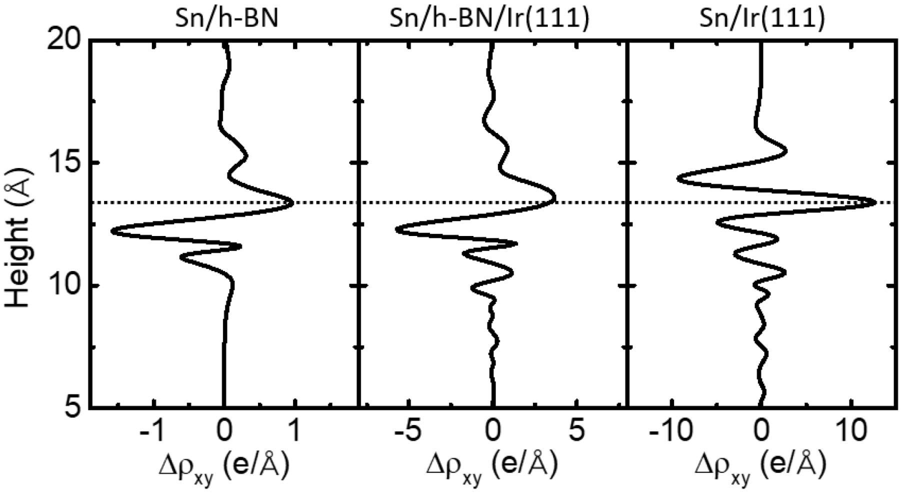

Figure 3-2: The integrated charge density differences for Sn/h-BN, Sn/h-BN/Ir(111) and Sn/Ir(111) systems
The dotted lines correspond to the middle plane between the bottom Sn atoms in the Sn adlayer and the top atoms of the substrates.

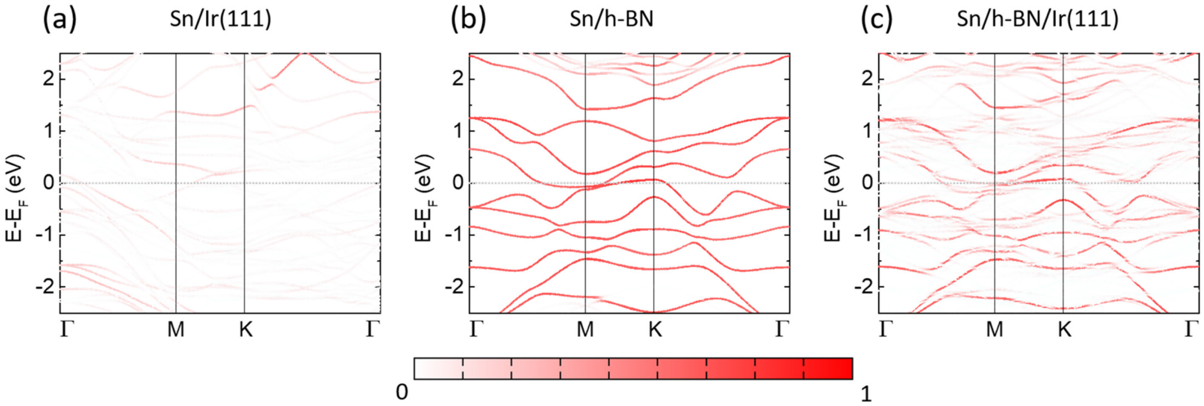

Figure 3-3: Electronic band structures projected onto the Sn atoms on three different substrates, Ir(111), h-BN, and h-BN/Ir(111)
Here the color code represents the contribution of the Sn states, normalized to the states that are fully contributed by Sn. In the calculations, √7 × √7 structure was used for Sn/h-BN and Sn/h-BN/Ir(111), and 2 × 2 structure was used for Sn/Ir(111). Note that (c) illustrates the situation on the locations of Moiré pores.

These calculations clearly demonstrate that the interfacial interaction plays a crucial role on the stabilization of the Sn adlayer.

3.1 2D Sn Growth on Ir(111)

On the Ir(111) substrate, we observe two main phases of Sn: (i) a honeycomb lattice (Figure 3-4(a)) with a lattice constant of 0.55 ± 0.01 nm, which is twice that of the underlaying Ir(111) (~0.274nm), and is therefore referred to as 2 × 2 structure, and (ii) a square-like structure, termed as “p-square” where p stands for planar (Figure 3-4(b)), with an average Sn-Sn distance of 0.34 ± 0.01 nm and $\theta = 86^{\circ} \pm 2^{\circ}$. This translates into a unit cell lattice constant of 1.02 ± 0.02 nm, which is in good agreement with the registry of 3 × 3 Sn to √15 × √15 Ir(111) as marked in Figure 3-4(b). The honeycomb structure is the most stable phase at the growth temperature of ~683K, and when the temperature rises above 873K, the p-square phase becomes dominant. This phase evolution is consistent with the α to β transition in bulk Sn. The motif of the p-square phase originates from the β allotrope of bulk Sn that is stable at and above room temperature.[173] The presence of the substrate helps stabilize the α-derived phase and postpones the α to β transition in thin films.

Both the honeycomb and p-square structures remain atomically flat, indicating a strong interaction with the substrate. Our DFT calculations show that these structures chemically bond to Ir(111) (side view of the optimized structures in Figure 3-4(a-b)) to form covalent bonds with the undercoordinated Ir atoms on the surface, resulting in a significant degree of interfacial charge transfer (Figure 3-1(c)). Note that the in-plane Sn-Sn bonds in the p-square structure can be slightly distorted to register to the substrate sites that have a different crystalline symmetry, as discerned in both the experimental and simulated STM images as well as the DFT optimized structure (Figure 3-4(b)).

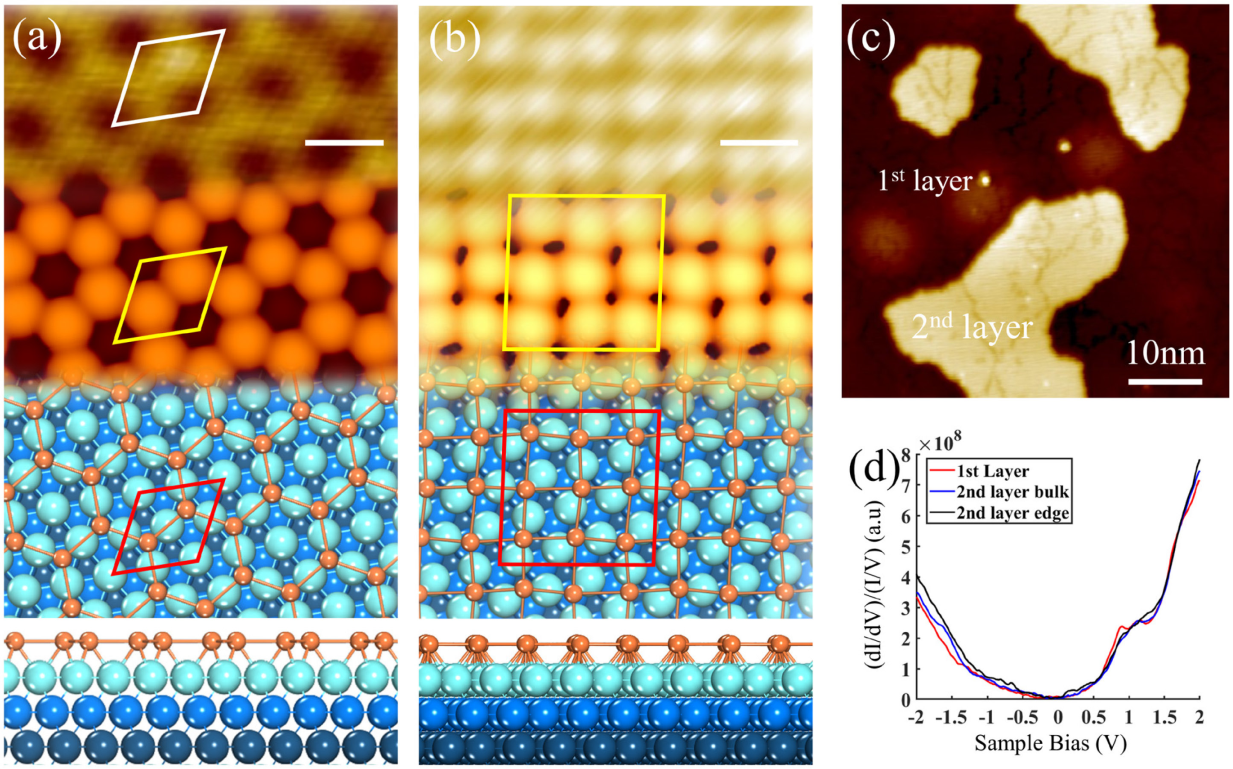

Figure 3-4: Sn growth morphologies and electronic property on Ir(111)
(a) Representative STM image (V_s = -1V, I_t = 30pA), simulated STM image, top and side views of the relaxed configuration of the honeycomb Sn on Ir(111). Rhombic unit cells are illustrated with lattice constant of 0.55 ± 0.01 nm, corresponding to 2 × 2 superlattice of Ir(111). (b) Representative STM image (V_s = 0.1V, I_t = 2nA), simulated STM image, top and side views of the relaxed configuration of the planar square Sn ("p-square") on Ir(111). Yellow and red boxes mark the unit cell, corresponding to the registry between 3 × 3 Sn and $\sqrt{15} \times \sqrt{15}$ Ir(111) with θ =

Figure 3-4 (cont'd)
88°. (c) Large scale STM image of the honeycomb Sn on Ir(111) (V_s = 2V, I_t = 30pA). (d) Normalized dI/dV spectra (setpoint: V_s = 2V, I_t = 200pA) taken on the 1st layer, the interior and edge of the 2nd layer honeycomb Sn, respectively. Scale bars are 0.50 nm in (a,b).

Cu(111) is another substrate with the established growth of 2 × 2 honeycomb lattice,[66] and the alignment between Sn and the metal atoms of the substrate is the same as that of Ir(111), i.e., Sn atoms sit on the hcp and fcc sites of Ir(111). Due to the different lattice constants of Cu(111) and Ir(111) surfaces, 2 × 2 honeycomb Sn on Ir(111) is more (16.4% vs. 8.1%) tensile strained with respect to freestanding stanene. This should be favorable for the topological band inversion at Γ point,[53, 66] however, our STS data (Figure 3-4(d)) taken on the first and second layer (Figure 3-4(c)) of 2 × 2 Sn/Ir(111) suggest metallic behavior in the film. Moreover, the inspection at the center and near edge of the second layer shows no indication of topological edge state other than the disappearance of the kink at ~1.5V on the edge (Figure 3-4(d)). The absence of non-trivial topology near Fermi level (FL) is also reflected in the DFT calculation (Figure 3-3(a)), which could be related to strong hybridization between Sn and Ir substrate, leading to overwhelming DOS from substrate. Note that our DFT calculation reveals that A-A stacking is preferred over A-B stacking for the bilayer structure (Figure 3-5). Nonetheless, the QSH conducting channels, even if existing, may not be electronically isolated on metallic substrates or accessible if it resides far away from FL, and hybridization with substrate significantly alters the physical properties of Sn adlayers.

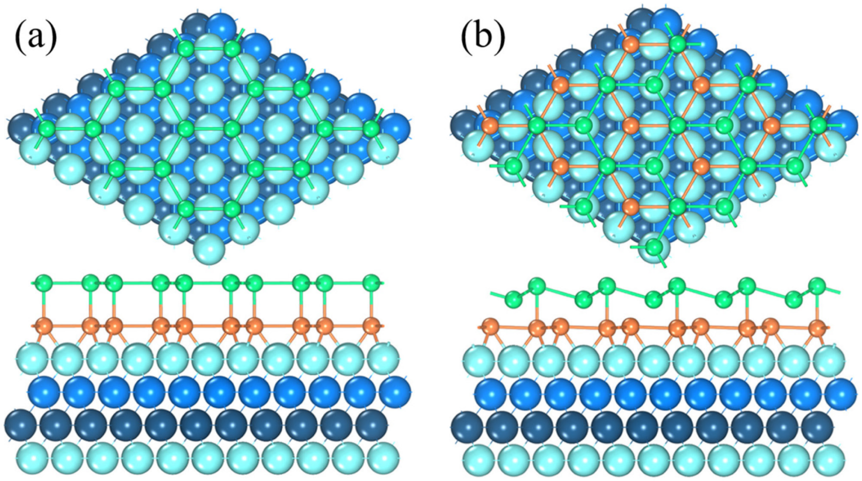

Figure 3-5: Top and side view of bilayer stanene on Ir(111) surface
(a) A-A stacking where the second layer Sn hexagon is organized directly above the first layer and assumes a flat configuration. (b) A-B stacking, in which the second layer is displaced so the center of the hexagon is above an Sn atom in the first layer. A-B stacking yields a buckled second layer.

3.2 2D Sn Growth on Pre-deposited h-BN Monolayer on Ir(111)

Next, we grow h-BN on the Ir(111) surface through the catalytic decomposition process of borazine ($B_3N_3H_6$) using the metal substrate as a catalyst. This process is self-limiting, that is, the catalytic capability of the metal substrate is significantly suppressed once the surface is passivated by a complete h-BN monolayer. Our h-BN/Ir heterostructure is of high quality and forms a Moiré lattice with a periodicity of ~2.90 nm (Figure 3-6), corresponding to approximately 12 × 12 (h-BN) registered to 11 × 11 (Ir).[76] By convention, the depression of the Moiré pattern (Figure 3-6(d)) is called “pore” and the surrounding area is termed “wire”. As indicated in previous reports, the pore area assumes a $B_{fcc}N_{top}$ [183] registry to the Ir substrate, with an absorption height as much as ~0.15nm lower than the wire region.[76] Charge density map on the pore area (Figure 3-1(b) shows a significant charge transfer between h-BN and Ir(111) top layer, whereas h-BN in the wire area can be classified as physisorption owing to the larger spacing and much smaller degree of charge rearrangement.[76] This varying degree of interaction results in h-BN/Ir(111) templates with regions that differ both geometrically and electronically,[76] as reflected in the STS spectra in Figure 3-6(b). The apparent heights of pore and wire regions in the STM images are dominated by DOS contribution, with the pore appearing brighter (dimmer) at positive (negative) 2V bias (Figure 3-6(c-d)).

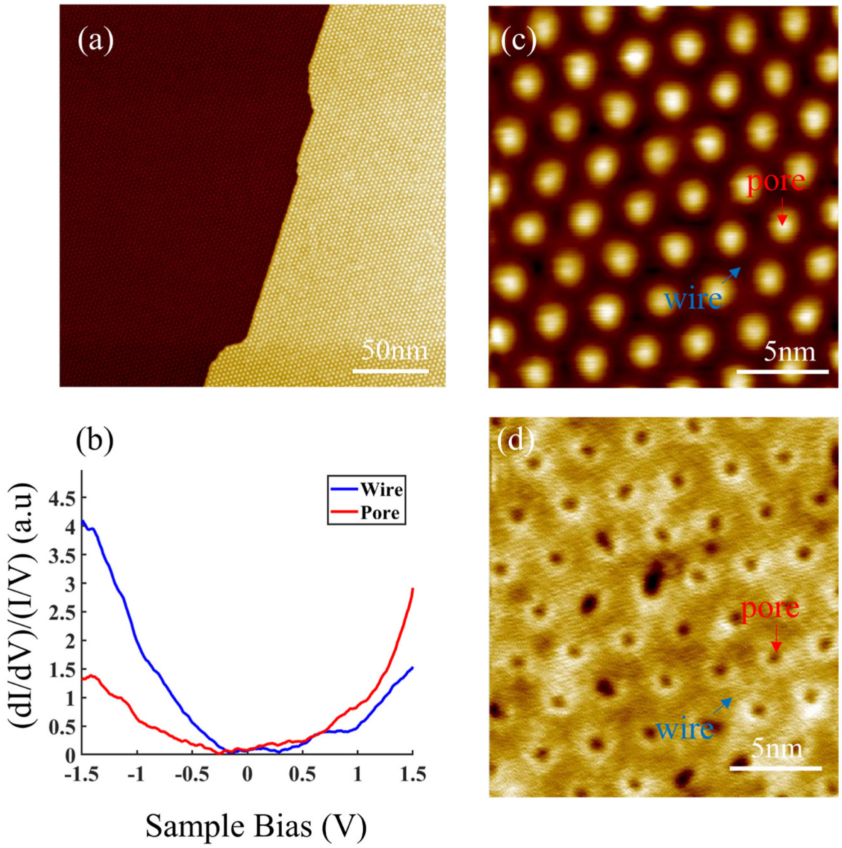

Figure 3-6: Morphology and electronic properties of h-BN/Ir(111)
(a) STM image (V_s = 2V, I_t = 5pA), which shows large-scale and high-quality monolayer h-BN grown on Iridium (111) substrate. (b) normalized STS curves (setpoint: V_s = 1.5V, I_t = 200pA) taken on the pore and wire regions of the Moiré pattern as indicated in c-d. (c-d) zoomed-in STM images of h-BN/Ir taken at V_s = 2V, I_t = 5pA and V_s = -2V, I_t = 5pA, respectively. Note: The tunneling current is established by electrons penetrating the thin insulating h-BN layer, and STS reveals the different degree of modification of the Ir surface states at different locations.

We then grow 2D Sn by evaporating Sn atoms on the h-BN/Ir substrate. After covering the iridium surface with h-BN monolayer, the growth morphology of Sn adlayers is changed drastically (Figure 3-7). Firstly, the square structure on h-BN/Ir(111), referred to as “b-square”, appears to be buckled with lattice constant measured at 0.44 ± 0.01 nm, $\theta = 90^\circ \pm 2^\circ$ (Figure 3-7d).

For the b-square phase, bias-dependent STM images (Figure 3-8(a,c)) are in good agreement with the simulated images (Figure 3-8(b,d)) at the given biases. The buckling is a direct consequence of reduced substrate interaction due to the absence of covalent bonding at the interface, as shown in the simulated configuration (bottom panel in Figure 3-7(d)).

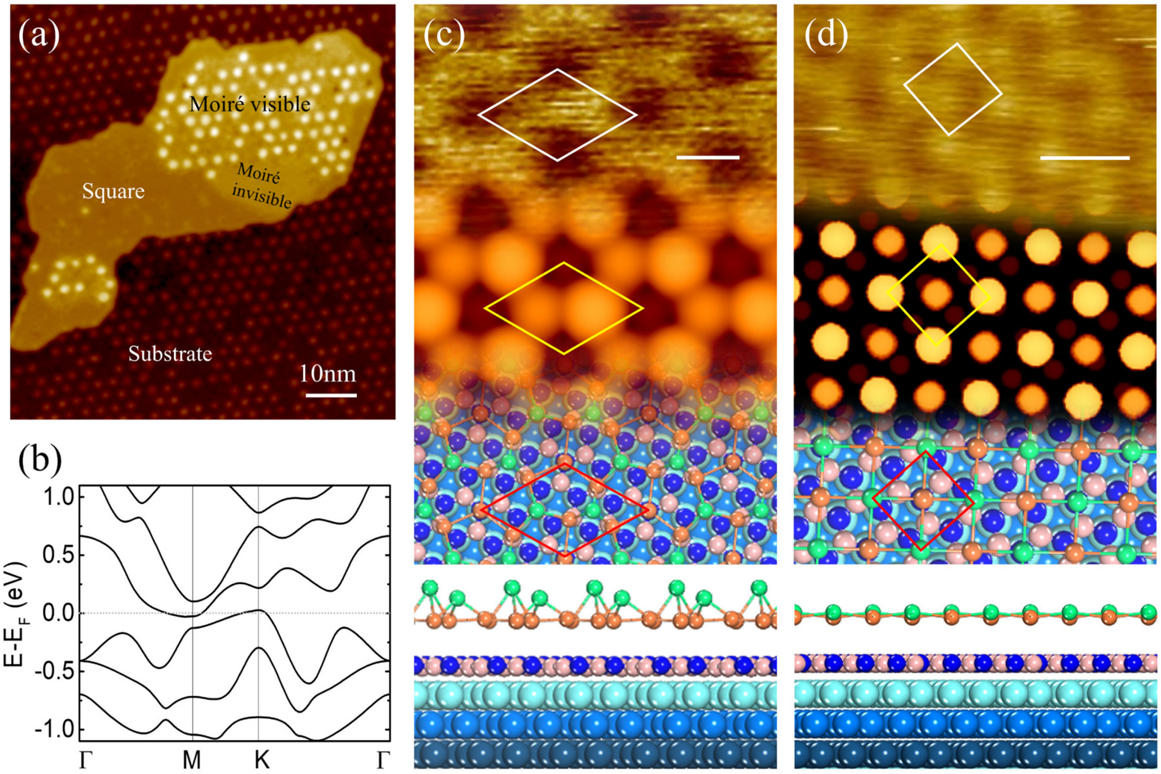

Figure 3-7: Sn growth morphologies on h-BN/Ir(111) and band structure
(a) Large-scale STM image (V_s = 2V, I_t = 5pA) that shows an island with the segregated phases of Sn formed on h-BN/Ir(111). The different phases, as marked on the image, are distinguishable from the contrast variations. (b) DFT calculated band structure derived from the optimized relaxation configuration of the $\sqrt{7} \times \sqrt{7}$ hexagonal phase with lattice constant of 0.718 nm. (c) Representative STM image of (V_s = 2V, I_t = 30pA), simulated STM image, top and side views of the relaxed configuration of hexagonal Sn on h-BN/Ir(111). Rhombic unit cells are illustrated with lattice constant of 0.72 ± 0.01 nm, corresponding to $\sqrt{7} \times \sqrt{7}$ superlattice of Ir(111). (d) Representative STM image (V_s = -0.05V, I_t = 0.8nA), simulated STM image, top and side views of the relaxed configuration of buckled square Sn (b-square). Unit cells are illustrated with lattice constant of 0.44 ± 0.01 nm. Scale bars are 0.50 nm in (c,d).

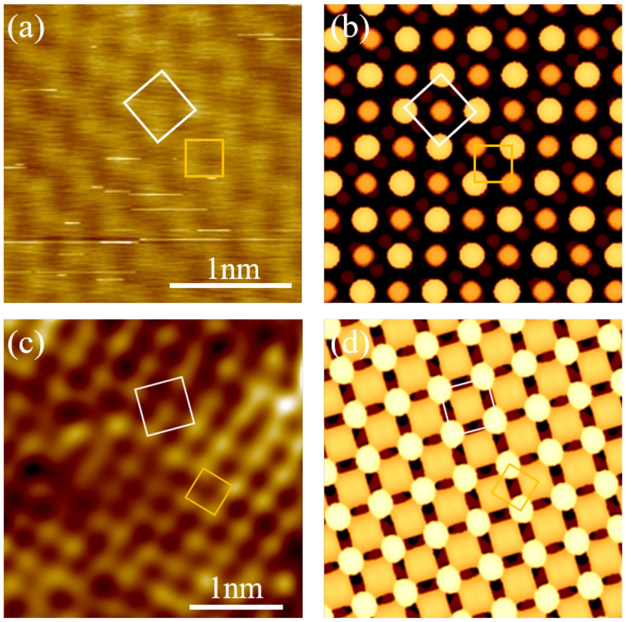

Figure 3-8: Buckled square-like (b-square) Sn on h-BN/Ir(111) at different imaging biases
(a) Representative STM image taken at (V_s = -0.05V, I_t = 0.8nA). (b) Simulated STM image at the same bias as (a). Yellow dots represent Sn atoms in the top layer of the buckled structure, and the orange ones illustrate the atoms in the bottom layer. (c) Representative STM image taken at (V_s = -0.02V, I_t = 1nA). At this condition, tip-sample distance is closer, thus both the top and bottom Sn atoms are revealed more clearly. (d) Simulated STM images at the same bias as (c). Unit cell is outlined by the white box with in-plane distance of 0.44 ± 0.01 nm, and the orange boxes label the nearest neighbor Sn with in-plane distance of 0.31 ± 0.01 nm.

Nevertheless, interaction with h-BN/Ir(111) substrate still plays a role in stabilizing this buckled structure. Secondly, the coexisting of different phases, i.e., “b-square”, “Moiré visible” and “Moiré invisible” hexagonal regions (Figure 3-7(a)), persists through a wide temperature range (~473K to ~1073K). As shown in the STM images (Figure 3-9(b-c)), both the “Moiré visible” and “Moiré invisible” regions reveal an intriguing hexagonal structure with lattice constant of 0.72 ± 0.01 nm, corresponding to √7 × √7 superlattice of Ir(111) (Figure 3-7(c)). The azimuthal rotation between the two neighboring hexagonal structures is ~22 degree (Figure 3-9(a)), originating from its √7 × √7 R19.1° registry with respect to the closely packed direction of the metal substrate, Ir[1 -1 0].[184]

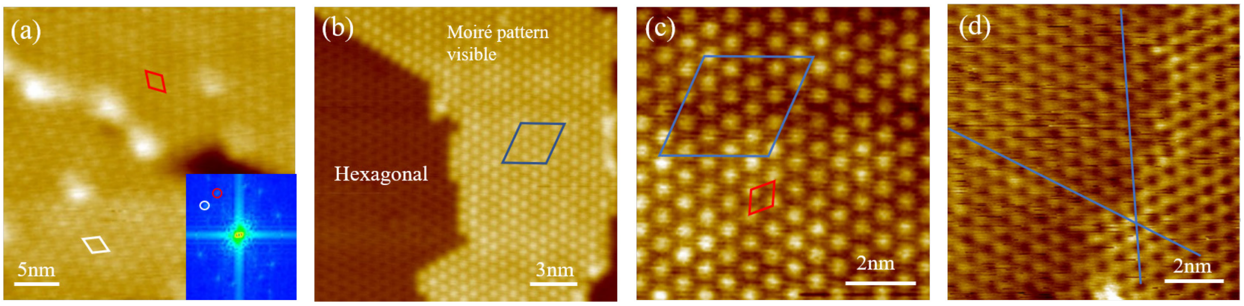

Figure 3-9: Registry and continuity of $\sqrt{7} \times \sqrt{7}$ Sn on h-BN/Ir(111)
(a) STM image (V_s = -2V, I_t = 5pA) displaying rotational angle between neighboring $\sqrt{7} \times \sqrt{7}$ domains. Inset is the FFT of the image, showing ~22° degree angle between the two domains. (b) STM image from randomly functionalized tip (V_s = -2V, I_t = 5pA) showing boundary between Moiré visible (bright stripe) and invisible (left corner) regions of $\sqrt{7} \times \sqrt{7}$. The Moiré of h-BN/Ir(111) is marked by the blue parallel. (c) Zoomed in image of the Moiré visible area that simultaneously shows the underlying h-BN/Ir Moiré pattern and the $\sqrt{7} \times \sqrt{7}$ lattice of Sn adlayer, with unit cells labelled by the blue and red parallels, respectively. (d) STM image (V_s = -1V, I_t = 5pA) showing the continuity of the $\sqrt{7} \times \sqrt{7}$ lattice across the Moiré visible and invisible boundary.

The b-square and $\sqrt{7} \times \sqrt{7}$ phases can be differentiated by color contrast (Figure 3-7), while the phase coexistence agrees with the small formation energy difference (~0.08eV per Sn) between the two (Table 3-1). With increasing substrate temperature (Figure 3-10), the ratio between the b-square phase and the $\sqrt{7} \times \sqrt{7}$ phase increases since β-derived phases are more favored at high temperatures.

Free-standing Stanene	$\sqrt{7} \times \sqrt{7}$ Sn/h-BN/Ir (pore)	$\sqrt{7} \times \sqrt{7}$ Sn/h-BN/Ir (wire)	"b-square" Sn/h-BN/Ir (pore)
544.30 meV/Sn	430.20 meV/Sn	493.50 meV/Sn	511.40 meV/Sn

Table 3-1: Calculated formation energies for different configurations of Sn
Free-standing low-buckled stanene, $\sqrt{7} \times \sqrt{7}$ phase of Sn on the pore location of h-BN/Ir(111) ($B_{fcc}N_{top}$), $\sqrt{7} \times \sqrt{7}$ structure of Sn on the wire location of h-BN/Ir(111) ($B_{top}N_{hcp}$), "b-square" structure of Sn on the pore location of h-BN/Ir(111) ($B_{fcc}N_{top}$). As indicated by the smaller formation energy with respect to the free-standing stanene, interaction with h-BN/Ir(111) substrate plays a stabilizing role for the formation of the $\sqrt{7} \times \sqrt{7}$ and "b-square" structures. Note: The formation energy of $\sqrt{7} \times \sqrt{7}$ structure on two possible pore configurations ($B_{fcc}N_{top}$ or $B_{hcp}N_{top}$) only differs by 0.20 meV/Sn which is within error. Thus, only one configuration is presented.

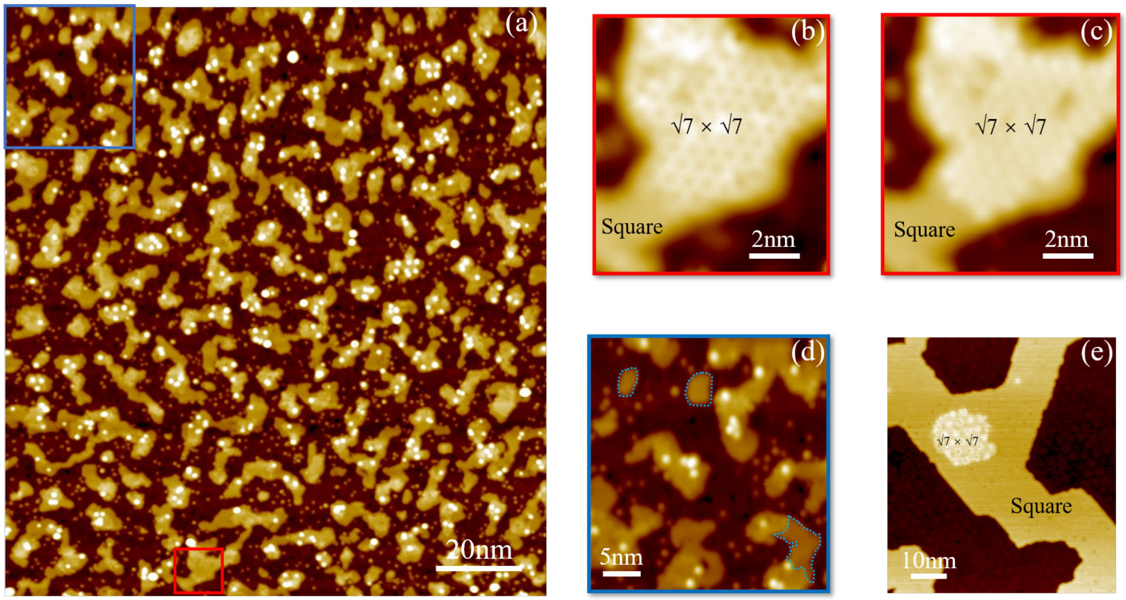

Figure 3-10: Size and temperature dependent of Sn phases on h-BN/Ir(111)
(a) Large scale STM image (V_s = -2.0V, I_t = 5pA) of Sn/h-BN/Ir(111) with substrate treatment up to ~543K. At lower temperature, the diffusion length is shorter, resulting in smaller domains. Different phases (√7 × √7 and b-square) can be differentiated by color contrast, which is clearly observed in the zoom-in STM images of the area outlined by the red box: (b) (V_s = 2.0V, I_t = 50pA), (c) (V_s = -2.0V, I_t = 100pA). (d) Zoom-in image (V_s = -2.0V, I_t = 5pA) of the area outlined by the blue box. A few islands of b-square phase are highlighted: two stand-alone and one on the lower right corner that is partially connected to the islands of √7 × √7 phase. (e) Large scale STM image (V_s = -2.0V, I_t = 5pA) of Sn/h-BN/Ir(111) with substrate treatment up to ~1073K. With increasing diffusion length, both the domain size and the percentile of the b-square phase increase on the surface.

3.3 √7 × √7 Superlattice – A New Phase of 2D Sn

In the intriguing √7 × √7 phase, the superlattice registers to the metal surface, which is exceptionally fascinating as it hints a possibility to remotely tune 2D Sn structure through the h-BN decoupling layer. The formation of the superstructure could be enabled either via hybridization directly to Ir or coupling to a h-BN region that is commensurate to Ir. As discussed earlier, h-BN assumes a $B_{fcc}N_{top}$ registry on Ir(111) at the pore region. We speculate that the √7 × √7 growth is templated by the h-BN/Ir(111) Moiré pattern with the initial nucleation preferentially occurring on the pore. As discussed earlier, significant charge redistribution occurs between $B_{fcc}N_{top}$[183] and Ir, which is expected to give rise to localized surface dipoles to guide the preferred adsorption of

Sn adatoms. With increasing interaction to substrate (Figure 3-1,Figure 3-2,Figure 3-3), the Sn film formation energy at the pore is reduced by ~0.06 eV per Sn in comparison to that at the wire (Table 3-1). The DFT optimization unfolds a trilayer Sn structure (bottom panels of Figure 3-7(c)) configured on the h-BN/Ir(111) pore, and the simulated STM image agrees well with the experiment (Figure 3-7(c) and Figure 3-11). This trilayer structure is derived from the buckled honeycomb stanene[53], with its structure deformed to maximize the interaction with the B and N atoms. Sn-substrate interaction attracts some Sn closer to the B and N atoms, whereas at the same time pushing nearby Sn atoms upward to yield a highly buckled trilayer phase. Owing to the substrate influence, Sn islands initially attempt to conform to the geometrically corrugated Moiré patterns on the substrate, however, as they grow bigger it will be too costly to keep the conformation. As the result, we observe the Moiré invisible region, as marked on the image. The coexistence of Moiré visible and invisible $\sqrt{7} \times \sqrt{7}$ patterns in Sn adlayer reflects the delicate balance between Sn-Sn and Sn-substrate interactions.

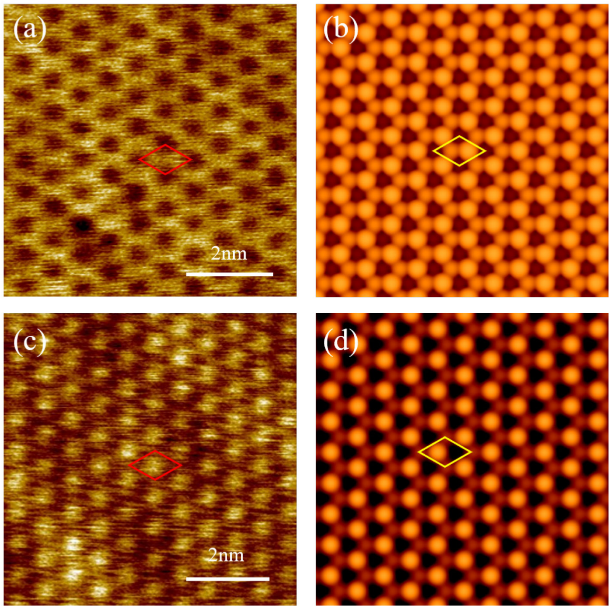

Figure 3-11: $\sqrt{7} \times \sqrt{7}$ Sn on h-BN/Ir(111) at different bias voltages
(a) STM image at (V_s = 2V, I_t = 30pA) and (c) (V_s = -2V, I_t = 30pA). (b) Simulated STM image at 2V and (d) -2V. Rhombic unit cell is illustrated in each structure. The STM images agree very well with simulated images at the same bias.

The new √7 × √7 phase observed in this study is templated by the Moiré patterns of the substrate (h-BN/Ir(111)), specifically, the stronger interaction and charge transfer at the locations of the Moiré pores, as evidenced by the DFT calculations. A rational question is whether the √7 × √7 phase will be relaxed into other forms when the motif of its formation diminishes with the elevation of the structure from the substrate surface. It is known that for a thin film to transform from one phase to another it might need to overcome an energy barrier associated with the phase transition pathway that is larger than the formation energy difference.[185] As shown in Figure 3-7(a), although the interaction strength is weakened when the film is no longer conformal to the substrate, it maintains the √7 × √7 hexagonal structure in the Moiré invisible region.

Experimentally, it will be difficult to argue unambiguously how the growth exactly happened as we are not able to track the real time evolution of the islands. At a lower deposition temperature (~543K, Figure 3-10(a)), the islands are smaller. The b-square and √7 × √7 phases are differentiable by the color contrast (Figure 3-7(a), Figure 3-10(b-c)). In Figure 3-10d, two isolated b-square-phase islands are identified, suggesting that both b-square and √7 × √7 phases can be formed independently which agrees with the small formation energy difference calculated by DFT (Table 3-1). As the segregated b-square and √7 × √7 phases encounter each other, they will be merged into one island, similar to that observed in Figure 3-7a. With increasing substrate temperature (~1073K, Figure 3-10(e)), the ratio between the b-square phase and the √7 × √7 phase increases since β-derived phases are more favored at high temperatures. At last, for the √7 × √7 domain, the moiré visible region is typically larger than the moiré invisible region (Figure 3-7(a) and Figure 3-10(e)), consistent with the fact that √7 × √7 is stabilized by the interaction to substrate particularly over moiré pore locations.

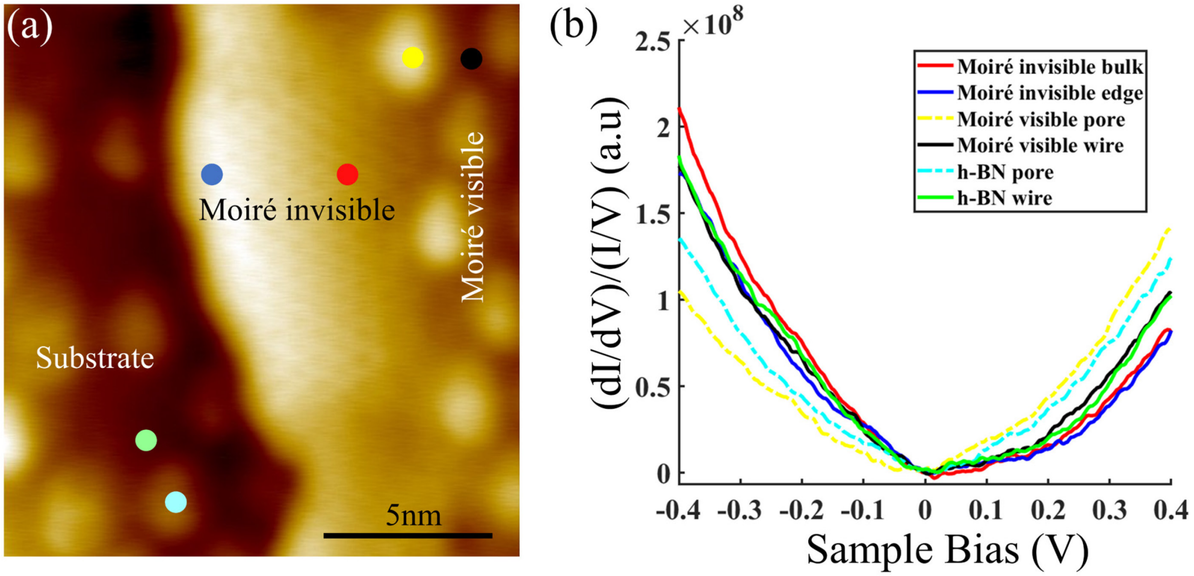

Figure 3-12: Representative STS curves at various locations of Sn adlayer on h-BN/Ir(111) (a) STM image (V_s = 2V, I_t = 5pA) that shows the segregated phases of Sn formed on h-BN/Ir(111), with the presence of partially exposed substrate. (b) Normalized dI/dV spectra (setpoint: V_s = 0.2V, I_t = 150pA) taken on the marked locations with corresponding colors on (a). By comparison, STS curves can be categorized into two groups: spectra from pore locations (dash lines), and spectra from wire locations or Moiré invisible hexagonal regions (solid lines).

STS spectra taken at the interior and edge locations of Moiré invisible $\sqrt{7} \times \sqrt{7}$ superlattice (red and blue curves in Figure 3-12(b)) reveals metallic electronic structure of the Sn adlayer, which agrees with the band structure calculation (Figure 3-12(b)). Nonetheless, investigations on electronic structures over various locations of the film, such as the $\sqrt{7} \times \sqrt{7}$ "Moiré invisible" and "Moiré visible" regions, reveal a dominant substrate DOS (Figure 3-12(b)). Specifically, STS over the "Moiré invisible" region is very similar to the spectrum taken on the wire area of the h-BN/Ir(111) substrate, and the curve taken above the pore (wire) location on the Moiré visible region, i.e., the yellow (black) curve on Figure 3-12(b), is similar to the spectra on the corresponding pore (wire) area of the substrate without Sn adlayer. The substrate-dominated DOS features in the STS likely originate from the insensitivity of STS to states of large parallel momentum ($k_{\parallel}$) (more discussion in the section 2.2.5, Equation(2-17)).[186] As shown in the calculated band structure in Figure 3-7(b), the low energy features of √7 × √7 superlattice are located at points with large parallel momentum. When tip-sample distance is reduced to increase the contribution from these states, tip is also getting closer to the substrate, and substrate electronic features begin to overwhelm the overall DOS. Although STS curves taken above the various locations of 2D Sn all display metallic behaviors, it is difficult to distinguish the DOS features of the thin film from those of the substrate.

Finally, it is important to note that during high temperature treatment, desorption and intercalation of Sn are both possible to occur. However, our results strongly suggest that the deposited films are on top of h-BN. First, the observation of the intrinsic h-BN/Ir(111) Moiré pattern on the "Moiré visible" region indicates that the film is on top of h-BN. Although one can argue partial intercalation at the "Moiré invisible" region, the continuum of the atomically resolved √7 × √7 lattice across the boundary between "Moiré visible" and "Moiré invisible" regions, as shown in Figure 3-9(b-d), strongly indicate the opposite. Secondly, if Sn were intercalated and directly contacting the Ir(111) surface, we would not have observed the drastically different growth morphologies on h-BN/Ir(111) and Ir(111).

3.4 Discussion

As point out in introduction, the structure of the Sn thin film is highly adaptable,[53, 71] For the same, low-buckled honeycomb stanene the electronic properties can also vary from experiment to experiment.[65, 72, 73] Substrate interactions [53, 66], and thickness[74] are the main factors that sensitively modulate Sn films.

While the novel 2D √7 × √7 Sn structure discovered in this study is a trivial metal, its electronic structure remains strongly dependent on the strain, much similar to the case of low-buckled honeycomb stanene[53]. Our DFT calculation reveals the opening of a bandgap under a slight tensile strain (Figure 3-13). From the investigations of the √7 × √7 phase, we have unraveled a unique interaction scheme between Sn monolayer and metal substrate mediated by the h-BN "decoupling" monolayer. This study offers significant insights and useful guidelines for the search and investigation of 2D Sn phases on h-BN/metal where Moiré patterns are universally present.

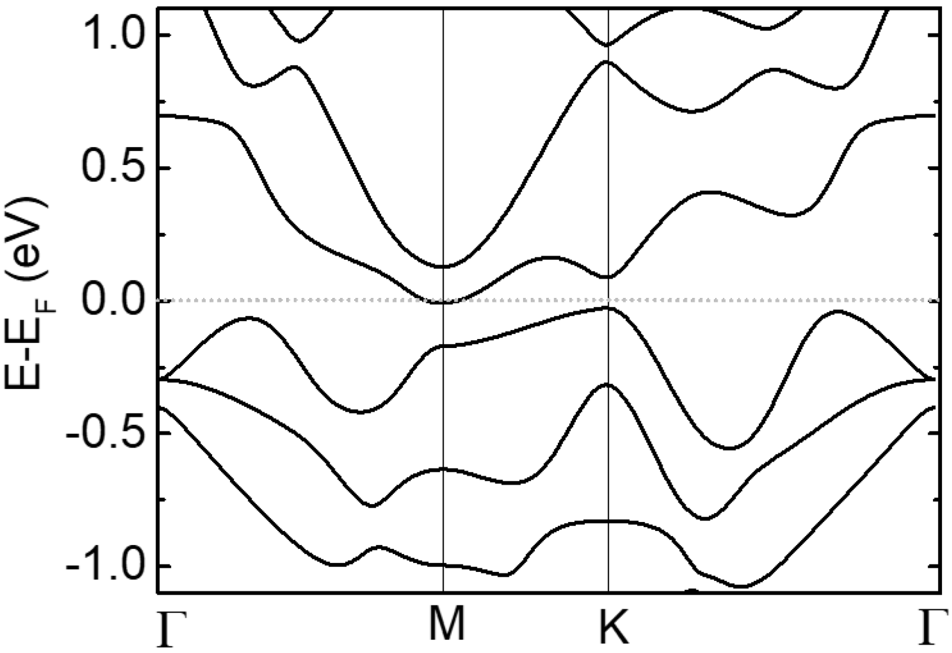

Figure 3-13: Band structure evolution of √7 × √7 Sn with strain
Band structure with lattice constant of 7.24 Å. In comparison to (Figure 3-7(b)), bandgap can be opened with a tensile strain.

Also mentioned in the introduction that h-BN/metal is a versatile system, where the strength of h-BN to metal interaction can be rationally tuned by two different methods, i.e., change of metal substrate with different *d*-orbital occupancy and intercalation of foreign atoms between h-BN and metal substrate.[75] Accordingly, the coupling between Sn structures and h-BN/metal substrate will be strengthened or weakened. Various degree of strain may also be introduced into Sn structures by varying the metal substrate of different lattice constants. Thus, h-BN/metal will potentially provide a new avenue for engineering electronic properties of 2D Sn and achieving new topological phases with high thermodynamic stability that warrants future studies.

3.5 Conclusion

Through combined experimental and theoretical investigations, we reveal various structures of Sn on Ir(111) and h-BN/Ir(111) substrates. The difference in growth morphology is connected to the various interaction scheme with substrate, as manifested by the degree of charge transfer and redistribution, which could be further tuned by the metal support in h-BN/metal system. Our results offer useful insights into phase engineering of Sn via remote epitaxy through the h-BN decoupling layer.

4 Semiconductor to Topological Insulator Transition Induced by Stress Propagation in Metal Dichalcogenides Core-Shell Lateral Heterostructures

As pointed out earlier, polymorphic phase transition is an important route for engineering the properties of two-dimensional materials.[55] Heterostructure construction, on the other hand, not only allows the integration of different functionalities for device applications, but also enables the exploration of new physics arising from proximity coupling.[187-190] Yet, implementing a design that incorporates the advantages of both remains underexplored. Nonetheless, except for 1T′-WTe_2, T′-phase of group VI TMDs are metastable[58] and thus remain difficult to access,[55] creating additional barriers for HSs integration. Direct synthesis is typically carried out at conditions far from equilibrium,[191] restricting the quality, e.g., domain size of the film, whereas phase transition triggered by mechanical stress or electron doping might introduce structural damage[192] and/or additional source of contamination.[193] As substrate is the indispensable part of devices, substrate-induced phase transition has also been explored, mainly attributed to interfacial charge transfer arising from the strong/hybridizing interaction at the interface, which unavoidably amounts to large electronic perturbation.[170] To better control electronic properties and to readily incorporate with HSs, it is imperative to develop more robust and versatile phase engineering methodologies that put less constraints on the choice of substrates or the heteroepitaxial design.

In this Chapter, we demonstrate a novel technique that combines the phase engineering and HS construction in one step. H to T′ phase transition is realized in WSe_2 upon the bottom-up construction of WSe_2/$SnSe_2$ core-shell lateral HS by MBE. STM/S and first-principles DFT studies reveal the semiconductor to TI transition associated with the polymorphic change of WSe_2 and exclude electron doping as the origin of phase transition. In addition to the observation of misfit dislocations which relax the epitaxial strain at heterojunctions,[101, 102] we propose a novel phase transition mechanism that involves the propagation of stress from shell to core mediated through the covalently bonded core-shell boundaries. Topological edge state is proved to be robust against local perturbations from misfit dislocations. Since $SnSe_2$ becomes superconducting at low temperatures, WSe_2/$SnSe_2$ lateral HS with the directly exposed boundary on surface provides a valuable platform for future investigations into topological superconductivity and spatial extent of proximity coupling. This chapter is adapted from Reference[171]: *X. Dong et al. Mater. Horiz. 2021,* ***8,*** *1029-1036).*

4.1 Observation of H to T′ Phase Transition in WSe_2 Core

WSe_2/$SnSe_2$ core-shell architectures were grown on HOPG via sequential MBE deposition of WSe_2 and $SnSe_2$ (see Section 2.1.4 for details). Thermodynamically stable H-phase of WSe_2 was formed initially, with substrate held at ~723K,[67] as confirmed by the lattice measurements shown in the inset of Figure 4-1(a).[194] For the subsequent $SnSe_2$ deposition, substrate temperature was lowered to ~438K to avoid the decomposition of $SnSe_2$ and the formation of alloy. Inset of Figure 4-1(b) reveals atomically resolved 1T-$SnSe_2$ that preferentially nucleates along the edges of existing WSe_2 islands. Intriguingly, approaching the formation of enclosed architecture, characteristic stripe-like features emerge on WSe_2 core (Figure 4-1 (c-e)). These lateral heterostructures that are composed of a WSe_2 inner "core" and a $SnSe_2$ outer "shell" are termed core-shell architecture in this article. The striped phase with structure illustrated in the inset of Figure 4-1(e) is commonly referred to as T′-phase,[62, 63] suggesting a H to T′ phase transition in WSe_2 core. After $SnSe_2$ fully encloses WSe_2 island, a 2D lateral heterostructure with the inner WSe_2 core and outer $SnSe_2$ shell is effectively created.

The apparent height measurements were conducted on the same core-shell structure on 1H-WSe_2/HOPG substrate (Figure 4-2). The heights of monolayer T′-WSe_2 and T-$SnSe_2$ at 2V are

~0.70nm and ~0.68nm, respectively, which agree well with the typical monolayer thickness (0.6-0.7nm) of metal dichalcogenides from theoretical calculations,[167] as well as previous STM measurements of the same materials.[67, 195] However, it should be noted that the apparent height or the contrast in an STM image is convoluted between the film morphology and electronic structure, and thus can be influenced by the scanning conditions.[196] 1T′-WSe_2 core may appear slightly taller (brighter) or shorter (dimmer) than the surrounding $SnSe_2$ shell at different sample biases due to the contribution of electronic structures that are different between $SnSe_2$ and 1T′-WSe_2 (Figure 4-2). Nevertheless, the apparent heights of the core measured at all biases are well below the thickness of bilayer metal dichalcogenides, which confirms the lateral geometry of the heterostructure.

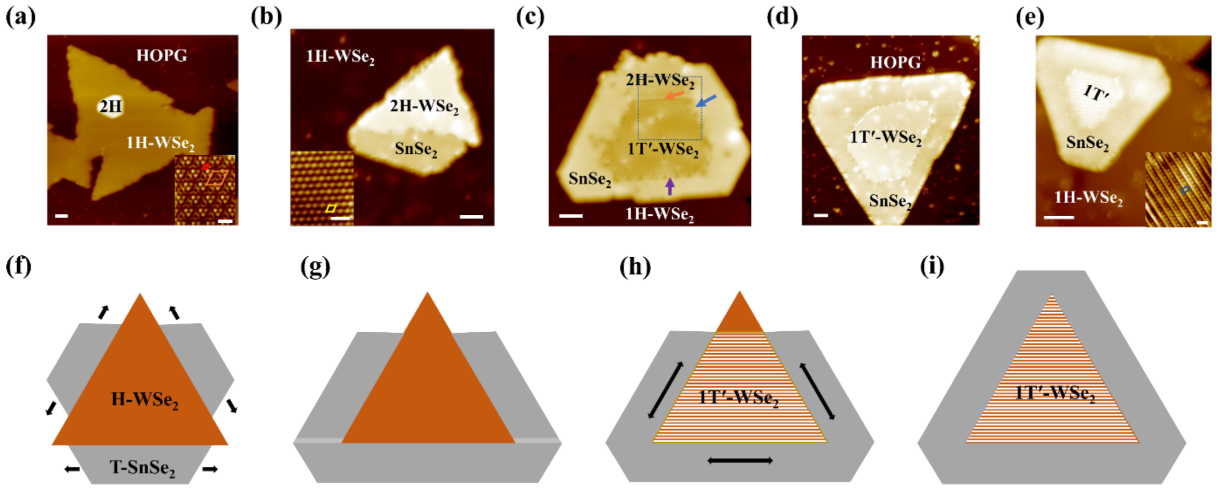

Figure 4-1: Phase transition in $SnSe_2$-surrounded WSe_2 islands
(a) STM image of H-WSe_2 grown on HOPG (V_s = 1.5V, I_t = 5pA). Inset: Atomically resolved image of 1H-WSe_2 (V_s= 1.3V, I_t = 30pA). Red and brown rhombic depict the unit cells of 1H-WSe_2 and the (3 × 3) Moiré pattern of 1H-WSe_2 on HOPG, respectively. (b) $SnSe_2$ preferentially nucleated along the edges of WSe_2 island (V_s = -2.0V, I_t = 30pA). Inset: Atomically resolved image of 1T-$SnSe_2$ (V_s = 1.3V, I_t = 30pA). Yellow rhombic marks the unit cell. Lattice constants are measured to be $a_1 = b_1 = 0.33 \pm 0.02$ nm, $\alpha_1 = 58^\circ \pm 2^\circ$ for 1H-WSe_2 and $a_2 = b_2 = 0.39 \pm 0.02$ nm, $\alpha_2 = 57^\circ \pm 2^\circ$ for 1T-$SnSe_2$. (c) Incomplete H to T′ phase transition when WSe_2 island is not fully surrounded by $SnSe_2$ (V_s = 2V, I_t = 30pA, 5nm scale bar). Orange arrow marks boundary between the H- and T′-phases of WSe_2. Blue and purple arrows label arc-like features at the boundaries between 1T′-WSe_2 and 1T-$SnSe_2$. The dashed box depicts an area that will be zoomed in Fig. 5(a).

Figure 4-1 (cont'd)
(d-e) 1T′-WSe_2 (core)/1T-$SnSe_2$ (shell) HSs on: (d) HOPG (V_s = 1.5V, I_t = 5pA) and (e) 1H-WSe_2/HOPG (V_s = 1.6V, I_t = 30pA). Inset: Atomically resolved image of 1T′-WSe_2 (V_s = -0.1V, I_t = 100pA). Blue rectangle illustrates the unit cell, with the lattice constants of $a = 0.34 \pm 0.02$ nm, $b = 0.60 \pm 0.02$ nm, and $\alpha = 88^\circ \pm 2^\circ$. (f-i) Schematics of structural evolution correlating to the STM images with increasing shell coverage. Light grey in (g) depicts the shell merging front. Black double arrows in (h) illustrate the direction of shear stress and gliding motion. Scale bars: 1nm for insets and 5nm for others.

The observed phase transition is closely related to the degree of $SnSe_2$ coverage surrounding H-WSe_2 islands, as depicted in the schematics in Figure 4-1(f-i), but is likely independent of the substrate as the T′-phase is identified on both HOPG (Figure 4-1(d)) and 1H-WSe_2/HOPG (Figure 4-1(e)). As mentioned earlier, phase transition can be triggered by mechanical stress[192] or electron doping.[170, 193] Both need to be considered since the coverage-dependent trend could be associated with the increase in either charge transfer or strain at the core-shell boundary.

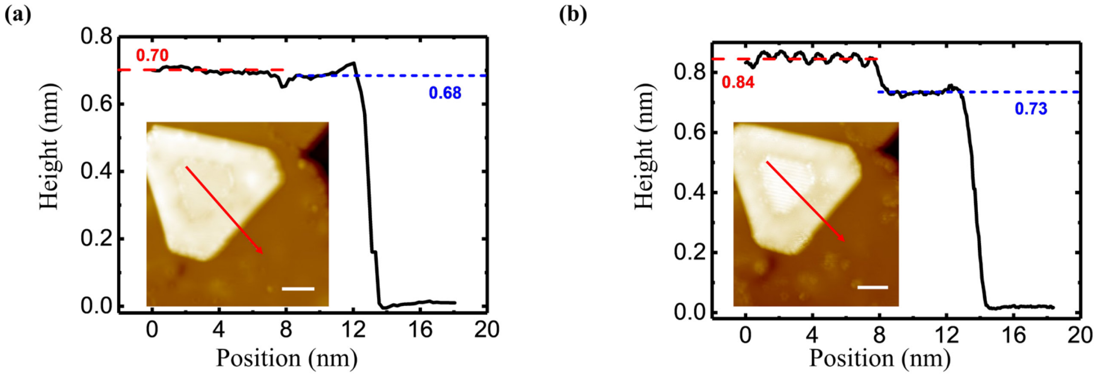

Figure 4-2: Bias-dependent apparent height measurements on the same core-shell structure
(a) Line profile measurement across the red trace on the inset STM image (V_s = 2.0V, I_t = 30pA). The apparent height for T′-WSe_2 and $SnSe_2$ are ~0.70nm and ~0.68nm, respectively. (b) Line profile measurement across the red trace on the inset STM image (V_s = 1.6V, I_t = 30pA). Due to the convolution between morphology and electronic structures in STM measurements, the apparent heights of T′-WSe_2 and $SnSe_2$ are slightly modulated at a different sample bias. The ripples are related to the strip features of 1T′-WSe, which become more pronounced at this scanning condition. Scale bar: 5nm.

4.2 Investigation of Charge Transfer Behaviors by STM/S

We first examine the charge transfer behaviors in the system prior to phase transition, i.e. 1H-WSe_2:1T-$SnSe_2$ (1H/1T) lateral HS on HOPG. H to T′ phase transition in the scheme of charge transfer requires excess electrons, i.e., electron doping. Metastable T′ phase of group VI TMDs has a higher total energy than the stable H phase,[58] however, the CBM of T′ phase lies in a much lower energy level than that of the H phase, originating from the *d*-orbital arrangement.[197] Thus, injection of excessive electrons is expected to bring the total energy of H phase above that of T′ phase, inducing phase transition by switching the ground state to T′.[198] Since the 1H/1T HS is anticipated to reach charge equilibrium with the underlying substrate, interfacial band alignment needs to be established. As depicted in Figure 4-3, STS curves taken on the interior of 1H-WSe_2 and 1T-$SnSe_2$ domains far from the lateral boundary agree well with the previous reports of the respective pristine monolayers on graphene.[147, 186] The extracted quasiparticle bandgap (~2.50eV) for 1H-WSe_2 is significantly larger than the optical bandgap (~1.60eV)[199] which is mainly attributed to the large exciton binding energy.[200, 201] Meanwhile, the insensitivity of STS to electronic states of large parallel momentum could also contribute to the overestimation of quasiparticle bandgap (more discussion in the section 2.2.5, Equation (2-17)). 1H-WSe_2 appears to be nearly charge neutral with FL residing at the middle of the bandgap. Thus, phase transition is unlikely the result of interfacial charge transfer with substrate. On the other hand, due to the relatively high work function of $SnSe_2$ (~5.3eV),[202] electrons are transferred from HOPG to $SnSe_2$, pulling its CBM down to the FL.

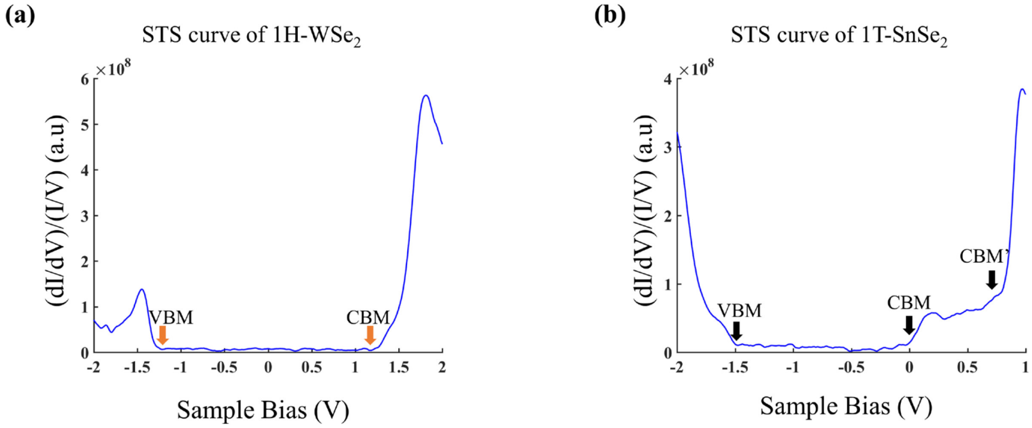

Figure 4-3: STS spectra taken on the interiors of 1H-WSe_2 and 1T-$SnSe_2$ on HOPG
(a) Representative normalized dI/dV (setpoint: $V_s = 2.0V$, $I_t = 300pA$) taken on the interior of 1H-WSe_2. Orange arrows mark the locations of band edges. The apparent bandgap is determined to be ~2.50 eV, with the VBM located at ~-1.27 eV and CBM located at ~1.23 eV. (b) Representative normalized dI/dV (setpoint: $V_s = -1.3V$, $I_t = 200pA$) taken on the interior of 1T-$SnSe_2$. There are three characteristic features labelled as VBM, CBM' and CBM. The identification of the band edges provides basis for the tracking of band bending in Figure 4-4(a) and (b).

After establishing band alignment with the substrate, we explore the charge transfer behaviors across the 1H/1T lateral heterojunction by extrapolating the band structure evolution towards the boundary using spatially resolved STS. As illustrated in the vertically offset STS curves and the corresponding density of states (DOS) heatmaps in Figure 4-4(a-b), a clear upward band bending is witnessed on both sides of the boundary by tracing the onsets of VBM and CBM. This indicates that electrons are depleted from both domains and accumulated at the boundary, which renders electron doping an unlikely origin of the phase transition observed in this study.

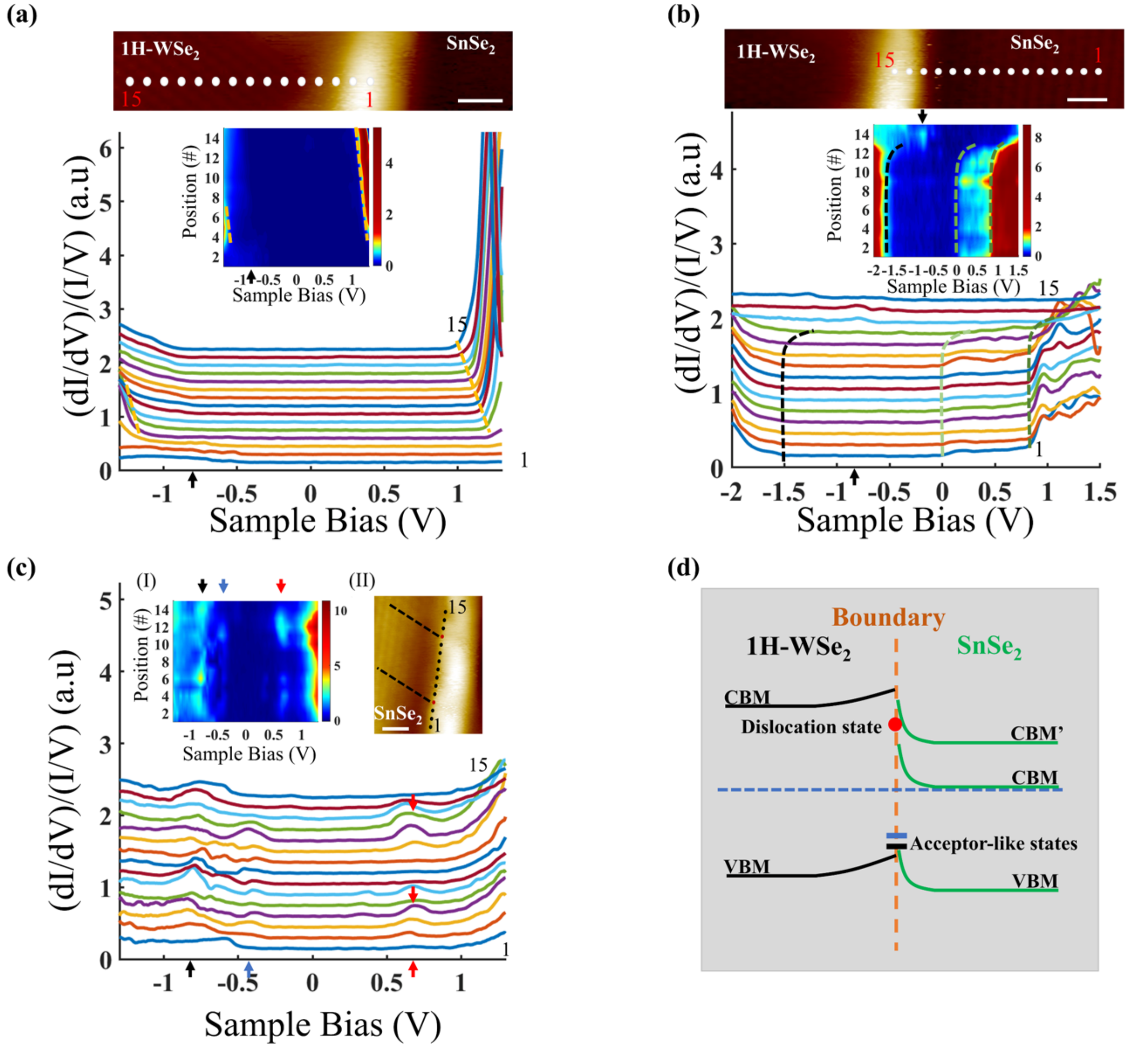

Figure 4-4: Electronic structures and band bending behavior near boundaries of 1H-WSe$_2$ and 1T-SnSe$_2$

(a-c) Vertically offset normalized dI/dV spectra taken on the 15 equally spaced points from the interior of 1H-WSe$_2$ or 1T-SnSe$_2$ to the boundary and along the boundary as marked on the respective STM images. Insets: DOS heatmap with x-axis, y-axis, and color representing sample bias, point number, and (dI/dV)/(I/V), respectively. In (a), towards the boundary (point 15 to point 1), a gradual upward band bending is identified in the WSe$_2$ domain by tracing the shifts of band edges (orange dashed lines) on both the spectra and heatmap. In (b), three distinct spectra features associated with the electronic structure of SnSe$_2$ are revealed, corresponding to VBM (black trace), CBM (light green trace) and CBM' (dark green trace). A steep upward band bending is observed near the boundary. In (c), acceptor-like states at the negative sample bias, as highlighted by black and blue arrows, persist throughout the entire boundary. Meanwhile, the intensity of the peak at ~0.65V (red arrows) is spatially modulated, which is expected to correlate to misfit dislocations. Specifically, the red dots in STM image (inset II) mark the locations (points 4 &12) of the maximum peak intensity at ~0.65V, which corresponds to a distance of 6 times SnSe$_2$ lattice constant (~2.30nm) by tracing along the high symmetry direction in SnSe$_2$ domain (black dashed

Figure 4-4 (cont'd)
lines). (d) Schematic diagram to illustrate the generic band alignment and the evolution of CBM and VBM energy levels with respect to the physical position towards the 1H-WSe_2/1T-$SnSe_2$ boundary. Setpoint for normalized dI/dV spectra (V_s = -1.3V, I_t = 200pA). Bias for STM images (V_s = -1.3V, I_t = 30pA). Scale bars: 1nm.

To further comprehend the nature of boundary states and their correlation to the boundary structural configuration, STS was conducted along the boundary. Figure 4-4(c) reveals "acceptor-like" boundary states that arise near VBM, along with a state residing at ~0.65V. The "acceptor-like" states persist over the entire boundary, responsible for trapping electrons from the nearby domains, whereas the state at ~0.65V displays a modulated peak intensity along the boundary, correlating to the periodic boundary features observed in the inset (II). Due to the significant DOS contribution, boundary morphology cannot be atomically resolved. Nonetheless, as guided by lines drawn along the high symmetry direction of the hexagonal WSe_2 and $SnSe_2$ lattices (Figure 4-5(a)), a 7:6 WSe_2 (red lines) to $SnSe_2$ (yellow lines) alignment was identified across the boundary, which translates into a boundary periodicity of ~2.3nm and implies the formation of misfit dislocations for relaxing the significant strain of ~15% between the two domains.[101, 102] Naturally, we suspect the electronic state arising at ~0.65V to be affiliated to misfit dislocations.

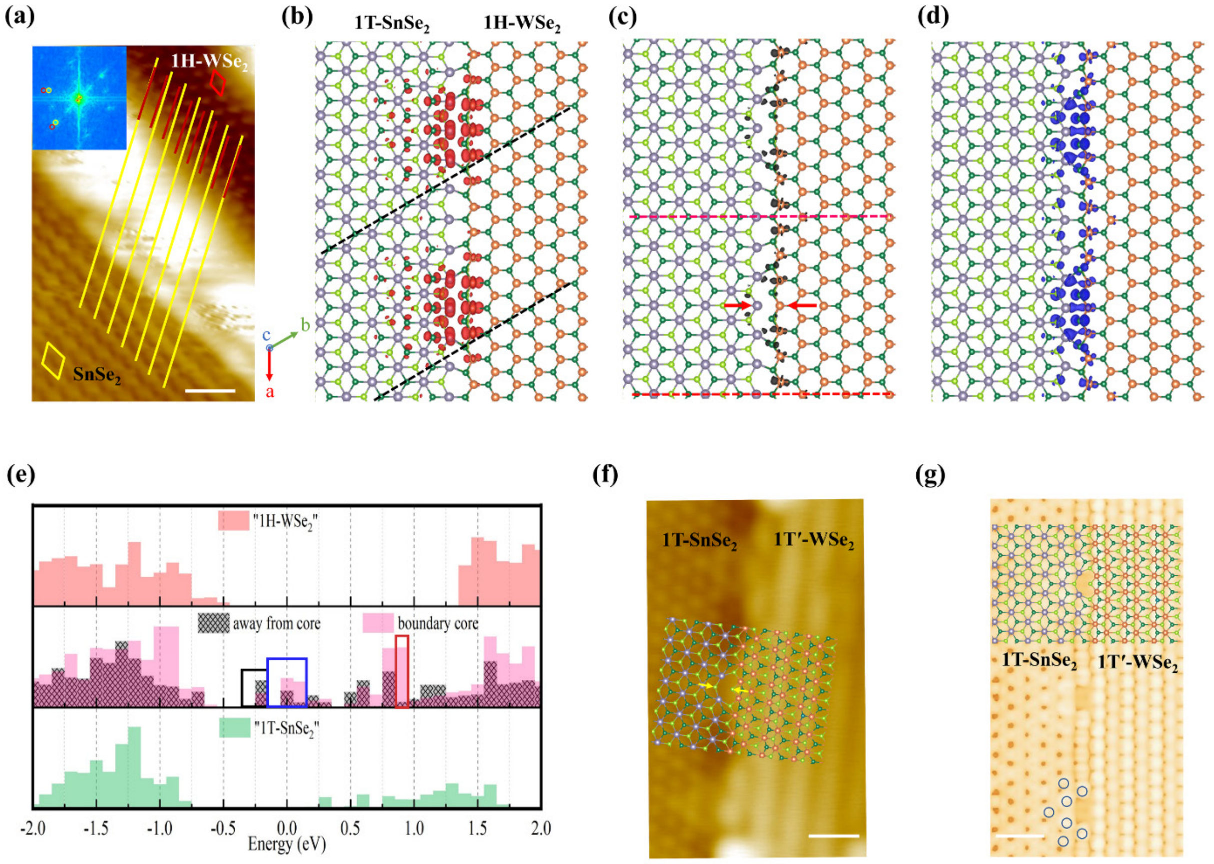

Figure 4-5: Impacts of misfit dislocation on morphologies and electronic states of 1H-WSe$_2$/1T-SnSe$_2$ and 1T′-WSe$_2$/1T-SnSe$_2$ boundaries

(a) STM image (V_s = -1.3V, I_t = 100pA) of 1H-WSe$_2$/1T-SnSe$_2$ lateral HS grown on HOPG. Unit cells of the two domains are labelled by the red and yellow rhombic, respectively. Inset: fast Fourier transformation (FFT) of the STM image, where the red and yellow circles correspond to the diffraction spots of WSe$_2$ and SnSe$_2$ lattices, respectively. 1H-WSe$_2$ and 1T-SnSe$_2$ domains are azimuthally aligned within the experimental error, evidenced by the STM image and its FFT. (b-d) Simulated atomic structure and charge density plots in the energy ranges of: (b) 0.9 – 1.0 eV, (c) -0.3 – -0.1eV, and (d) -0.1 – 0.2eV, corresponding to the red, black, and blue boxes outlined in (e). A fixed isovalue of 0.002 e/Bohr^{-3} is used in all charge density plots. Silver-colored atoms represent Sn, brown for W, dark green for top Se, and light green for bottom Se. The black dashed lines in (b) are drawn along a high-symmetry direction of top Se atoms to illustrate the boundary periodicity, and the red arrows in (c) mark the center of a dislocation core positioned in the middle of a 7:6 periodic boundary segment as outlined by the red dashed lines perpendicular to the boundary. (e) Projected density of states (PDOS) plotted in histograms with the 0.1eV spacing, are compared across the center of each domain (top and bottom panels) and the different locations at boundary (center panel). (f-g) Atomic structure and morphology of 1T′-WSe$_2$/1T-SnSe$_2$ boundary: (f) STM image of 1T′-WSe$_2$/1T-SnSe$_2$ boundary (V_s = 1.0V, I_t = 100pA) with DFT simulated atomic structure overlaid on top. Yellow arrows mark the center of dislocation core. (g) Simulated STM image of the HS at 1V. The appearance of star-shaped features outlined by blue circles and their periodicity along boundary all match well with the STM image in (f). scale bars: 1nm.

4.3 First-principles Calculations of Boundary Morphology and Electronic Structures

To confirm our hypothesis, optimized 1H/1T boundary structure was calculated using density functional theory (DFT), which reveals the formation of dislocations centered on the (7:6) segment (Figure 4-5(c)). In the construction of (7:6) 1H-WSe_2 to 1T-$SnSe_2$ alignment, Se-terminated zigzag edge is considered the most likely termination for 1H-WSe_2 due to the Se-rich environment during MBE growth,[203] and subsequent deposition of $SnSe_2$ yields a covalently bonded lateral heterojunction. The optimized boundary structure illustrates the formation of dislocations, marked by the red arrows in Figure 4-5(c), that are centered along the (7:6) segment as guided by the red dashed lines. Nonetheless, with respect to the black dashed lines drawn along the high symmetry direction of top Se atoms (Figure 4-5(b)), the dislocation core appears to be shifted away from the center, consistent with the STM image in Figure 4-5(a). Note that the periodic bright dots observed in the STM image correspond to the top Se atoms of TMDs due to STM sensitivity to tip-sample distance.

To identify boundary electronic structures, projected density of states (PDOS) are compared among various locations at the boundary as well as within the domain interiors (Fig. 3(e)). Real space charge density plots in Figure 4-5(b-d) further elucidate the origins of the boundary states, i.e., the one enclosed by the red box is dominated by dislocation cores, and the two states marked by the black and blue boxes contain contribution from the entire boundary with the latter carrying a higher weight at dislocation cores. This finding is in excellent agreement with the STS results in Figure 4-4(c), which can be visualized by comparing the experimental band alignment in Figure 4-4(d) with that extrapolated theoretically in Figure 4-6. In the STS spectra displayed in Figure 4-5(c), the acceptor-like state marked by the blue arrows is also slightly modulated by dislocations. The three boundary states highlighted by the black, blue, and red boxes display drastically different real-space charge density distribution (Figure 4-5(b-d)) that correlates well to the spatial modulation of the corresponding STS peaks observed in Figure 4-4(c). Specifically, the boundary state enclosed by the red box is dominated by misfit dislocations, and the two states marked by the black and blue boxes contain contribution from the entire boundary with the latter carrying a higher weight at dislocation cores. Note: the bandgap is underestimated by PBE, which agrees with previous report (see section 2.3.4 for more discussion related to DFT).[204-206]

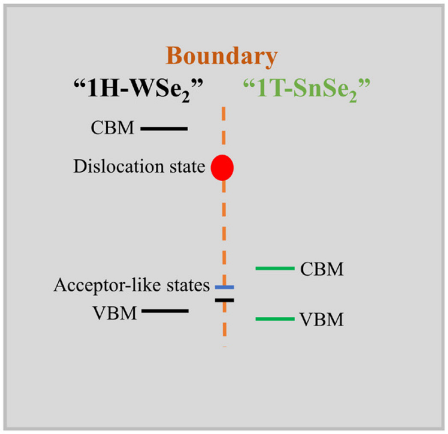

Figure 4-6: Theoretically extrapolated band alignment from PDOS analysis in Figure 4-5(e) The relative peak locations agree with Figure 4-4(d), where the acceptor-like states are near the VBMs and the dislocation state is above the CBM of 1T-$SnSe_2$ and below the CBM of 1H-WSe_2. The charge transfer with substrate which was not considered in the DFT calculation. Note that band bending near boundary is not mapped since PDOS was only analyzed in the center of TMD domains and along the boundary in Figure 4-5(e).

Formation of misfit dislocations is expected to relax the strain at 1H/1T boundary.[101, 102] Since electron doping has already been excluded as the cause of phase transition, to address how the transition occurs we inspect its outcome, i.e., the 1T′-WSe_2:1T-$SnSe_2$ (1T′/1T) boundary. In Figure 4-5(f), the optimized boundary structure calculated by DFT is overlaid on top of the STM image, which agrees with the simulated image (Figure 4-5(g)) as highlighted by features surrounding the dislocation core. It is worth noting that the periodicity of this boundary is identical to that of 1H/1T, owing to the same lattice parameter between the 1H and 1T′ phases of WSe_2

along the direction parallel to the boundary. Despite having the same periodicity, these two boundaries do exhibit some differences including the configuration of dislocation cores as marked by the arrows in Figure 4-5(c) and Figure 4-5(f), suggesting a relative gliding between the two domains during phase transition.

4.4 A New Phase Transition Mechanism in Core-shell Architecture

Next, we review the different stages during the core-shell formation and propose a new phase transition mechanism. The observed phase transformation in WSe_2 core is closely related to the degree of $SnSe_2$ coverage surrounding WSe_2 islands. As shown in Figure 4-1(b) and (f), no phase transition is observed in the initial stage when individual $SnSe_2$ domains developed from the adjacent 1H-WSe_2 edges are not yet merged, which is expected considering the relaxation of strain at the 1H/1T boundary by dislocations.[101, 102] With increasing coverage, $SnSe_2$ domains start to encounter each other and coalesce to form enclosed core-shell structures. During the dynamic process of merging (highlighted by light grey in Figure 4-1(g)), rearrangement of lattices necessarily occurs as the result of lattice misalignment between $SnSe_2$ domains. The degree of freedom in the (7:6) registry arising from prior nucleation of $SnSe_2$ along 1H-WSe_2 edges, signified by the position of misfit dislocation (Figure 4-7(a)), plays the major role in this lattice misalignment. Figure 4-7(b) illustrates the merging front (grey box) of type I and type II configurations, depicted in Figure 4-7(a), from the right and bottom edges, respectively. Without considering the further contribution from boundary separation, it translates into a ~13% lattice misalignment in the shell. With the various combinations of (7:6) configurations from the adjacent edges, the degree of lattice distortion in the shell could be even greater than that presented in Figure 4-7(b).

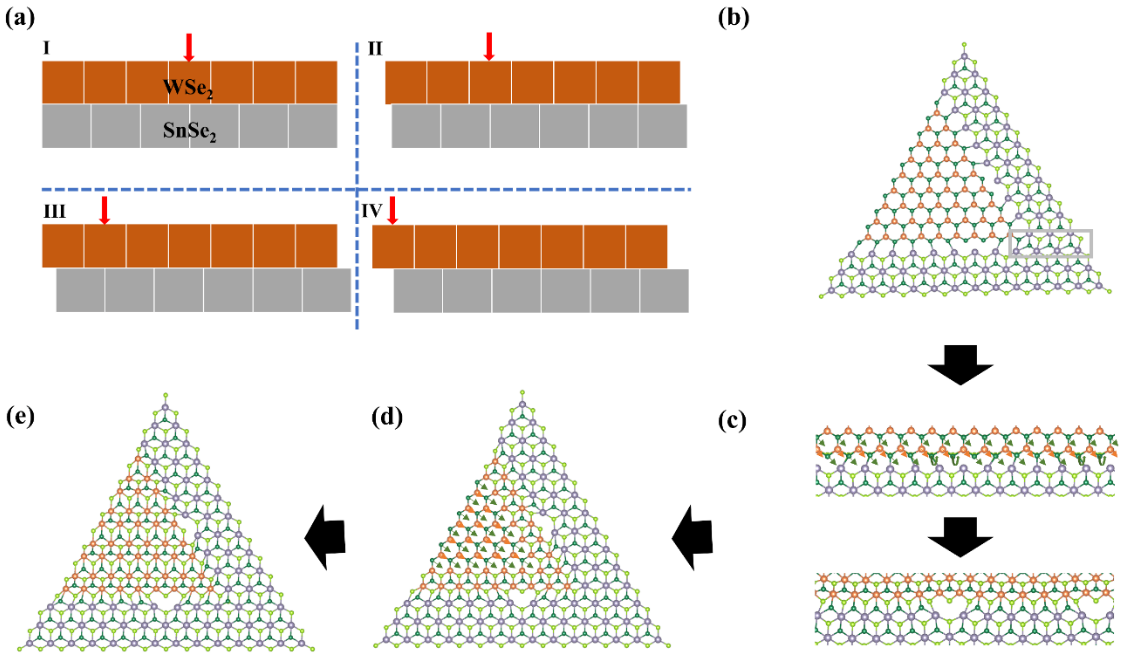

Figure 4-7: Mechanism of stress propagation for phase transformation of WSe$_2$
(a) Four different (7 WSe$_2$:6 SnSe$_2$) lattice alignment scenarios at 1H-WSe$_2$/1T-SnSe$_2$ boundary with the varying position of misfit dislocation (red arrow). (b) As SnSe$_2$ domains extended from adjacent WSe$_2$ edges merge, the random combination of (7 WSe$_2$:6 SnSe$_2$) pairs results in lattice misalignment at the merging front of the shell, highlighted in the grey box. The combination of type I and type II configurations from the right and bottom edges, respectively, is illustrated, which correlates to ~13% lattice misalignment (0.05nm/0.38nm) in the shell. (c) Rearrangement of SnSe$_2$ lattices during the coalescing induces a shear stress along the H-WSe$_2$/T-SnSe$_2$ boundary. The gliding motion of Se with respect to W, illustrated by the straight arrows, contributes to the polymorphic phase transformation of WSe$_2$. The curved arrows represent the possibility of Se atoms leaving the boundary. (d) Schematics to delineate the propagation of phase transformation from boundary to interior of WSe$_2$ until the entire WSe$_2$ island is transformed in (e). Note that for the purpose of illustrating stress propagation these schematics represent a simplified scenario where only two SnSe$_2$ domains from adjacent WSe$_2$ edges merge, whereas in actual experiments the complete WSe$_2$ phase transformation is often observed when WSe$_2$ islands are enclosed by SnSe$_2$ (Figure 4-1(d)-(e)).

As SnSe$_2$ rearrange to reach the energetically favored positions, a shear stress is inevitably created along the covalently bonded WSe$_2$/SnSe$_2$ junctions. We speculate this stress to cause a gliding motion of Se atoms relative to W ions (Figure 4-7(c)), which then propagates into the domain interior and leads to a H to T′ phase transition in WSe$_2$ (Figure 4-7(d-e)). The dimerization of metal atoms in Figure 4-7(e) is resulted from spontaneous structural relaxation of 1T phase due to Peierls-like distortion, which is a well-known phenomenon in group VI TMDs.[206] When WSe_2 islands are not yet fully enclosed by $SnSe_2$, a partial phase transition is induced (Figure 4-1(h)), consistent with the experimental observation in Figure 4-1(c). In the complete core-shell structure, the entire WSe_2 domain is transformed into the metastable T′-phase (Figure 4-7(i), and (d-e)). This shell-induced gliding motion may be further facilitated by the symmetry of $SnSe_2$ shell as Se atoms at the merging front, where the gliding is initiated, are already adopting the T phase. Note that the collective structural transformation of $SnSe_2$ domains is unlikely to occur since there is no reported metastable phase in the nearby energy range.

Integration of phase transition with core-shell architecture is unique and potentially versatile as: (i) TMD core is less likely to suffer from structural damage, such as fracturing, in comparison to other stress-based phase-transition methods.[192, 207-209] H to T′ phase transition of group VI TMDs (MoS_2, WS_2, $MoSe_2$, WSe_2) requires a biaxial strain of ~10-15%.[58] It is difficult to sustain such a big strain via conventional heteroepitaxy. Formation of misfit dislocations, as evidenced along each individual 1H/1T boundaries in this study, will largely relax the epitaxial strain[101, 102]. When the strain is applied using more aggressive methods like hydrostatic pressure with diamond anvil cell,[207] e-beam,[208, 210] or tip pulling,[209] potential development of fractures and vacancies will become a concern. (ii) It is less susceptible to contaminations[193, 211] or other undesirable substrate effects[170] as in the charge-transfer based techniques that involve foreign dopants. (iii) The methodology is likely applicable to other TMDs with the proper choice of core and shell materials. Covalent bonding between core and shell is necessary to enable the stress propagation from shell to core. Meanwhile, to create sufficiently large lattice misalignment as shells coalesce, it is mandatory to select shell candidates that bear decent lattice mismatch with the core. (iv) Establishment of phase transition on van der Waals interacting substrates not only reduces the constrain on the choice of substrate, but also opens possibilities to extend the technique to other vapor deposition methods, such as chemical vapor deposition which holds promise on scalability.[212]

4.5 Topological Properties of 1T′-WSe_2 Core

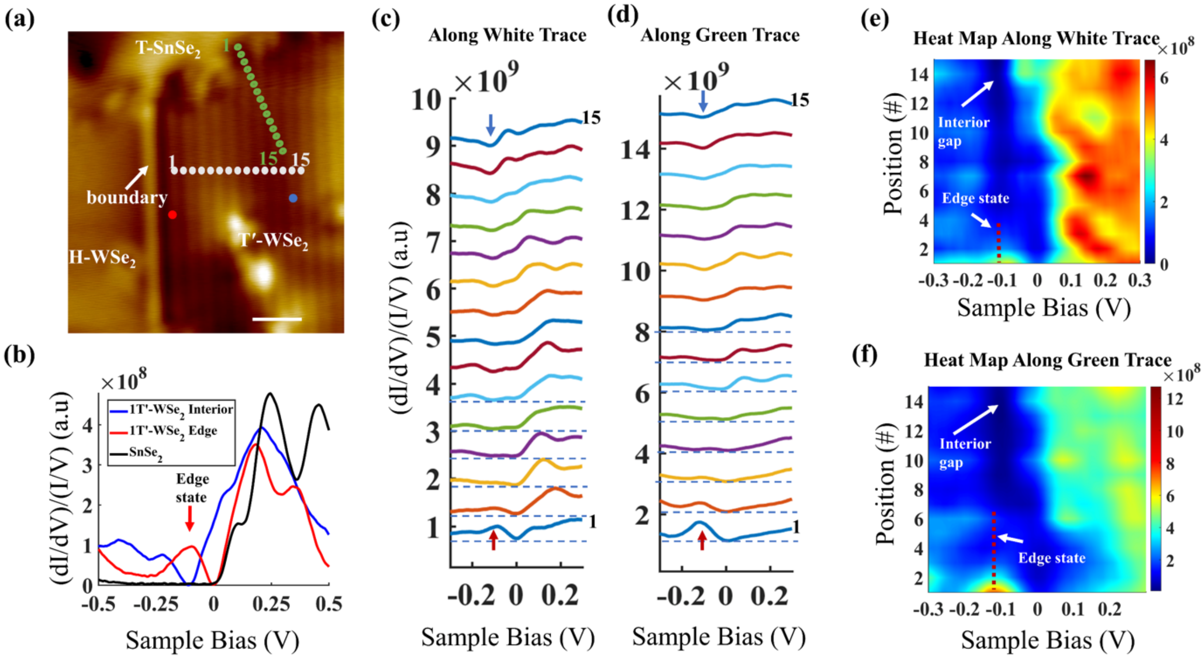

Figure 4-8: Topological edge state of 1T′-WSe_2
(a) STM image illustrating partially converted WSe_2 island (V_s = 2V, I_t = 30pA) on 1H-WSe_2/HOPG. The zoomed-out image of the same area is shown in Fig. 1(c). (b) Normalized dI/dV spectra (setpoint: V_s = 0.5V, I_t = 200pA) taken on the interior of 1T′-WSe_2 island (blue dot in (a)), the boundary (red dot in (a)), and $SnSe_2$, respectively. The blue curve reveals a dip at around -110mV which is associated with the bandgap of 1T′-WSe_2. Boundary (red) curve shows an edge state arising within the bandgap of 1T′-WSe_2 as well as the gap of $SnSe_2$ shell (black curve). (c-d) To examine the spatial extension of the edge state and to distinguish whether local structural perturbations influence this extension, dI/dV spectra are taken across both the smooth H- to T′-WSe_2 boundary (white trace in (a)) and the T′-WSe_2 to T-$SnSe_2$ boundary with periodic misfit dislocations (green trace in (a)). The red and blue arrows provide eye guide for the locations of the edge state and the interior bandgap, respectively. (e-f) DOS heat maps corresponding to (c) and (d), respectively. The extension of the edge state is drawn to the point where its DOS vanishes (red dashed lines), which corresponds to ~1.8nm for both boundaries. This demonstrates that the topological edge state is preserved in the core-shell architecture regardless of the boundary inhomogeneity and local perturbations associated with misfit dislocations. Scale bar: 2nm.

Most importantly, realization of phase transition on the template of HSs allows the rational design and integration of TMD functionalities. Proximity coupling could further lead to the emergence of new phenomena and enable the exploration of new physics that is otherwise not accessible.[18] In the WSe_2/$SnSe_2$ core-shell architecture, 1T′-WSe_2 is expected to be a 2D TI,[62, 63] which holds immense potential for applications of quantum spin hall (QSH) effect due to its much larger bandgap (~120meV) with respect to 1T′-WTe_2 and its better chemical stability in comparison to other large bandgap QSH insulators like stanene.[53, 206, 213] To explore the effects of local defects on the extension of topological edge state, we investigate both 1T′-WSe_2/1H-WSe_2 (smooth) and 1T′-WSe_2/1T-$SnSe_2$ (containing periodic misfit dislocations) boundaries on a partially phase-converted domain shown in Figure 4-1(c) and its zoom-in image in Figure 4-8(a). As depicted in Figure 4-8(b), a dip feature centered at ~ -110meV (blue curve) is observed on the interior of 1T′-WSe_2, whereas a conducting edge state (red curve) that is located right above the dip feature emerges near the boundary between 1T′-WSe_2 and a trivial semiconductor/insulator, i.e., 1H-WSe_2 or 1T-$SnSe_2$ in our study. The dip feature was suggested to be the consequence of gap reduction due to electron lifetime broadening associated with substrate coupling, vibrational, or electronic scattering.[62, 63] Spatial extension of the edge state was examined by taking STS spectra along the white and green dotted lines in Figure 4-8(a), corresponding to the smooth and “rough” boundaries, respectively. As revealed in the vertically offset spectra as well as DOS heatmaps (Figure 4-8(c)-(f)), this edge state penetrates ~ 1.8 nm into the interior of 1T′-WSe_2 at both boundaries, which provide strong evidence towards the preservation of extended edge state regardless of the boundary inhomogeneity and local perturbations. Additionally, investigations on various locations of the arc-like features on the 1T′-

WSe_2/1T-$SnSe_2$ boundary, arising from dislocation cores, also indicate the persistence of the edge state despite slightly modulated peak intensity (Figure 4-9).

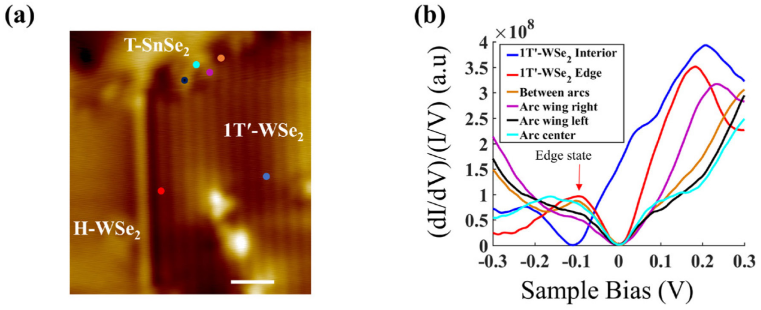

Figure 4-9: Topological edge state on the 1T′-WSe_2/1T-$SnSe_2$ boundary with structural perturbations from misfit dislocations
(a) STM image of the partially converted WSe_2 island (V_s = 2V, I_t = 30pA) on 1H-WSe_2/HOPG substrate. The zoomed-out image of the same area is shown in Fig. 1(c). (b) Normalized dI/dV (setpoint: V_s = 0.5V, I_t = 200pA) spectra taken on the interior of 1T′-WSe_2, the smooth edge between H- and T′-WSe_2, and on various locations of the T′-WSe_2/T-$SnSe_2$ boundary. Locations of the spectra are marked using dots of respective colors in (a). Regardless of boundary morphology and local structural perturbation, the edge state, as marked by the red arrow, persists with only slight modification of intensity. Scale bar: 2nm.

The robustness of the extended edge state concurs with its topological nature. Finally, the as-grown 1T′-WSe_2/1T-$SnSe_2$ lateral HS provides a valuable platform for investigating proximity-induced superconductivity[30] on the topological edge of 1T′-WSe_2 when the system is cooled below the superconducting transition temperature (T_c = ~4.84K) of $SnSe_2$.[147] Topological superconductivity is a functional ingredient for realizing Majorana bound states, which hold great potential to implement topological qubits in fault-tolerant quantum computation.[31]

4.6 Conclusion

In conclusion, we successfully demonstrate a H to T′ phase transition on vdWs interacting substrates based on the formation of WSe_2/$SnSe_2$ core-shell lateral HS. With comprehensive STM/STS and first-principles calculations, we propose a novel phase transition mechanism derived from shell to core stress propagation, which is presumably applicable to other TMDs and vapor deposition methods. In addition, we show that the topological edge state originating from 1T′-WSe_2 remains intact and is robust to periodic local perturbations at the core-shell boundary. WSe_2/$SnSe_2$ lateral HS with the directly exposed heterojunction provides a unique template for future investigations into proximity-induced superconductivity at the topological edge and the spatial extent of superconducting proximity effect.

5 Spatially Resolved Investigation of Mixed Valence and Insulator-to-Metal Transition in an Organic Salt

To demonstrate the universal importance of heterointerface and reveal the link between microscopic phenomena at the interface to global phase transition, we continue to investigate an organic lateral heterostructure (HS) in this Chapter. As mentioned previously, CTC exhibits a rich variety of physical properties.[10-13] With proper tuning such as hydrostatic pressure, electric field or optical fields, phase transition between different physical properties can also be triggered.[80, 83-85] Our collaboration with Dr. Shenqiang Ren, demonstrated a long-lived conducting phase up to 400 days after optical treatment of K-TCNQ, which future confirmed the bistablity of the Mott insulating and conducting phases.[80, 83, 84] As pointed out in the introduction, in the high conducting phase, K-TCNQ has periodic stripe-like patterns consisted of alternating carrier-rich and carrier-poor domains,[83] and coexisting of TCNQ molecules ($TCNQ^0$) and TCNQ radical anions ($TCNQ^{-1}$).[78, 83, 86] Does mixed valence and chemical composition variation give rise to any local inhomogeneity in the electronic structure of K-TCNQ? Furthermore, how does this local inhomogeneity relate to the phase separation that occurs on a much larger length scale? To address these questions, imaging and spectroscopy studies with molecular resolution are imperative.

In this Chapter, we use the self-assembly bottom-up approach to create heterojunctions of mixed valence consisted of TCNQ ($TCNQ^0$) and K-TCNQ ($TCNQ^{-1}$) domains on the weakly interacting HOPG substrate. STM/S is utilized to correlate the spatial distribution of electronic structures to the morphology of molecular heterojunction. Our results show that pristine TCNQ and K-TCNQ assemblies are both insulating, while a continuum of DOS across Fermi level (FL) arises in the TCNQ region near domain boundary due to abrupt change in the valence state of TCNQ molecules. As these DOS reach equilibrium with the rest of the system, they create local electric field, evidenced by the band bending in each molecular assembly. The abilities to construct exposed heterojunctions using bottom-up approach and to characterize them by STM/STS provide direct evidence that mixed valence indeed perturbs the electronic structure and local electrostatics in K-TCNQ, and that boundaries of mixed valence are likely the “weak” points to initiate the electric field induced IMT. The result is further discussed in conjunction with the previously reported macroscopic scale phase segregation in bulk K-TCNQ. This chapter is adapted from Reference[214]: *X. Dong et al., J. Phys. Chem. Lett. 2020, **11**, 8352−8357).*

5.1 Self-assembly and Electronic Structure of TCNQ on HOPG

Figure 5-1(a) shows the assembly of TCNQ molecules on HOPG substrate. A nearly square lattice with the head-to-tail molecular packing and unit vectors of $a_1 = 0.91 \pm 0.02$nm, $a_2 = 0.93 \pm 0.02$nm, and $\theta = 84 \pm 1^\circ$ is observed, in agreement with self-assembly of TCNQ on graphene.[215] Intra-molecular resolution of individual TCNQ molecules shows a characteristic four-arm pattern composed of two symmetric U-like protrusions and two bulges centered on the dicyanomethylene groups, separated by a central nodal plane, that resembles the lowest unoccupied molecule orbital (LUMO) of free-standing molecules.[216, 217] The observation of negative differential resistance (NDR, see section 2.2.5 for more discussion), i.e., the dip below zero in the STS spectrum (Figure 5-1(c)), that is characteristic for molecules weakly adsorbed on supporting substrates, further indicates that the electronic structures of TCNQ molecules are well preserved on HOPG.[137, 138, 218]

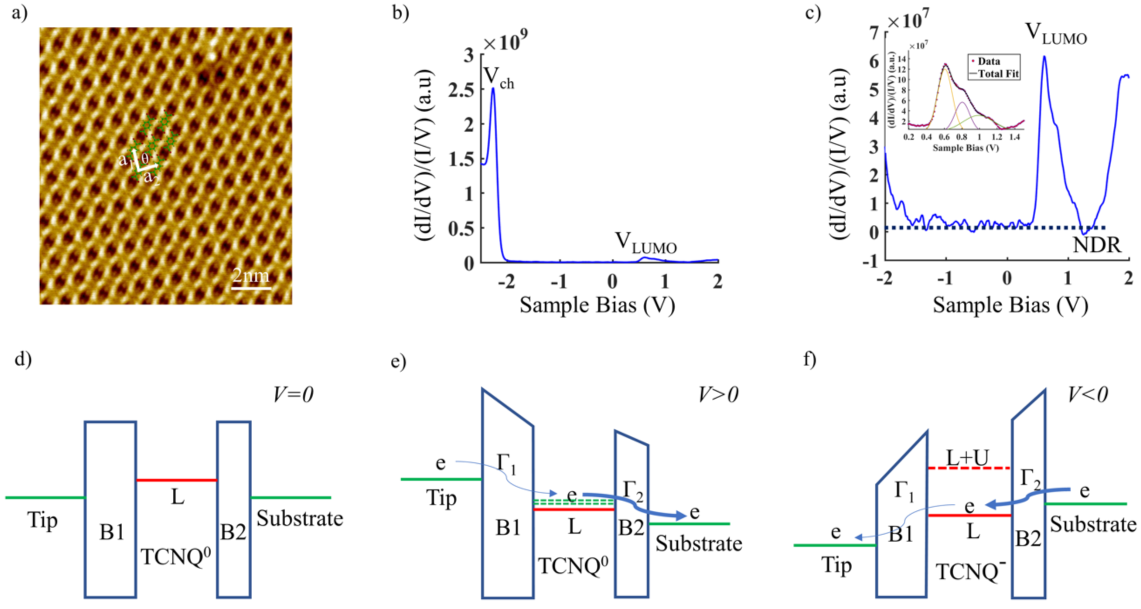

Figure 5-1: Morphology and electronic structures of TCNQ self-assembly on HOPG
(a) STM image ($V_s = 2V$, $I_t = 5pA$) of TCNQ self-assembly on HOPG with superimposed unit vectors as indicated by the white arrows and atomic structure of TCNQ molecule (C-green, H-yellow, N-red). (b) Representative normalized dI/dV spectrum (setpoint: $V_s = 2V$, $I_t = 30pA$) with a sharp charging peak at negative bias and a broad density of states (DOS) feature at positive bias. (c) Zoomed-in spectrum and Gaussian fitting shown in the inset illustrate that the broad DOS feature is composed of LUMO and its vibronic levels, followed by a negative differential resistance (NDR) region. (d-f) Schematics to explain the characteristic peak features observed in the normalized *dI/dV* spectra shown in (b-c): (d) Qualitative representation of the double barrier tunneling junction (DBTJ) model and the energy level alignment between tip, molecular layer and substrate at V (sample bias) = 0. The red solid line labeled "L" depicts the LUMO level of TCNQ, and the green solid lines for the FLs of the tip and substrate. B1 and B2 represent the effective tunneling barriers between tip and molecular layer at a finite tip-sample distance and between molecular layer and substrate, respectively. (e) Energy level alignment at positive sample bias ($V > 0$). Γ_1 and Γ_2 illustrate electron tunneling through B1 and B2, respectively, with the arrows indicating the tunneling directions and the thickness for the tunneling rate ($\Gamma_1 < \Gamma_2$). Green dashed lines mark the vibronic levels of TCNQ molecule. (f) Energy level alignment at negative sample bias ($V < 0$). U represents on-site Coulomb repulsion energy.

Nevertheless, the lack of strong chemical interaction does not preclude interfacial charge transfer. To discern the charge state of TCNQ molecules and to corroborate STS spectrum which exhibits a broad asymmetric peak at positive sample bias and a sharp resonance at negative bias (Figure 5-1(b-c), we look into the double barrier tunneling junction (DBTJ) model, as illustrated in Figure 5-1(d-f). Since TCNQ molecules are in direct contact with the substrate and are separated from the tip by a vacuum gap (~1nm), the effective barrier between tip and molecular layer (B1) is typically larger than that between molecular layer and HOPG substrate (B2). At positive sample bias (V > 0, Figure 5-1(e)), TCNQ molecules remain charge neutral as transient electrons ejected from the tip can be depleted to the substrate efficiently (electron tunneling rate $\Gamma_2 > \Gamma_1$). Further increasing the sample bias or electric field between tip and sample triggers the excitation of vibronic modes within TCNQ molecules and enables inelastic tunneling, which explains the broad asymmetric spectrum feature at positive sample bias (Figure 5-1(c)).[215, 219] Gaussian fitting of the broad asymmetric DOS (Figure 5-1(c) and inset) suggests a molecular peak associated with LUMO, accompanied by additional vibronic satellites with an average energy separation of 0.20 ± 0.04V. This energy separation can be attributed to the breathing mode of the inner carbon ring of TCNQ molecules, in agreement with the previously reported values associated with TCNQ vibronic modes.[215, 219] At negative sample bias (V < 0, Figure 5-1(f)), the electron tunneled from substrate to molecule cannot be effectively drained to the tip due to the small tunneling rate of Γ_1, altering the charge state of the molecule from $TCNQ^0$ to $TCNQ^-$. As sketched in Figure 5-1(f), to tunnel a second electron to this molecule the intramolecular Coulomb repulsion, U, on the order of several eV, has to be overcome, which essentially prevents the access of vibronic states and results in a single sharp resonant peak. Similar spectroscopic features have been observed previously in other molecular systems, attributed to the charging of molecular adsorbates.[215, 220-223] The observation of the charging peak further validates the charge neutrality of TCNQ molecules on HOPG substrate in the absence of external electric field (V=0, Figure 5-1(d)).

5.2 Self-assembly and Electronic Structure of K-TCNQ on HOPG

Upon deposition of potassium (K) atoms, the weakly bound TCNQ molecules readily rotate on the surface to form a two-dimensional mesh. Utilizing the characteristic four-arm pattern of TCNQ molecules, one can assign the positions of molecules and determine the dimensions of the unit cell ($b_1 = 1.35 \pm 0.05$nm, $b_2 = 1.41 \pm 0.05$nm and $\varphi = 94 \pm 1^{\circ}$), as illustrated in Figure 5-2(a). This "windmill" structure with K atoms occupying at the center surrounded by molecular neighbors of alternating orientation is in good agreement with the packing motif within the *b-c* plane of bulk K-TCNQ,[224] and its formation is likely a result of strong ionic attraction between K and TCNQ species. It is worth noting that the exact locations of K atoms are difficult to pinpoint. The protruding blobs observed in Figure 5-2(a) represent electron clouds delocalized among K atoms and cyano ligands of TCNQ molecules, and for simplicity K cations are assigned at the center of these blobs.[225-227] Major differences that distinguish the STS spectrum of K-TCNQ from that of TCNQ are: (1) the absence of charging peak at negative sample bias (Figure 5-2(b)); and (2) the shift of LUMO towards more positive energy by 0.25 ± 0.04V (Figure 5-2(c)). The charging peak necessarily vanishes since TCNQ molecules are already charged ($TCNQ^{-1}$) via the ionic interaction with K atoms, whereas the shift in LUMO can be explained by the increase in substrate work function. Increase in work function is a result of extra energy required to remove an electron from the FL to vacuum due to the formation of interface dipoles between the negatively charged TCNQ molecules and the induced positive image charges in the substrate.

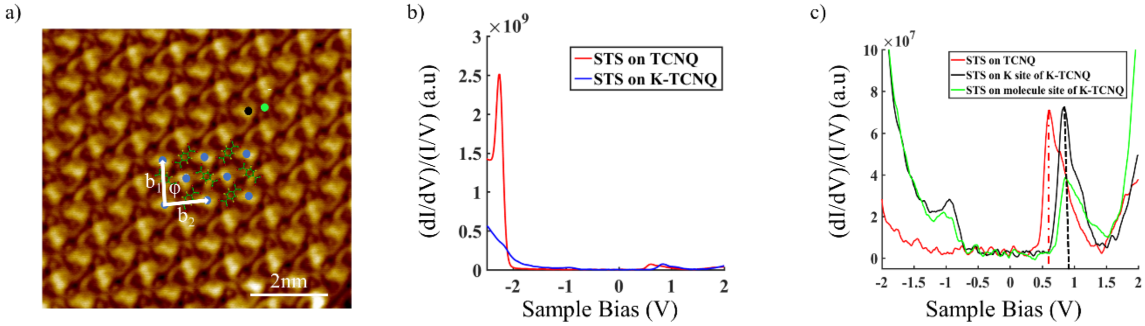

Figure 5-2: Morphology and electronic structures of K-TCNQ self-assembly on HOPG
(a) STM image (V_s = -2.0V, I_t = 5pA) of K-TCNQ self-assembly on HOPG with superimposed unit vectors as indicated by the white arrows. The atomic structure of TCNQ molecules (C-green, H-yellow, N-red) and the positions of nearby K atoms (blue dots) are denoted as well. (b) Comparison between the representative normalized dI/dV spectra (setpoint: V_s = 2.0V, I_t = 30pA) taken on the TCNQ (red) and K-TCNQ (blue) assemblies. The sharp charging peak at negative bias disappears on the K-TCNQ spectrum. (c) Zoomed-in spectra (setpoint: V_s = 2.0V, I_t = 30pA) on TCNQ assembly (red), at the center of a delocalized site on K-TCNQ (the black dot as marked on (a)), and at the molecular backbone on K-TCNQ (the green dot as marked on (a)).

5.3 TCNQ and K-TCNQ Lateral Heterostructure

TCNQ:K-TCNQ heterostructure can be readily created by sequential formation of K-TCNQ, i.e., via converting TCNQ assemblies to K-TCNQ using excessive K adsorption, followed by additional deposition of pure TCNQ. Due to variations in local molecular arrangement, defected boundaries associated with missing molecules, as marked by the white arrows in Figure 5-3(a), are frequently observed. However, for better benchmarking and systematic investigations of mixed valence effect, we focus on well-packed segments as that sketched by the black dashed line. Figure 5-3(b) illustrates the layout of TCNQ molecules and K atoms extrapolated from the bias dependent STM images in Figure 5-4.

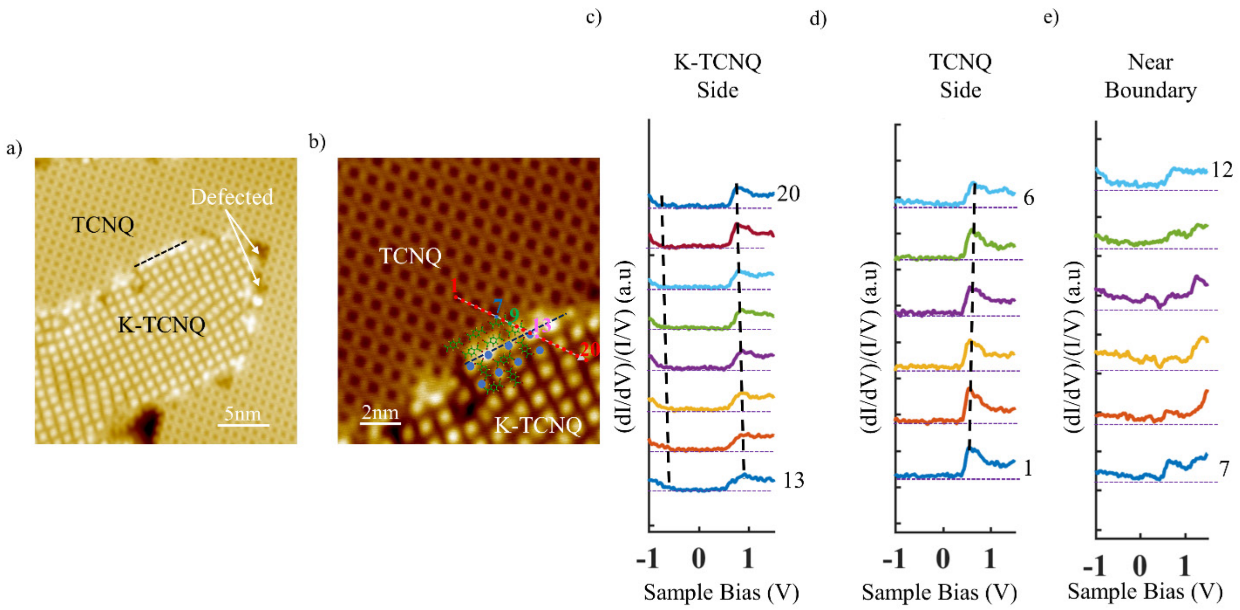

Figure 5-3: Morphology and electronic structures of TCNQ:K-TCNQ heterostructure on HOPG

(a) STM image ($V_s = 2.0$V, $I_t = 5$pA) of TCNQ:K-TCNQ heterostructure with the black dashed line and white arrows denoting a well-packed boundary and defected boundaries, respectively. (b) Zoomed-in STM image showing the well-packed region with superimposed TCNQ molecules and K atoms (blue dots) near the boundary. A line profile of dI/dV spectra was taken across the boundary along the red trace. (c) Normalized *dI/dV* spectra (setpoint: $V_s = 2.0$V, $I_t = 50$pA) collected on the K-TCNQ side of the heterostructure, corresponding to points 13-20 in (b). Spectra are offset vertically with the purple dashed line marking the zero DOS of each curve, and the black dashed lines outlining the shifts in the LUMO peak and the HOMO onset. As the boundary is approached from the interior of the assembly (point 20 to point 13), an upward band bending is observed, e.g., LUMO peak shifts away from the FL. (d) Normalized *dI/dV* spectra (setpoint: $V_s = 2.0$V, $I_t = 50$pA) collected on the TCNQ side of the heterostructure, corresponding to points 1-6 in (b). The same trend of LUMO shift and upward band bending is observed as the boundary is approached from the interior of TCNQ assembly (point 1 to point 6). (e) Normalized *dI/dV* spectra (setpoint: $V_s = 2.0$V, $I_t = 50$pA) collected near the TCNQ:K-TCNQ boundary, corresponding to points 7-12 in (b). A continuum of density of states rises within the apparent bandgap, particularly for points 7 to 11 that are near the boundary but still reside within the TCNQ assembly.

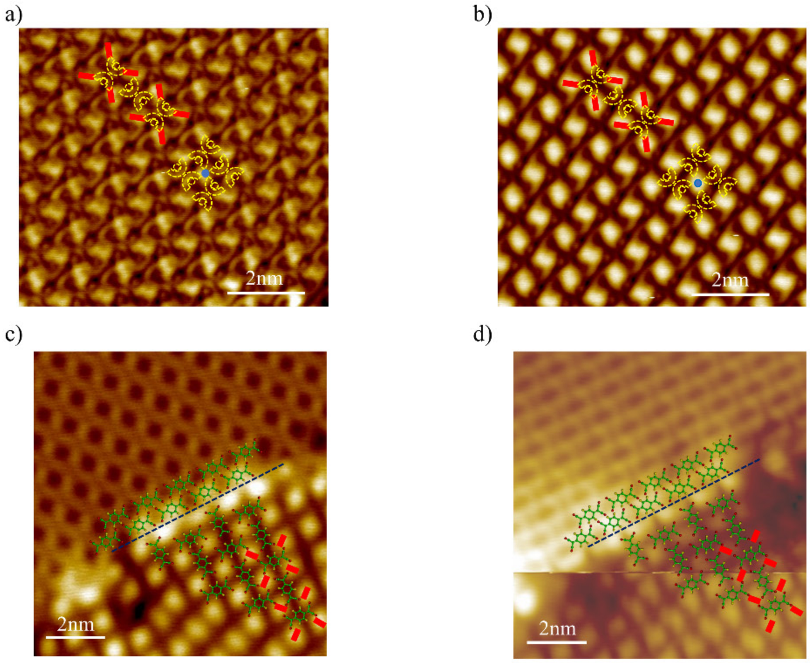

Figure 5-4: Assignment of molecule and K locations in K-TCNQ assembly and TCNQ : K-TCNQ heterostructure. Bias-dependent STM images of K-TCNQ
(a) V_s = -2.0V, I_t = 5pA. In the lower half of the overlaid schematics, four TCNQ molecules with the characteristic U-shaped features and bulges as outlined by the yellow dashed lines form a "windmill" structure with K atom in the center that is labelled by the blue dot. (b) V_s = 2.0V, I_t = 5pA. At positive bias, the characteristic intra-molecular shape is difficult to resolve. With the same "windmill" structure imposed and K atom located at the topmost of the protruding blob, we identify the registry of TCNQ molecules with respect to the fine distortion of the surrounding blobs as marked by the red bars (upper half of the overlaid schematics). This also serves as the guidance for the assignment of TCNQ molecules in the K-TCNQ domain of the heterostructure. Bias-dependent STM images of the TCNQ:K-TCNQ heterostructure: (c) V_s = 2.0V, I_t = 5pA, and d) V_s = 0.6V, I_t = 40pA. Tip-sample distance is reduced in (d) to reveal the characteristic U-shaped pattern on the TCNQ side. Molecular arrangement on the K-TCNQ side is expected to retain the same "windmill" structure as shown in the pristine K-TCNQ assembly.

Assignment of TCNQ molecules is based on the characteristic four-arm pattern composed of two symmetric U-like protrusions and two bulges centered on the dicyanomethylene groups, separated by a central nodal plane, that resembles the LUMO of free-standing molecules.[216, 217] This pattern is most clearly observed in Figure 5-1(a), revealing a head-to-tail packing of TCNQ molecules on HOPG substrate. In Figure 5-2(a), some part of the U-shaped arms is dressed by the presence of K atoms, while the bulges remain mostly visible. This provides basis for TCNQ assignment in the K-TCNQ assembly on HOPG substrate, in which neighboring TCNQ molecules are orthogonally aligned to each other with the center of the dicyanomethylene groups (corresponding to the locations of bulges) pointing at the middle of the quinonoid rings (corresponding to the locations of central nodal planes) of adjacent molecules. The exact positions of K atoms are difficult to pinpoint, and for simplicity K cations are assigned at the topmost of the protruding blobs (blue circles) observed in Figure 5-2(a) and Figure 5-4(a-b). This "windmill" structure that consists of K atoms surrounded by molecular neighbors of alternating orientation is in good agreement with the packing motif within the *b-c* plane of bulk K-TCNQ.[224] Figure 5-2(c) further illustrates that the intensity of the LUMO peak is stronger at the sites of K atoms as compared to the TCNQ backbones. This suggests that the TCNQ molecular orbital feature has been extended to K sites. Thus, the protruding blobs observed in Figure 5-4(a) and Figure 5-1(a-b) represent electron clouds delocalized among K atoms and cyano ligands of TCNQ molecules.[227] Additionally, the shoulder that emerges at ~-0.95±0.04V on the normalized dI/dV spectrum (Figure 5-2(c)) likely originates from the HOMO of K cations, which, to certain degree, also convolutes with the cyano ligands of neighboring TCNQ molecules.

Boundary in the TCNQ : K-TCNQ lateral heterostructure (Figure 5-3(a-b)) is reasonably well defined as the two domains exhibit dramatically different molecular alignment and electronic structures. The electronic effect on morphology is most pronounced in Figure 5-4(d) as a relatively sharp transition is observed from the TCNQ to K-TCNQ domains. While the U-like pattern is clearly observed within the TCNQ domain to assist the molecular assignment, it is not resolved on the K-TCNQ side (Figure 5-4(c-d)) due to the predominant delocalized electronic clouds around K atoms. Therefore, we deduce molecular alignment on the K-TCNQ side of the heterostructure under the guidance of bias-dependent STM images taken on the pristine K-TCNQ assembly (Figure 5-4(a-b)).

To assess the spatial distribution of electronic structures across the boundary, STS line profile is performed at 20 evenly spaced locations along the red trace in Fig. 3b. The spectra taken on the K-TCNQ side (points 13 to 20) are displayed in Figure 5-3(c), with each individual one showing the characteristic DOS as discussed in Figure 5-2(b-c). Remarkably, an upward band bending behavior becomes pronounced as we trace the positions of LUMO peak and HOMO onset from the interior of K-TCNQ assembly towards the TCNQ:K-TCNQ boundary. Beyond the shift in LUMO, its peak also becomes broadened as approaching the boundary, as evidenced by the Gaussian fittings in Table 5-1.

Gaussian analysis of peak position and peak width

	Point Number	LUMO Peak (V)	FWHM (V)
	1	0.53	0.33
	2	0.54	0.35
TCNQ	3	0.56	0.47
	4	0.56	0.45
	5	0.60	0.50
	6	0.64	0.66
	7	0.66	0.53
	8	0.62	0.61
	9	0.71	0.95
	10	0.74	1.00
Near Grain Boundary	11	0.74	0.89
	12	0.74	0.76
	13	0.93	1.26
	14	0.92	1.19
	15	0.89	1.01
	16	0.86	0.75
	17	0.84	0.48
	18	0.79	0.49
K-TCNQ	19	0.77	0.40
	20	0.77	0.42

Table 5-1: Summary of position and FWHM (full width half maximum) of LUMO peak obtained from Gaussian fitting of the twenty normalized *dI/dV* spectra shown in Figure 5-3. As approaching the grain boundary from either the TCNQ (points 1-6) or K-TCNQ (points 20-13) side, the LUMO peak shifts away from the FL accompanied by peak broadening. As the continuum density of states arises within the apparent bandgap (points 7-12), it becomes more difficult to isolate the LUMO peak, thus the peak position and FWHM obtained from Gaussian fitting may not be accurate.

Figure 5-3(d-e) displays the STS spectra on the TCNQ side (points 1 to 12), which can be categorized into two groups of distinct behaviors. The curves taken on points 1-6, relatively far from the boundary, exhibit the characteristic TCNQ electronic structure despite the upshift and the broadening of the LUMO peak as moving towards the boundary (Table 5-1), a behavior similar to that seen on the K-TCNQ side. Nevertheless, a striking phenomenon arises in those spectra collected near the domain boundary (points 7-12), in which a continuous DOS across the FL is established. Considering that molecules within this region, ~1.5nm from the physical domain boundary, are as well packed as those in the deep interior of the TCNQ assembly, these continuum states that emerge inside the molecular bandgap cannot be attributed to localized defects states associated with disorders in the TCNQ structure. As discussed in our recent work, adding a K^+ vacancy in the bulk K-TCNQ unit cell introduces DOS within the bulk gap.[228] Thus, the continuum DOS observed in our experiment most likely originates from the abrupt valence change at the boundary, the electrostatic effects of which spreads a couple of nanometers into the interior of TCNQ assembly. Local electric fields are created as these states reach equilibrium with the rest of the system including HOPG substrate via charge transfer. The strength of the electric fields can be estimated from the degree and width of the band bending, which amounts to the order of 10^7-10^8 V/m in both assemblies.

5.4 Discussion

Previous studies on bulk K-TCNQ and related alkali-TCNQ systems have witnessed IMT induced by electric field, optical field, or pressure.[78, 83, 86, 228, 229] The mechanisms of the induced IMT had been largely attributed to the avalanche dielectric breakdown.[77, 83] From the energetics perspective, the application of electric field decreases the energy barrier between the insulating Mott state and the metastable correlated metallic (CM) state. Once the density of CM state reaches the critical value, an avalanche-like process could be triggered, resulting in the formation of percolated conducting pathways/filaments.[77] Our results indicate that boundaries of mixed valence are likely the “weak” points to initiate dielectric breakdown. While more electrons are redistributed to the newly available DOS, causing even greater local electric fields, the “positive” feedback is accountable for the avalanche-like behaviors. Nonetheless, current-induced phase segregation in bulk K-TCNQ has been reported to occur with a very periodic manner on the macroscopic scale, whereas mixed valence, typically a consequence of electrochemical migration of metal ions in metal-TCNQ systems, represents a local phenomenon.[83, 89, 229-233] Next, we discuss a possible scenario to associate these phenomena developed at the different length scales.

In macroscopic transport studies carried out in bulk K-TCNQ, the electrochemical migration of K^+ is expected to generate a gradient of mixed valence between the two electrodes. Microscopically, as K^+ ions migrate away from the positive terminal, leaving behind nano-puddles of K-TCNQ and TCNQ, local electric field will be built up in line with the STM/STS observation discussed above. IMT naturally starts from locations of the greatest local electric field and propagates towards the other electrode. Stripe-like alternating metallic and insulating domains are developed along this propagation direction, likely due to the Coulomb interaction between adjacent metallic domains which determines the overall periodicity of the pattern. Note that a similar phase coexistence with stripe-like micrometer-sized domains induced by nonuniform strain had been recently reported in a (BEDT-TTF)-based CTC compound.[234]

5.5 Conclusion

To summarize, our STM/STS investigation provides the first microscopic understanding of the crucial physics occurring near domain boundaries of mixed valence in K-TCNQ. Additionally, our study demonstrates that the ability to construct organic heterojunctions using bottom-up approach is vital for identifying the key physical processes empowered by interface. This methodology is anticipated to lead to broader impacts in other organic or inorganic charge-transferred systems since the bottom-up approach enables these interfaces that are typically buried in the bulk to be directly exposed for a microscopic understanding of structure-property relationship.

6 Investigation of $SnSe_2$ on $SrTiO_3$ (STO) Surface

From Chapter 3 and Chapter 4, we developed a good understanding of interface interactions and their effects on modifying and even inducing new electronic properties of thin films in a Heterostructure (HS). More recently, superconductivity (SC) was also induced in the originally semiconducting $SnSe_2$, a van der Waal metal dichalcogenides, via pressure,[235] gating,[236] heterostructures,[147, 195] or intercalations.[237] Most intriguingly, recent investigations of $SnSe_2$ on graphene[147] and STO(001)[195, 238] both revealed the striking two-dimensional nature of the SC in the HSs. Charge density wave (CDW) and SC were found to coexist in the same $SnSe_2$ film[195, 238] which shares some similarity with high T_c superconductors where the electronic phase diagram often displays CDW phase in adjacent to SC phase. This provides a good platform for the study of correlated behavior near 2D limit. In Chapter 4, we have successfully created a ($SnSe_2$/1T′-WSe_2) core-shell HS connecting the 2D superconductivity to a 2D topological insulator.[171] Via proximity effect, this lateral heterostructure was predicted to be a promising route to achieve topological superconductivity,[18, 30] which is a key ingredient for the realization of Majorana physics for fault tolerant quantum computing.[31]

As pointed out in Chapter 4, the superconducting transition temperature (T_c) in the $SnSe_2$/graphene HS is ~4.8K. Previous studies also showed that superconducting transition in the $SnSe_2$ HSs ties strongly to the amount of charge carriers near FL which is typically donated by the other constituent.[147, 195, 236-239] Consequently, electronic donating ability of the other constituent (usually the substrate) has become very important. So far, the highest superconducting transition temperature (T_c =~8.3K) is achieved on STO(001) surface, which is a an excellent electron donor hosting a two dimensional electron gas (2DEG) near the surface.[195, 240] Is there a possibility to increase the T_c even more with more doping from the substrate? Can the substrate be modified to achieve this goal, and can new properties be induced from the HS construction on this surface?

With these two questions in mind, in this chapter, we will focus on the investigation of $SnSe_2$ thin film on differently modified STO surfaces to understand the effect of the interface interaction in contribution to the development of the exotic effect such as CDW and SC. This chapter consists of two parts. For the first part, we will focus on the studying the effects of local variations on the reconstructed STO(111) surface on the growth and the electronic properties of the $SnSe_2$ overlayer. For the second part, the STO surface will be modified by the deposition of a monolayer WSe_2 which effectively constructed a vertical HS and we investigate its influence on the electronic structure of the $SnSe_2$ overlayer. (*This work is yet to be published*).

6.1 Spatially Inhomogeneous Charge Transfer in $SnSe_2$/3 × 3 Reconstructed STO(111)

In this part, we systematically investigate the local electronic structure variations in the $SnSe_2$/STO(111) system on a microscopic scale by STM/S. Three low-index STO surfaces are commonly available: STO(001), STO(110) and STO(111). In the ideal crystal structures, STO(001) (STO(110) and STO(111)) crystal consists of alternating layers of square (rectangular, hexagonal) SrO ($SrTiO^{4+}$, Ti^{4+}) and TiO_2(O_2^{4-},SrO_3^{4-}) with step height of 0.391nm (0.275nm and 0.225nm), corresponding to distance between the adjacent layers with same chemical compositions (Figure 6-1).[241] The STO(001) are most widely explored due to its charge neutral nature. It is relatively easy to obtain the atomically smooth and homogeneous TiO_2 terminated surface on the STO(001) surface from chemical and thermal treatment.[242, 243]

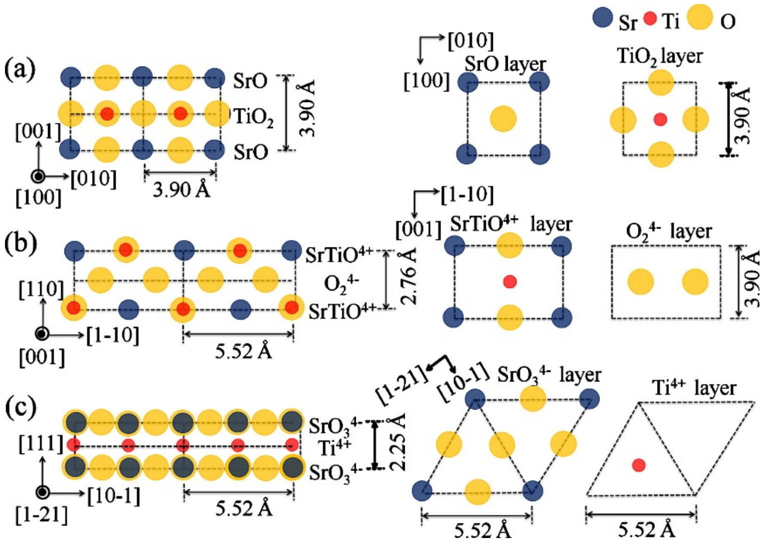

Figure 6-1: Crystal structure of STO(001), STO(110) and STO(111). Adapted from [241]

Meanwhile, the polar instability on the truncated bulk STO(110) and STO(111) surface are often required to be compensated by electronic and/or structural reconstructions (RCs).[244-251] To compensate this instability, both top and bottom surfaces will need to be modified to obtain a charge density that cancels with one half of the next bulk layer as revealed in Figure 6-2(a). This charge density modification on the surface can be done with and without the changing of the surface stoichiometry. Without changing the surface stoichiometry, the surface charge density modification can be solved by electronic RC with the out-of-plane ionic displacements which is typically observed in STO surface layers that is subjected to an electron confining potential.[249, 252] This modification can also be driven by a surface RC that changes the surface stoichiometry which is often observed in high-temperature treated STO samples.[244-251] The surface RCs of the STO(110) and STO(111) are typically modeled with bilayer TiO_x terminations with different Ti and O arrangements.[246, 248, 250] This is true for both the 3 × 3 and 4× 4 surface RC of STO(111) that is used in this thesis.[247] Nonetheless, the charge density of the surface of these RCs will satisfy the same condition as described earlier. Using 4 × 4 reconstructed surface of STO(111) as an example (Figure 6-2(b-c)), the surface consists of two TiO_x layer where the stoichiometry and the charge of top layer L1 and second layer L2 are $(Ti_{18/16}O_{52/16})^{2-}$ and $(Ti_{20/16}O_{8/16})^{4+}$, respectively. [247, 253] Together, the surface charge will be 2+ which cancels with one half of the next bulk layer SrO_3^{4-} which agrees with polar compensation condition.

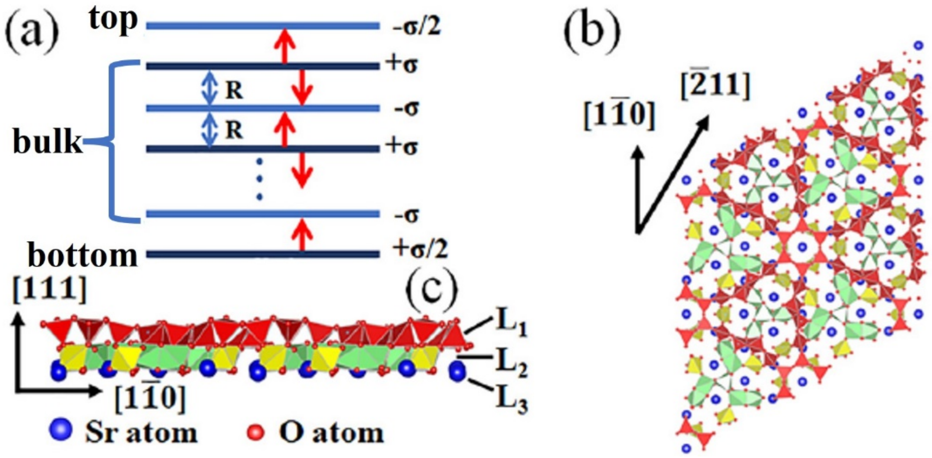

Figure 6-2: Polar compensation mechanism by surface reconstruction and 4 × 4 surface reconstruction of STO(111). Adapted from [253]
(a) Polar compensation mechanism with surface charge density modification of top and bottom surface. (b-c) top and side views of 4 × 4 surface RC of STO(111) from [247].

The oxygen vacancies created by thermal annealing will donate electrons that are partially localized near positively charged vacancies and partially itinerant to form 2DEG near the surface.[240, 254] The weight of the 2DEG wavefunction is neglectable on the topmost surface, and the 2DEG exists with different surface RCs.[240, 254] Both the carrier concentration in the 2DEG and the work function of the STO substrate depend critically on the environment, surface termination, as well as the sample processing condition.[255-257] Slight variation on the sample treatment could cause a very different surface defect density or surface reconstruction along with a significant work function variation (up to a few tens of meV).[257] The detailed characterization of the STO surface before the deposition of $SnSe_2$ film was largely omitted in the previous studies,[147, 195, 238, 239] which requires more careful investigations. Substrate variation could be an important factor that contributes to the variation in T_c and the coexistence of CDW and SC phases found in the previous studies.[147, 195, 238, 239] Lastly, the $SnSe_2$ band structure could also be modified by local variations in the growth morphology, such as strain and local defects. A systematic investigation on the local variations of the $SnSe_2$/STO system is imperative for understanding the interfacial phenomena and the emergent novel physical properties.

In our experiment, a reasonably well-defined 3 × 3 reconstructed STO(111) surface is created and a 2DEG is shown to form near the surface. Electronic variations on the surface are revealed from the location dependent STS measurements. We then investigate the growth of $SnSe_2$ on this symmetry-matching(hexagonal)reconstructed STO(111) surface. $SnSe_2$ forms a high-quality (carpet-like growth with low density of defects) film, where the electronic and structural variations in the film can be correlated to the local strain and local charge transfer in the system. By linking the electronic evolution to the gradual changes in the film substrate separation, a critical role of the interface is revealed. The local nonuniformities will likely lead to granular SC before it eventually evolves into continuous SC at low enough temperatures, which is important in understanding the transport behavior in the system.

6.1.1 STO(111) Surface Reconstuction and Local Electronic Variation

As shown on section 2.1.2, substrate surface plays an indispensable role for the growth of high-quality thin film[258-260] which is also responsible for tuning its electronic properties[15, 261, 262]. Prior to film deposition, detail characterization of STO substrate is required. In this experiment, niobium (Nb)-doped (0.5% by weight) STO(111) substrate was annealed up to ~1150 C for 1 hour in UHV (<1E-9 mbar). On each terrace, surface is primarily consisted of atomically smooth 3 × 3 RC and some local defects (Figure 6-3(a)). The height measurement (Figure 6-3(b)) across the STO(111) step is found to be ~0.23 nm which agrees with previous result.[241] The unit cell of the 3 × 3 RC were marked by white rhombic in the zoomed STM image (Figure 6-3c), confirmed by the lattice constant measurement (Figure 6-3c).[241, 246, 247]

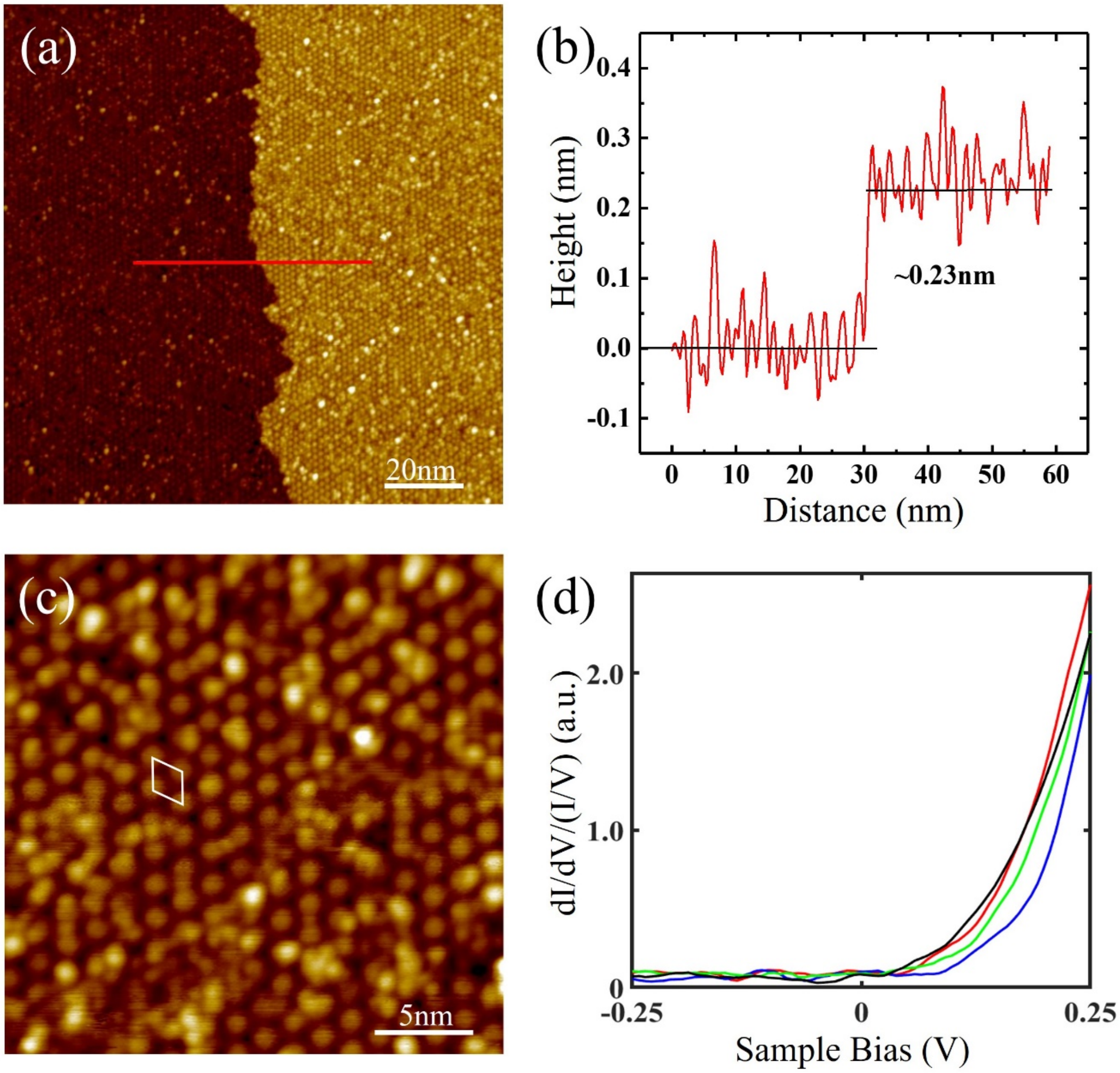

Figure 6-3: Substrate morphology and work function variations on this substrate
(a) Large scale STM image ($V_s = 2V$, $I_t = 5pA$) revealing majority of the STO(111) surface forms 3 × 3 surface reconstruction. Terraces at different steps reveals similar structures. (b) Line profile across red line in (a) revealing the single step height of the STO(111) surface. (c) zoom-in STM image ($V_s = 2V$, $I_t = 5pA$) with the unit cell of 3 × 3 surface reconstruction labelled by white rhombic (d) Representative STS spectra ($V_s = 0.5V$, $I_t = 200pA$) taken at various locations of the substrate shows location dependent for the energy position of the CBM.

The metallic behavior of 2DEG is confirmed by transport measurement of both doped and undoped samples with same treatment as shown on Figure 6-4. However, neither signature of the 2DEG nor the in-gap states created by the oxygen vacancies and previous observed local defects are observed. Only a large gap is found on STS spectrum as shown in Figure 2-10(a). Figure 2-10(a) shows a characteristic STS curve on the 3 × 3 RC, which reveals a very large clean bandgap of ~3.09V, deduced from the log-scale plot (Figure 2-10(b)). The bandgap is slightly smaller in comparison to previous report (~3.20V),[263] which is likely associated with surface states of the 3 × 3 RC. Previous ARPES studies indicate the formations of the 2DEG sub-bands below Fermi level (FL) which is buried deep (~a few layers) beneath the reconstructed surface.[240] Thus, it is very difficult for the surface sensitive technique like STS to detect. To correctly explain "disappearing" of in-gap states, we need to understand some profound challenges in the tunneling based imaging techniques.[264] It can be linked to two reasons. At first, wavefunction distribution of defect states might be confined in-plane. Previous study[264] has pointed out that the wavefunction of oxygen vacancy state is mainly confined in-plane in the TiO_2-terminated STO(001) surface. The 3 × 3 RC is modeled by the surface termination of bilayer TiO_x, which is likely has similar wavefunction distributions for the vacancy state.[247] Lacking the out of plane component reduced the possibility of overlapping with the tip DOS which makes the observation of these states difficult. Secondly, the density of the defect states may be low, and the energy level of the defect states are far from the bulk states. As the defect induced in-gap states are localized, at low density, the wavefunction of different defect sites cannot overlap to form a lateral conducting pathway for tunneling. On the other hand, if the defect states are in the energy level near the bulk states, a conducting pathway can also be established from resonance tunneling (e.g. if the defect state is near the CBM, electron can tunnel from the tip to the in-gap states, then tunnel into bulk CBM to form a completed pathway). For the defect states to be not observable in a tunneling measurement, both conditions must be met.

Meanwhile, the combined effects of Nb and oxygen vacancy doping likely contribute to the pulling of CBM of STO(111) toward FL. As shown on Figure 6-3(d) and Table 6-1, the energy position of CBM shifts slightly which reflects local variations of doping level and work function. These local morphology and electronic variations are expected to influence both the growth and the electronic properties of the deposited thin film, which is worth examining.

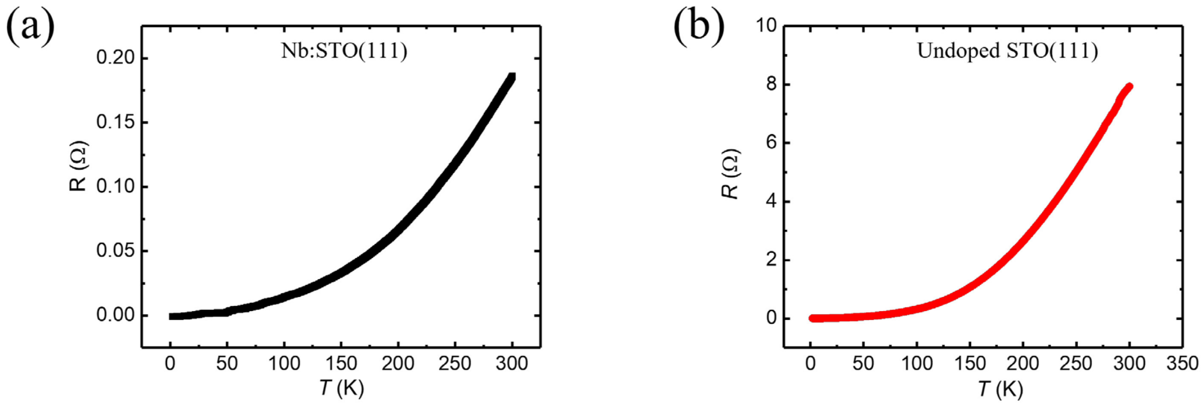

Figure 6-4: Temperature dependent four-probe resistance measurement for UHV treated STO(111) samples
(a) UHV annealed Nb:STO(111) 3 × 3 RC surface. (b) UHV annealed undoped STO(111) surface. Same UHV treatment procedure was used. The four-probe resistance measurement was done in physical property measurement system (PPMS) by Quantum Design. 20uA current was used in both measurements. The metallic behavior can be removed by sanding away the conducting surface layers.

	Red Curve	Blue Curve	Green Curve	Black Curve
CBM position (V)	0.013	0.051	0.031	-0.038

Table 6-1: CBM variations of the STO(111) surface
The energy position of CBM was extracted from the method used in Figure 2-10 and Figure 6-3. From this table, a maximum shift of a ~0.09V on the CBM was found, which is likely connected to the work function variation of the STO surface.

6.1.2 Growth Morphology of $SnSe_2$ on 3 × 3 RC STO(111)

Upon deposition of $SnSe_2$ onto the 3 × 3 RC STO(111) surface, the growth mode was found to be coverage dependent as shown in Figure 6-5. This suggests significant changes on the interaction scheme with substrate. In the direct contact regime, the incoming atoms forms small clusters (nanoparticles) on surface without destroying the 3 × 3 RC surface (Figure 6-5(a)). This is believed to be related to the limited diffusion which is attributed to the relatively stronger interaction with substrate and the limited growth temperature for $SnSe_2$. Unlike other transition metal dichalcogenides (e.g. WSe_2, $MoSe_2$), $SnSe_2$ decomposes at temperature above 513K which limits the growth temperature. Further deposition in the direct contact regime leads to the coverage of STO surface with more nanoparticles without formation of compact islands (Figure 6-5(b)). As no compact islands are formed, this layer will be referred as "dead layer". The height of the dead layer nanoparticles (insets, Figure 6-5(b)) is significantly shorter than the calculated monolayer thickness of $SnSe_2$.[205] This is likely due to stronger interaction with the STO substrate that reduced the interlayer spacing and perturbed stoichiometry. Local height variations (Figure 6-5(a-b)) are also observed within the dead layer, which could suggest influence from the local morphology and electronic structure variations of the substrate. Continue to increase the coverage above the dead layer, compact $SnSe_2$ layer was achieved which grows over the STO steps like a carpet (Figure 6-6(a-b)) with small number of defects (e.g. vacancies and grain boundaries). Figure 6-6(c) shows more detail of the continuous $SnSe_2$ film across a step, with the unit cell of $SnSe_2$ marked by blue rhombic. We believe that interaction weakened by covering the STO surface with nanoparticles in the dead layer enables the growth of the compact $SnSe_2$ films above. Large continuous films are formed due to the coarsening of adjacent smaller islands. This is drastically different from $SnSe_2$ deposition on weakly interacting graphene[147] or WSe_2[171] where compact islands are found in the direct contact regime.

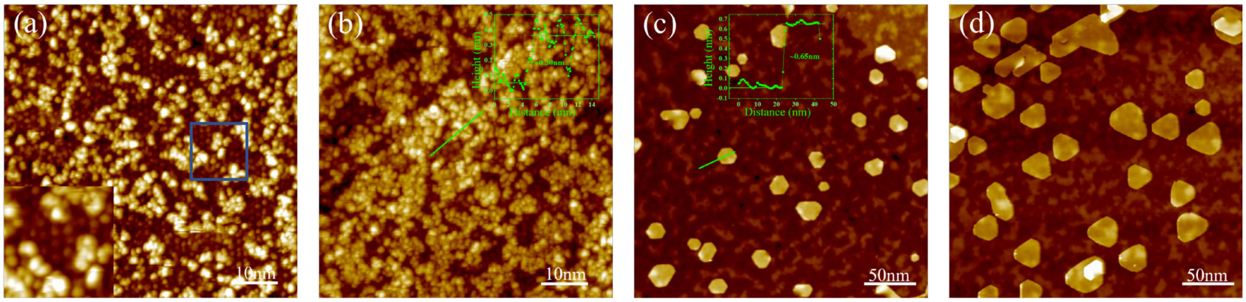

Figure 6-5: Sub-monolayer growth morphology and layer dependent growth rate
(a) STM image ($V_s = 2.5V$, $I_t = 5pA$) showing growth morphology at sub-monolayer are granular with the 3 × 3 RC STO(111) still partially visible beneath. The inset shows the 2x magnified inside the blue box. Sn and Se were co-deposited with Sn flux (~35nA), deposition time 30mins. The estimated coverage is ~30%. Additional 30mins at the same condition as in (a) increases coverage to ~60% (b). After formation of $SnSe_2$ film, the growth rate is significantly reduced due to weakened interaction to substrate as shown on (c-d) Sn flux (~150nA), deposition time has increased for 30mins, the coverage only increased for ~10%. Insets in (b-c) measure the height profile across the green lines in the respective images.

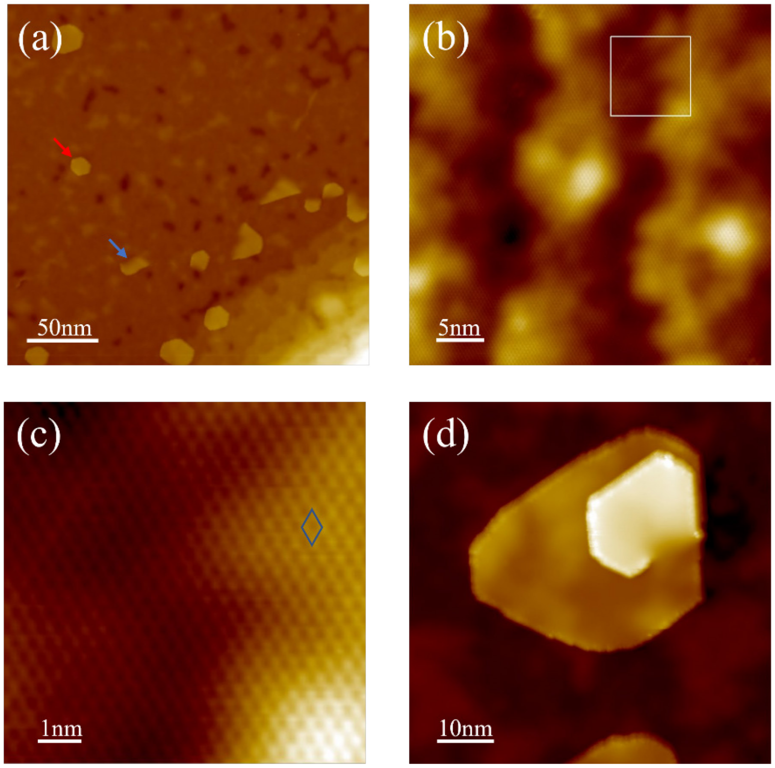

Figure 6-6: Characterization of growth morphology of $SnSe_2$ on STO(111)
(a) Large-scale STM image ($V_s = 2V$, $I_t = 5$ pA), showing a large continuous growth on the first layer and small amount of growth on the second layer with either isolated island or partially

Figure 6-6 (cont'd)
connected island to the first layer. (b) STM image (V_s = 0.6V, I_t = 150pA) showing carpet-like growth with lattice continuity across STO steps and low density of atomic defects. (c) Zoom-in STM image (V_s = 0.6V, I_t = 150pA) inside white box of (b) clearly reveals the lattice continuity across the step, with $SnSe_2$ unit cell labelled by blue rhombic. (d) STM image (V_s = 2V, I_t = 30pA) showing spiral growth originated from the partially connected $SnSe_2$ island.

It is worth mentioning that coarsening of the smaller island are capable of climbing over most of the height variations from the substrate (e.g. step, Figure 6-6(a-b)) and the height difference from the nanoparticles (Figure 6-5) which revealed as dark and bright patches (Figure 6-6(a)) on the continuous first compact $SnSe_2$ layer. Above the fully covered first compact $SnSe_2$ layer, there are few second-layer islands found in two types: isolated second layer and film with partial connection to first layer (Figure 6-6(a)). The later will be referred as "partially connected second layer" from now on. Continue to deposit $SnSe_2$ after the coalescence of the first monolayer, the growth rate is significantly reduced with smaller sticking coefficient from weakened substrate interaction. Consequently, the diffusion length is significantly increased. We no longer observed high-density small clusters, instead an increase in both the size and the density of compact $SnSe_2$ islands was found. The growth mode and the film quality of these isolated island are similar to the growth on HOPG, due to similar weak vdWs interactions. The isolated islands growth bigger and evolves more towards the truncated triangles due to the different growth rate on the opposite sides. Although, 1T structure can have six-fold symmetry with all edges terminated with the most stable edge. The edge flips up and down on the opposite sides causing a different interaction with the substrate which result in different growth speed, thus grow toward triangular shape.[265] Meanwhile, some of those partially connected second layer serves as seeds to drive the growth into a spiral form.[258, 265] The partially connected second layer can be view as the screw dislocation which is likely originated from the unevenness of the substrate/dead layer (such as a step or a small bump or dip in a dead layer). Once the screw dislocation is created, a growth front can be formed that continues to spiral up due to the previous mentioned growth speed different.

6.1.3 Distance Dependent Evolution of $SnSe_2$ Electronic Structure

In this experiment, we were provided a unique opportunity to observe the change in charge transfer behavior across a gradual climbing $SnSe_2$ island at the initial stage of a spiral formation. From the investigation of the electronic structure evolution in this partially connected second layer (Figure 6-7(a-b)), more insights can be learned towards the interfacial phenomena. The spatial electronic evolution of the partially connected second layer were inspected by the spatial dependent STS.

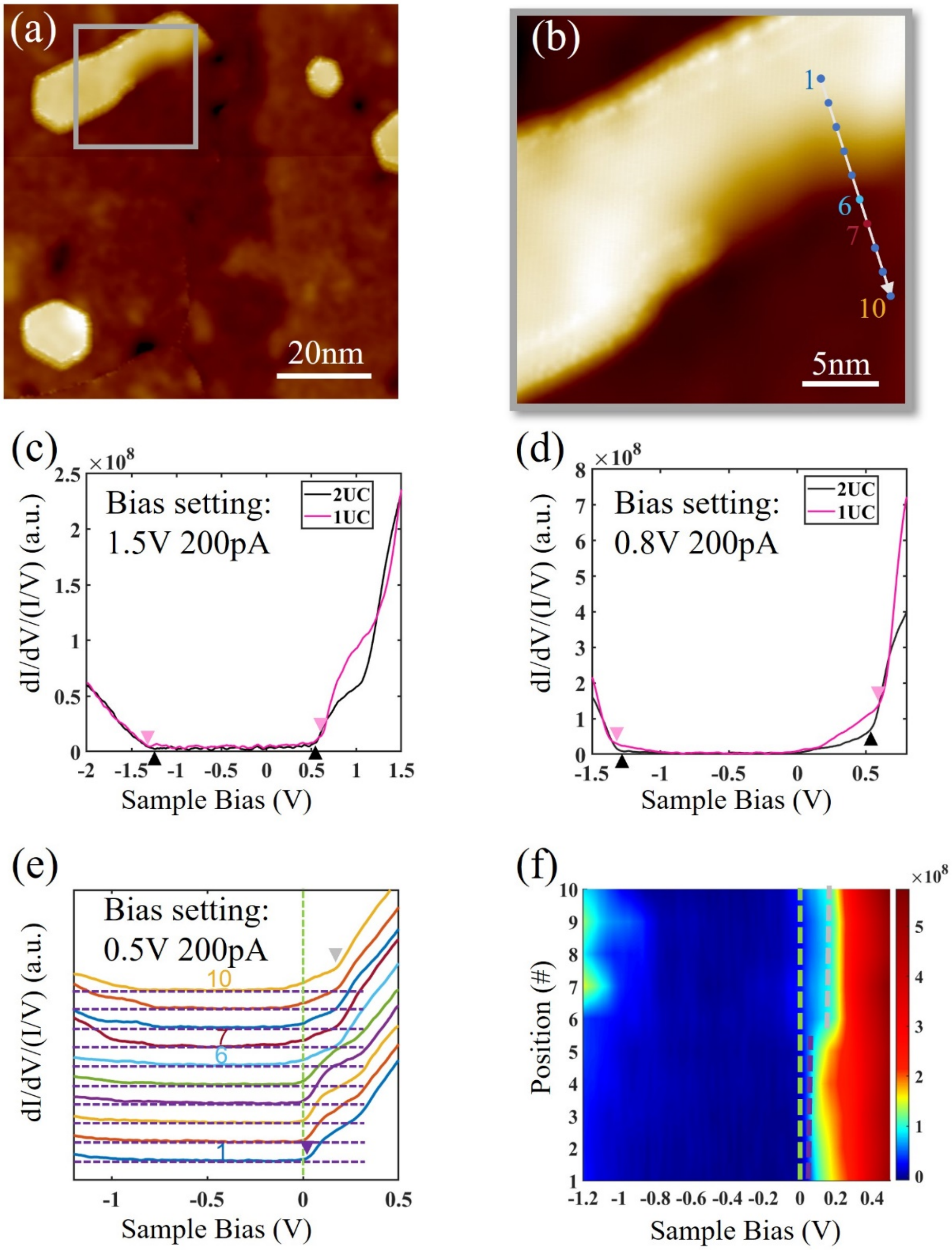

Figure 6-7: Charge transfer and band bending evolution at a partially connected island
(a) Large scale STM image (V_s = 2.5V, I_t = 5pA) showing the coexisting of stand-alone $SnSe_2$ second layer and partially connected second layer. Zoomed in image is shown in (b) (V_s = 0.8V, I_t = 100pA). (c-d) Large scale normalized STS spectra taken at monolayer (1UC, pink) and bilayer (2UC) $SnSe_2$ thin film at larger tip sample distance with bias setting at (V_s = 1.5V, I_t =2 00pA), (V_s = 0.8V, I_t = 200pA), respectively. The pink and black triangles mark the CBM' and VBM originating at the Γ point of the momentum space. (e) Normalized STS spectra taken along the

Figure 6-7 (cont'd)
grey line from second layer to the first layer at a reduced tip sample distance with bias setting at (V_s=0.5V, I_t=200pA). With reduced tip sample distance, CBM at the M point (larger parallel momentum) is visible, with emerging of a DOS tail penetrated below Fermi level that originates from the interfacial in-gap states between $SnSe_2$ and STO. The purple dash lines provide eye guide for the ground of each spectrum (f) DOS heat map across the same line in (b). Green dash line marks the Fermi level position in (e-f).

To correctly interpretate the results, one should remember that sensitivity of STS measurements to large parallel momentum depends critically on the tip-sample distance (more discussion in the section 2.2.5, Equation (2-17)). [147, 186] At large tip-sample distance (Figure 6-7(c)), the direct bandgap with CBM' and VBM both derived from Γ ($k_{//}$=0) point was revealed, showing a decrease in bandgap with increasing film thickness. This is in good agreement with theoretical prediction, likely arising from reduced quantum confinement and enhanced electrostatic screening.[205] At intermediate tip-sample distance (Figure 6-7(d)), we continue to observe the CBM' and VBM from Γ ($k_{//}$=0) point. At the same time, we also identify some DOS emerging near CBM' on both the first and second layer. For the first layer, DOS is also emerging on the VBM side, which is likely a combined effect of the increased tip sensitivity to DOS at larger parallel momentum and the observation of tail states. Upon even closer tip-sample distance (Figure 6-7(e)), more detailed electronic structures can be revealed. At the positive sample bias, the effect of increased tip sensitivity is evidenced by the observation of CBM at M (CBM(M)) point with a larger parallel momentum on both the first and second layer as marked by the grey and purple triangles, respectively. This agrees with our observation from $SnSe_2$ on HOPG sample in Chapter 4. It is also important to note that the measured indirect bandgap (~1.55V between CBM(M) point and VBM(Γ)) is slightly smaller than the calculated value (1.69V)[205] which is likely due to enhanced screening effect from the electron rich substrate. Tracing down from the second layer down to the first layer along the partially connected region (Figure 6-7(b,e,f)), CBM moves in the same direction as CBM', i.e., away from the FL which agrees with the theoretical calculation.[205]

Meanwhile, tail states are increasing in intensity as the tip is moving closer to the substrate interface. From the line profile STS curves, we can see negligible tail state density on the second layer, which gradually increases during the transition from second to first layer (points 5-6) and becomes pronounced on the first layer (points 7-10).

Due to the large electron affinity of $SnSe_2$, electrons are transferred from the STO(111) substrate to $SnSe_2$, which bends the CBM(M) of $SnSe_2$ towards the FL and confines the 2DEG at the interface.[238] Both CDW and SC of $SnSe_2$ depend on the electron carrier density near FL.[147, 195, 236-239] The tail states may have two different origins. (1) The DOS near CBM(M) contributed by the 2DEG which is located near the FL after band bending. (2) The virtually induced in-gap states with CBM(M) character developed at the heterointerface between the $SnSe_2$ and the STO(111) substrate.[238] It has been argued that the CDW is likely a consequence of the fermi surface nesting between the electron pockets at M, as near FL there is nearly no DOS at Γ. [238] And the SC is likely associated with the phonon mediated coupling for electron carriers near the FL.[147, 237] Thus, the degree of the filling of these tail states are expected to correlate to the emerging of CDW and SC in $SnSe_2$.[238] Near the VBM of $SnSe_2$, the virtually induced in-gap states are likely originated from localized states created by local defects which will vary from location to location. Note that the energy position of localized oxygen vacancy state of STO is near the VBM of $SnSe_2$ and the sub-bands of the STO 2DEG arising from the quantum confinements for the itinerant electrons are located near the FL.[264]

6.1.4 Strain Effect

The property of the $SnSe_2$/STO system relies critically on the morphology and interface. It is noticeable that the $SnSe_2$ monolayer is not completely uniform, which can be related to the presence of STO steps and nonuniformity in the dead layer. Within a single STO terrace, the previously observed dark and bright patches on the surface are due to the continuous $SnSe_2$ film

(Figure 6-8(a-b)) conforming over the non-uniform dead layer (Figure 6-8(c), Figure 6-5(b)). In another word, the dark area is closer to and the bright area is farther away from the substrate. According to our height measurement (Figure 6-8(c)), the relatively flat area is brightest thus sitting farthest, and the pit area is closest to the substrate along the line marked in (a).

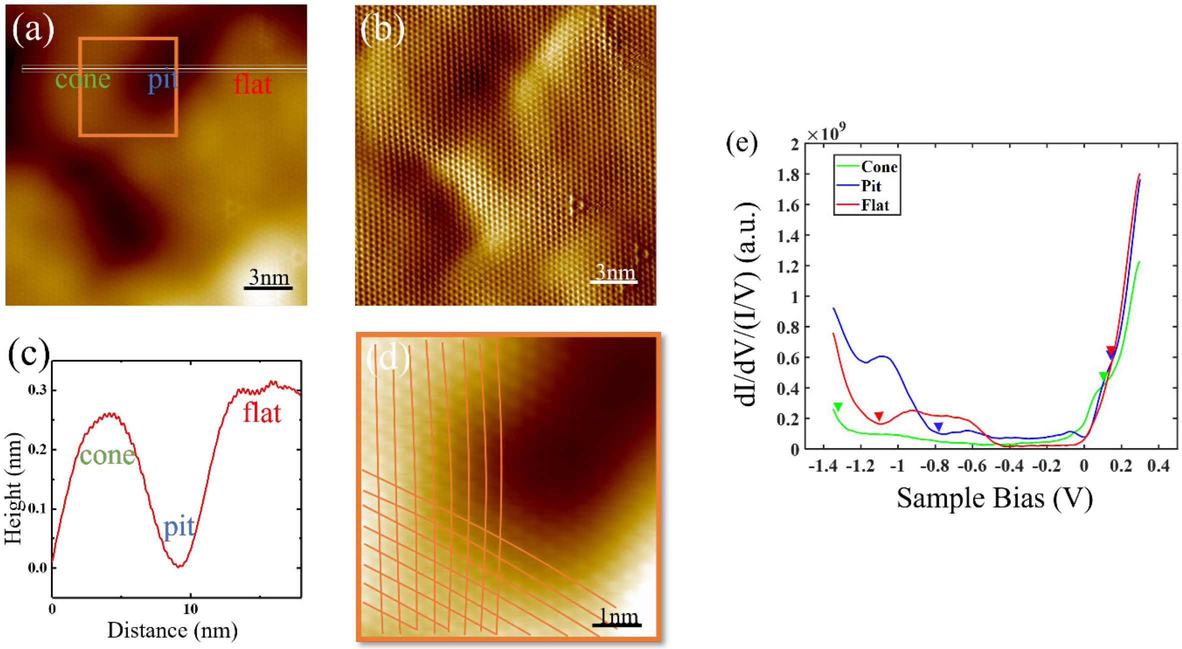

Figure 6-8: Strain variation on the as grown $SnSe_2$ film within the same terrace
(a) STM image ($V_s = 0.8V$, $I_t = 100pA$) of $SnSe_2$ on top of the same STO terrace reveals height variation, where the darker and brighter regions are not defects. The lattice continuity is clearly resolved in the current image ($V_s = 0.6V$, $I_t = 150pA$) in (b). According to the corresponding shape and height profile shown in (c), the locations are named cone, pit and flat regions. The lattice distortion as $SnSe_2$ film conforms to the underlying dead layer is clearly shown in the zoom-in image in (d) (from brown box in (a)), with the brown lines tracking the atom positions. (e) STS spectra ($V_s = 0.3V$, $I_t = 200pA$) taken at the cone, pit and flat regions, respectively.

The consequence of the height modulation on electronic structures of $SnSe_2$ is clearly reflected in our STS curves (Figure 6-8(e)). At the pit area, the tail states are observed over the entire bandgap range. At the cone and the flat areas, the density of tail states decreases with increasing distance to the substrate (Figure 6-8(e)). This is consistent with the nature of these tail states that is contributed by 2DEG and virtual induced-in gaps states as discussed previously.

However, near the VBM, the tail states vary significantly and randomly which is likely dominated by the localized defects states from the underlying dead layer.

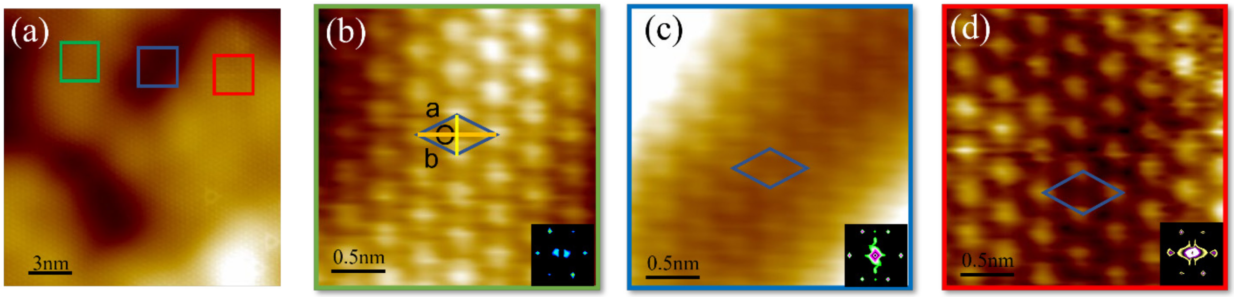

Figure 6-9: Lattice constant measurement
(a) Large scale STM image ($V_s = 0.8V$, $I_t = 100pA$). (b-d) Zoom-in STM ($V_s = 0.8V$, $I_t = 100pA$) at the green, blue and red box in (a). The orange and yellow bars in (b) are parallel to the armchair and zigzag directions, respectively. The unit cells are label with blue rhombic, which is extracted from the FFT image on the lower right corner. The average lattice constant of each region is listed below in Table 6-2.

	Cone	Pit	Flat
a(nm)	0.386(1.3%)	0.371(-2.6%)	0.376(-1.3%)
b(nm)	0.398(4.5%)	0.360(-5.5%)	0.380(-0.3%)
Zigzag strain (ε_x)	(5.2%)	(-6.8%)	(-1.0%)
Armchair strain(ε_y)	(1.1%)	(-2.3%)	(-1.1%)
Angle (degree)	56.24	59.14	59.46

Table 6-2: Lattice and strain variation on the uneven $SnSe_2$ film
The average lattice constants were extracted from Figure 6-9 by FFT images from the cone, pit and flat locations, respectively. Inside the paratheses are the strains calculated w.r.t the theoretical lattice constant of $SnSe_2$. For better comparison to previous studies, the strains along the zigzag and armchair direction are listed which are deduced by projecting of the strains along the a, b unit vector directions into the respective orthogonal directions.

Due to the height modulation, strain is also expected in $SnSe_2$. Figure 6-8(d) shows the lattice distortion tracked along the high symmetry directions. Table 6-2 lists the averaged local strain at the cone, pit and relatively flat area, respectively, deduced from the Fast Fourier Transformation (FFT) of STM images as noted in Figure 6-9. Consistent with the tracking along high symmetry directions (Figure 6-8(d)), the flat area has nearly no strain, where the film in the cone and pit areas suffer compressive and tensile strain, respectively. The $SnSe_2$ has positive Poisson ratio which is defined $\nu = -\varepsilon_y/\varepsilon_x$ if y direction is fully relaxed while x direction is strained (x, y directions are commonly denoted as the zigzag and armchair direction, respectively).[266] The fact that the strains are of the same sign along the x and y directions indicates a non-neglectable substrate interaction with the film. According to the previous DFT calculation,[129] the biaxial tensile strain tends to increase the bandgap in $SnSe_2$, and the compressive biaxial strain reduces the bandgap. Although the strain is not uniform in our sample, the general trend of bandgap evolution found in our STS measurements (Figure 6-8(e)) agrees well with the theory.[129] The bandgap is largest in tensile strained cone area and smallest in compressive strained pit area. For the flat area with very small compressive strain, the bump between -0.5V to -1.1V was contributed to the localized defects from the substrate/dead layer, so the overall bandgap with small strain is comparable to the result found in Figure 6-7.

Due to the strong charge transfer with the substrate, the CBM is bent towards the FL. The position of the CBM does not shift significantly which seems to suggest that the observed degree of strain is insufficient to significantly perturb the charge transfer behavior near FL. Nonetheless, small variations on the CBM shift are still visible as marked by the triangles, which is likely linked to the small variations of substrate work function (Figure 6-3(d)). Although the electronic structures of $SnSe_2$ film strongly vary with strain and local work function of the substrate, the density of tail states near CBM, which is a strong indicator of the interfacial charge transfer, critically depends on the film thickness and film roughness that determines the distance to STO substrate.

6.1.5 Discussion and Conclusion

The physical properties of $SnSe_2$ depend critically on the carrier density near FL which can be influenced by both the growth morphology and substrate interaction.[147, 195, 236-239] In previous studies, CDW and SC observed in $SnSe_2$ grown on different substrates were found to strongly tie to interfacial charge transfer.[147, 195, 238] Our systematic investigations of the local electronic structure variation on bare STO(111) substrate and $SnSe_2$ films grown on STO(111) provide valuable insights onto the interfacial phenomena occurring between $SnSe_2$ and charging donating substrate.

We observed a layer dependent growth mode of $SnSe_2$ on STO(111), identified the formation of a dead layer, and studied the influenced of the dead layer on growth morphology and electronic structures. The height variation of the dead layer is found to be an important factor in determining the growth morphology of the continuous $SnSe_2$ compact layers. On the first compact $SnSe_2$ layer, the height variation on the dead layer changes the distance between the film and the STO substrate, which will influence the degree of local charge transfer. Meanwhile, strain induced by the film conforming to the uneven dead layer/substrate will further modify the electronic structures of $SnSe_2$. Climbing up to the second compact layer in islands that are at the initial stage of the spiral growth, a decrease in the available states (tail states) for interfacial charge transfer is clearly observed. In a previous study, the coexisting of CDW and SC was discovered in $SnSe_2$ film grown on STO(001) substrate.[195, 238] Our study suggests that the variations on interfacial charge transfer, which is strongly correlated to film-substrate separation, are most likely responsible for the coexisting phases. This nonuniformity poses challenges on the applications of the system. For instance, percolated superconducting regions could be created throughout the film, which could significantly alter the macroscopic transport behaviors. The UHV treated STO hosts 2DEG and a strong electron donating ability, important for inducing exotic properties in $SnSe_2$.

Nonetheless, controlling the uniformity of $SnSe_2$ film remains difficult due to the formation of an uneven dead layer caused by the strong interfacial interaction. It warrants future studies to explore surface modification techniques towards growth of uniform $SnSe_2$ thin films on the strongly electron donating STO substrates.

6.2 Investigation of $SnSe_2$/WSe_2/STO(111) Vertical Heterostructure

From the previous investigation on the bare STO(111) surface, we understand that the key factors that influence the electronic properties of $SnSe_2$ are the work function difference of the substrate and the quality of the as-grown film. Here, we cover the STO surface with a thin layer of vdW-like material to modify the surface properties including work function with the aim of achieving a high-quality growth and more charge transfer with $SnSe_2$ adlayer. As pointed out in Chapter 4, WSe_2 is a layered materials with two different phases. The 1H-WSe_2 is a semiconductor and the 1T′-WSe_2 was found to be a 2D TI. The work function of 1T′-WSe_2 is ~2.36eV, which is significantly lower than the work functions of graphene(~4.56eV), STO(~4.26eV), 1H-WSe_2 (~4.08eV) and $SnSe_2$(~5.30eV).[202, 257, 267, 268] Covering STO substrate with 1T′-WSe_2 will likely significantly increase the ability of the substrate to dope $SnSe_2$, and consequently the possibility of inducing SC in $SnSe_2$ film. This work is ongoing, and some preliminary results will be presented below.

6.2.1 WSe_2 Deposition on STO(111)

In order to reuse the STO substrate after thin film deposition, Ar sputtering is used to remove the surface layers. The sputtering condition is weaker than the conditions used for metal surfaces, which was carried out at 1.5kV beam energy and 12μA electron flux. After annealing under the same condition as mentioned previously, we recovered a surface that is dominated by the 4 × 4 surface RC which is likely due to the removal of more oxygen during sputtering.[246, 248] The surface is shown in Figure 6-10.

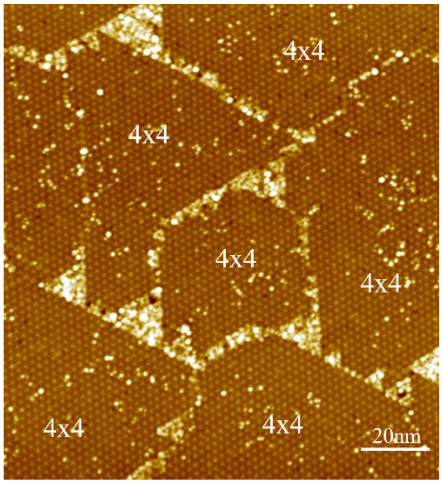

Figure 6-10: Surface reconstruction after Ar sputter and annealing
Due to Argon sputtering the surface is rougher with less oxygen. The annealing can no longer recover the 3 × 3 RC under the same annealing condition. The remaining areas are 6 × 6 RC with absorbates.

As WSe_2 decomposed at a much high temperature than $SnSe_2$, the growth is carried out at much higher substrate temperature (~623K to ~723K). Atomically smooth and compact WSe_2 islands are formed without the presence of small clusters on surface when the substrate temperature is above 673K. At lower temperatures, tall nano rod features are observed (Figure 6-11(a)). The H and T′ phases are coexisting on the surface which can be distinguished by their color contrast originated from DOS difference (Figure 6-11(c-d)). Zoomed-in image of the T′ phase shows the characteristic strip feature which agrees with Figure 4-1 (d-e) in Chapter 4. At our current temperature range, the phase transition appears to be dominated by the coverage or more specifically it depends on the merging of WSe_2 islands. The substrate temperature is higher in Figure 6-11(c) than in Figure 6-11(d), but there are more T′ phase in Figure 6-11(c) when the islands are isolated. Continue to increase the coverage of Figure 6-11(c), all 1st layer island will transform into the H phase. This likely suggests that the phase transition is induced by the random strain originated from the merging of the misaligned islands.

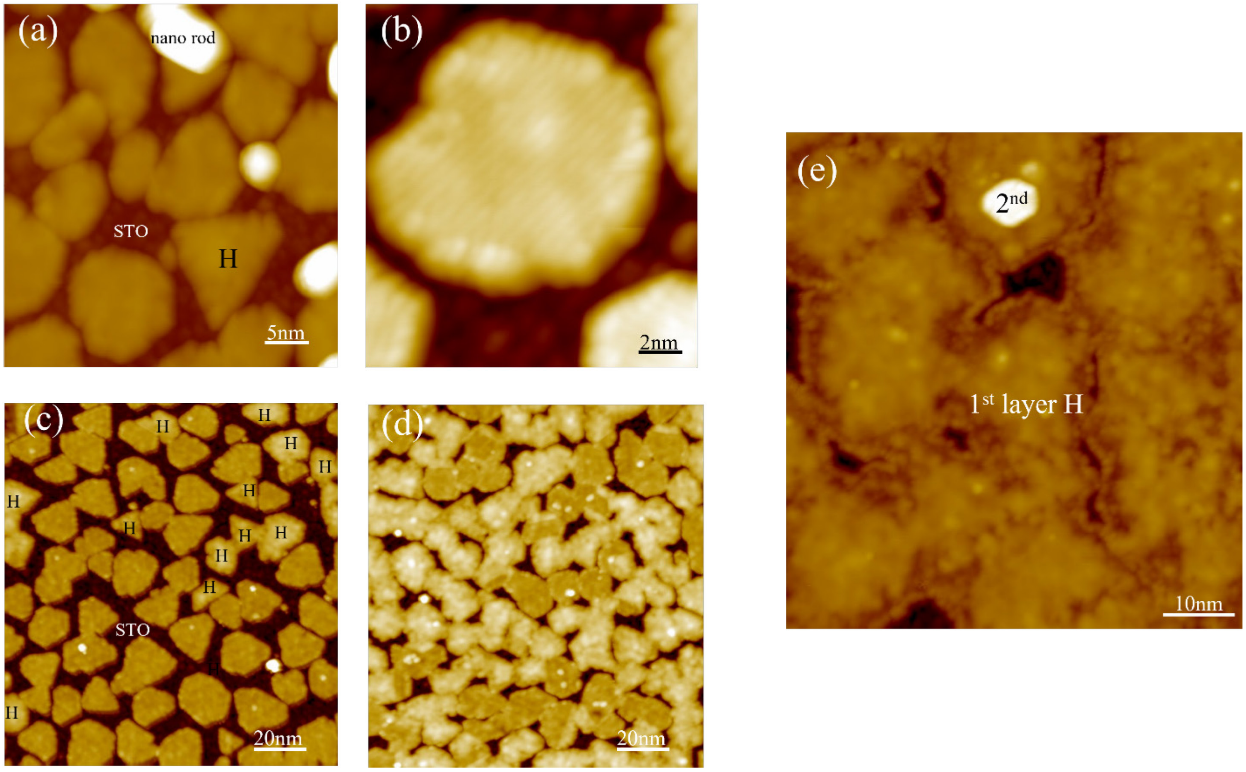

Figure 6-11: Temperature and coverage evolution of WSe_2 morphology on STO(111)
(a) STM image ($V_s = 2V$, $I_t = 5pA$) of WSe_2 deposited at STO(111) at substrate temperature ~623K. Only the H-phase island is labelled, as well as the tall nano rod feature. (b) Zoom in STM image ($V_s = 1V$, $I_t = 30pA$) of the T′ phase shows characteristic stripe feature. (c) STM image (V_s=2V, I_t=5pA) of WSe_2 deposited on STO(111) at substrate temperature ~723K. All the brighter H phase are labelled. The islands are mostly isolated. (d) STM image ($V_s = 2V$, $I_t = 5pA$) of WSe_2 deposited at STO(111) at substrate temperature ~673K. Bright domains are H phase. Islands being to merge with increasing percentage of H phase. (e) STM image ($V_s = 1.5V$, $I_t = 5pA$) of WSe_2 deposited at STO(111) at substrate temperature ~723K with higher coverage. All first layer islands are now converted to H phase.

In Chapter 4, we observed edge state inside the bulk gap for T′-WSe_2 on HOPG and revealed that the topological properties remain intact on the weakly interacting substrate. Nonetheless, the growth morphology of T′-WSe_2 on STO substrate, i.e., small island size and high island density, suggests that the interfacial interaction strength is higher than that on the HOPG substrate. This is likely the reason why the T′ phase can be stabilized on STO at a much higher temperature. However, if we probe the electronic structure of the T′ phase, its topological properties appear to be quenched due to the strong interfacial interaction, as the film becomes metallic without the emergence of edge states (Figure 6-12). At the same time, for the H phase, the morphology (rougher) and electronic structures are also very different in the center and at the edge, as revealed in the STM image (Figure 6-11). This rough edge is likely originated from the interaction between the dangling bonds at the edge of WSe_2 island and the STO(111) surface. At the center of the H-phase, the film appears to be n-doped (Figure 6-12(b)) likely from 2DEG of the STO. But at the edge, defect states arise near the valence band, which p dopes the island.

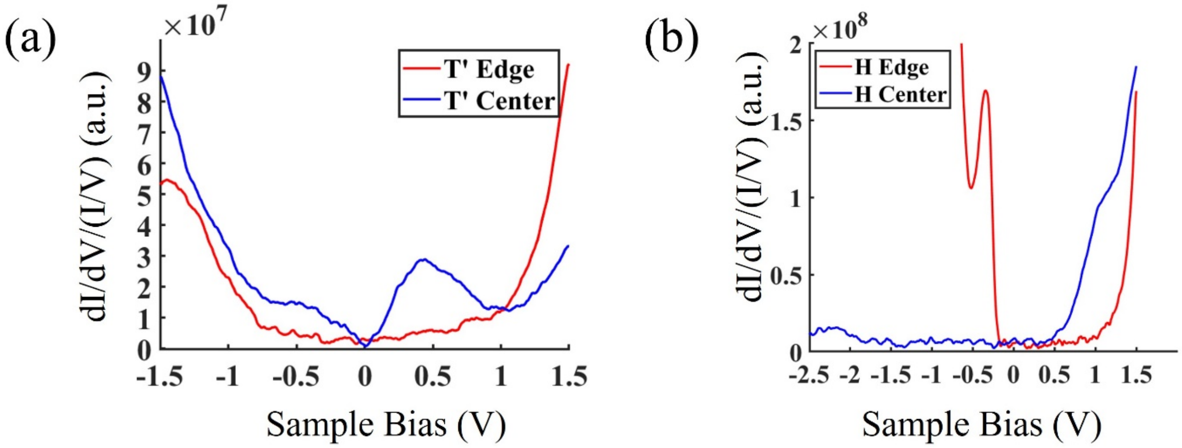

Figure 6-12: Electronic structure of different phase of WSe_2 on STO(111)
(a) STS spectra ($V_s = 1.5V$, $I_t = 100pA$) taken at the edge and center of the T′-WSe_2, respectively. (a) STS spectra taken at the edge and center of the H-WSe_2, respectively. ($V_s = 1.5V$, $I_t = 100pA$) for edge. ($V_s = 1.5V$, $I_t = 150pA$) for center.

6.2.2 $SnSe_2$ Deposition on WSe_2 Covered STO Substrate and Future Perspectives

For the incoming $SnSe_2$ deposition, different interaction schemes are simultaneously present on this surface, as WSe_2 is not completely covering the STO substrate. On top of the WSe_2 islands, the interaction strength is significantly reduced where atoms are allowed to diffuse across the entire island (~10nm in size) with nearly no nucleation (nanoparticle). After overcoming ESB at the edge, small clusters are formed to fill the voids between WSe_2 islands due to combined effects of dangling bonds on the edge of WSe_2 islands and the interaction to STO substrate (Figure 6-13(b)). Upon continued deposition of $SnSe_2$, compact islands are found on top of both WSe_2 islands and nanoparticles filling the voids (Figure 6-13(c)). Thus, the relationship between growth morphology and substrate interaction strength can be constructed on this surface, which confirms our previous hypothesis on the growth of $SnSe_2$ on bare STO(111). The formation of screw dislocation (e.g. partially connected second layer) are more pronounced on the STO surface partially covered by WSe_2, since this surface exhibits a bigger variation on the height (Figure 6-13(c)).

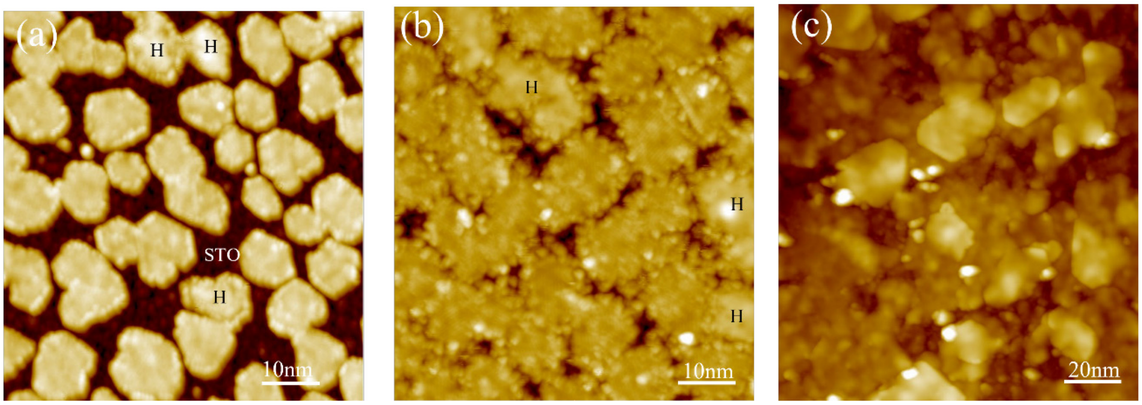

Figure 6-13: $SnSe_2$ deposition on WSe_2 covered STO substrate
(a) STM image ($V_s = 2.0V$, $I_t = 5pA$) showing growth morphology of sub monolayer WSe_2 on STO(111). Two phases of WSe_2 are found (H and T′). They are differentiable by the color contrast originated from the DOS difference. The H phase are labeled, and the other islands are T′. The voids in between are exposed STO. (b) STM image ($V_s = 2.0V$, $I_t = 5pA$) showing the voids filled

Figure 6-13 (cont'd)
by small clusters after $SnSe_2$ deposition. (c) STM image (V_s = 2.0V, I_t = 5pA) revealing predominately partially connected second layer $SnSe_2$ islands with increased coverage.

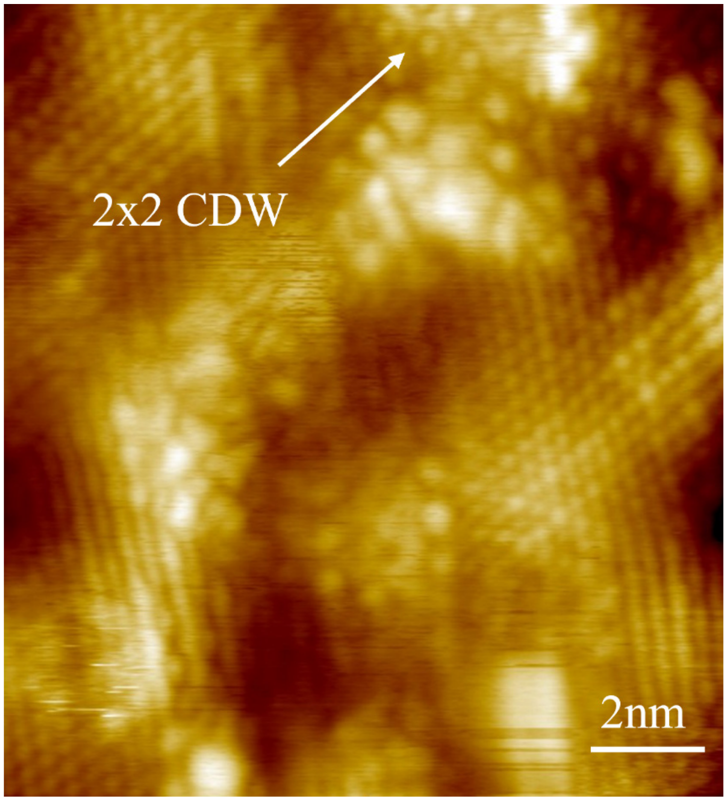

Figure 6-14: Emerging of local CDW on $SnSe_2$ on WSe_2/STO(111)
STM image (V_s = 0.5V, I_t=30pA) of $SnSe_2$ on top of coexisting T′ and H WSe_2 on STO(111) substrate, the actual phase underneath is unknown.

The STM image of $SnSe_2$ at (V_s = 0.5V, I_t=30pA) reveals very interesting 2x2 CDW phase coexisting with other phases on top of the T′ and H WSe_2 on STO(111) substrate (Figure 6-14). This CDW phase is not previously observed on the HOPG substrate or the bare STO (111) at the liquid nitrogen temperature (~77K), which suggests changing of the electron doping ability with modified surface. The local carrier density in the $SnSe_2$ film is different which is likely due to the varying doping ability of the H- and T′-WSe_2 passivated STO substrate. Nonetheless, it is difficult to differentiate the H and T′ WSe_2 phases as they are now underneath the $SnSe_2$ thin film. To correctly assign the electronic modification from the substrate, the next step in this project will be to produce single phase WSe_2 on STO substrate for $SnSe_2$ deposition. Then the system can be cooled down to liquid helium temperature (~4K) to investigate the possibility of the SC transition.

7 Conclusion and Future Prospects

In the process of tailoring the electronic design via incorporation of low-dimensional quantum materials (organic and inorganics) into HSs for the creation and enhancement of novel properties, the interfacial interactions need to be carefully considered. In this thesis, we have demonstrated the ability to tune the physical structure of thin film from the deposition of the adaptive 2D Sn on a versatile h-BN on metal substrate. We have also demonstrated a new phase transition mechanism based on the propagation of stress from shell to core on the lateral $WSe_2/SnSe_2$ core-shell structure on weakly interacting HOPG substrate. The topological property of the T′-WSe_2 core is found to be intact. The $SnSe_2$/graphene HS is expected to be superconducting at low temperature (~4.8K) which is adjacent to the edge state of the 2D TI. It is convenient to study the superconducting proximity effect on this lateral HS with exposed interface, which warrants further study. From the microscopic investigation of the organic K-TCNQ and TCNQ lateral HS, we were able to make the connection between the emergence of the local continuous DOS to the macroscopic insulator-to-metal transition. Finally, the exploration of $SnSe_2$ thin film on modified STO(111) surfaces for understanding the influence of interfacial interactions is still ongoing. We investigated the growth morphology and electronic perturbation from the bare 3×3 RC STO(111) surface. After the deposition of a monolayer WSe_2 on the surface, CDW emerges at liquid nitrogen temperature. The detailed electronic contributions from the different phases of WSe_2 and the superconducting T_c in the system is yet to be determined. Both the superconducting proximity effect in the $WSe_2/SnSe_2$ core-shell lateral HS on HOPG and the superconducting phenomenon in the $SnSe_2/WSe_2$/STO(111) vertical heterostructure can be investigated in the future after the systems are cooled down further to accommodate the relatively low T_c.

BIBLIOGRAPHY

BIBLIOGRAPHY

[1] Cava R, de Leon N and Xie W 2021 Introduction: Quantum Materials *Chem. Rev.* **121** 2777-9

[2] Wang H, Liu F, Fu W, Fang Z, Zhou W and Liu Z 2014 Two-dimensional heterostructures: fabrication, characterization, and application *Nanoscale* **6** 12250-72

[3] Wang J, Li Z, Chen H, Deng G and Niu X 2019 Recent Advances in 2D Lateral Heterostructures *Nanomicro. Lett.* **11** 48

[4] Sun Y, Wang D and Shuai Z 2016 Indirect-to-Direct Band Gap Crossover in Few-Layer Transition Metal Dichalcogenides: A Theoretical Prediction *J. Phys. Chem. C* **120** 21866-70

[5] Li M-Y, Chen C-H, Shi Y and Li L-J 2016 Heterostructures based on two-dimensional layered materials and their potential applications *Mater. Today* **19** 322-35

[6] Ohtomo A and Hwang H Y 2004 A high-mobility electron gas at the LaAlO3/SrTiO3 heterointerface *Nature* **427** 423-6

[7] Gariglio S, Reyren N, Caviglia A D and Triscone J M 2009 Superconductivity at the LaAlO(3)/SrTiO(3) interface *J. Phys. Condens. Matter* **21** 164213

[8] Ben Shalom M, Sachs M, Rakhmilevitch D, Palevski A and Dagan Y 2010 Tuning spin-orbit coupling and superconductivity at the SrTiO{3}/LaAlO{3} interface: a magnetotransport study *Phys. Rev. Lett.* **104** 126802

[9] Bert J A, Kalisky B, Bell C, Kim M, Hikita Y, Hwang H Y and Moler K A 2011 Direct imaging of the coexistence of ferromagnetism and superconductivity at the LaAlO3/SrTiO3 interface *Nat. Phys.* **7** 767-71

[10] Jerome D 2004 Organic conductors: From charge density wave TTF-TCNQ to superconducting (TMTSF)(2)PF6 *Chem. Rev.* **104** 5565-91

[11] Saito G and Yoshida Y 2007 Development of conductive organic molecular assemblies: Organic metals, superconductors, and exotic functional materials *B. Chem. Soc. Jpn.* **80** 1-137

[12] Kagawa F, Horiuchi S, Tokunaga M, Fujioka J and Tokura Y 2010 Ferroelectricity in a one-dimensional organic quantum magnet *Nat. Phys.* **6** 169-72

[13] Saito G and Murata T 2008 Mixed valency in organic charge transfer complexes *Philos. T. R. Soc. A* **366** 139-50

[14] Peng Z, Chen X, Fan Y, Srolovitz D J and Lei D 2020 Strain engineering of 2D semiconductors and graphene: from strain fields to band-structure tuning and photonic applications *Light. Sci. Appl.* **9** 190

[15] Li W, Qian X and Li J 2021 Phase transitions in 2D materials *Nat. Rev. Mater.* **6** 829-46

[16] Zhang C, Chuu C P, Ren X, Li M Y, Li L J, Jin C, Chou M Y and Shih C K 2017 Interlayer couplings, Moire patterns, and 2D electronic superlattices in MoS_2/WSe_2 hetero-bilayers *Sci. Adv.* **3** e1601459

[17] Zhang H M, Zhang D, Lu X W, Liu C, Zhou G Y, Ma X C, Wang L L, Jiang P, Xue Q K and Bao X H 2017 Origin of charge transfer and enhanced electron-phonon coupling in single unit-cell FeSe films on $SrTiO_3$ *Nat. Commun.* **8** 214

[18] Wang J and Zhang S C 2017 Topological states of condensed matter *Nat. Mater.* **16** 1062-7

[19] Shi H, Pan H, Zhang Y-W and Yakobson B I 2013 Quasiparticle band structures and optical properties of strained monolayer MoS_2 and WS_2 *Phys. Rev. B* **87** 155304

[20] Konig M, Wiedmann S, Brune C, Roth A, Buhmann H, Molenkamp L W, Qi X L and Zhang S C 2007 Quantum spin hall insulator state in HgTe quantum wells *Science* **318** 766-70

[21] Fu L, Kane C L and Mele E J 2007 Topological insulators in three dimensions *Phys. Rev. Lett.* **98** 106803

[22] Hsieh D, Qian D, Wray L, Xia Y, Hor Y S, Cava R J and Hasan M Z 2008 A topological Dirac insulator in a quantum spin Hall phase *Nature* **452** 970-4

[23] Fu L 2011 Topological crystalline insulators *Phys. Rev. Lett.* **106** 106802

[24] Murakami S 2008 Phase transition between the quantum spin Hall and insulator phases in 3D: emergence of a topological gapless phase *New J. Phys.* **10** 029802

[25] Klitzing K v, Dorda G and Pepper M 1980 New Method for High-Accuracy Determination of the Fine-Structure Constant Based on Quantized Hall Resistance *Phys. Rev. Lett.* **45** 494-7

[26] Buttiker M 1988 Absence of backscattering in the quantum Hall effect in multiprobe conductors *Phys. Rev. B Condens. Matter.* **38** 9375-89

[27] Bernevig B A and Zhang S C 2006 Quantum spin Hall effect *Phys. Rev. Lett.* **96** 106802

[28] Kane C L and Mele E J 2005 Z2 topological order and the quantum spin Hall effect *Phys. Rev. Lett.* **95** 146802

[29] Šmejkal L, Mokrousov Y, Yan B and MacDonald A H 2018 Topological antiferromagnetic spintronics *Nat. Phys.* **14** 242-51

[30] Fu L and Kane C L 2009 Josephson current and noise at a superconductor/quantum-spin-Hall-insulator/superconductor junction *Phys. Rev. B* **79** 161408(R)

[31] Das Sarma S, Freedman M and Nayak C 2015 Majorana zero modes and topological quantum computation *Npj Quantum Inform.* **1** 15001

[32] Hatsugai Y 1993 Chern number and edge states in the integer quantum Hall effect *Phys. Rev. Lett.* **71** 3697-700

[33] Fu L and Kane C L 2007 Topological insulators with inversion symmetry *Phys. Rev. B* **76** 045302

[34] Yao Y, Ye F, Qi X-L, Zhang S-C and Fang Z 2007 Spin-orbit gap of graphene: First-principles calculations *Phys. Rev. B* **75** 041401(R)

[35] Zhang D, Wang J, DaSilva A M, Lee J S, Gutierrez H R, Chan M H W, Jain J and Samarth N 2011 Superconducting proximity effect and possible evidence for Pearl vortices in a candidate topological insulator *Phys. Rev. B* **84** 165120

[36] Sochnikov I, Bestwick A J, Williams J R, Lippman T M, Fisher I R, Goldhaber-Gordon D, Kirtley J R and Moler K A 2013 Direct measurement of current-phase relations in superconductor/topological insulator/superconductor junctions *Nano Lett.* **13** 3086-92

[37] Williams J R, Bestwick A J, Gallagher P, Hong S S, Cui Y, Bleich A S, Analytis J G, Fisher I R and Goldhaber-Gordon D 2012 Unconventional Josephson effect in hybrid superconductor-topological insulator devices *Phys. Rev. Lett.* **109** 056803

[38] Beenakker C W J 2013 Search for Majorana Fermions in Superconductors *Annu. Rev. Condens. Matter Phys.* **4** 113-36

[39] Fu L and Kane C L 2008 Superconducting proximity effect and majorana fermions at the surface of a topological insulator *Phys. Rev. Lett.* **100** 096407

[40] Trainer D J, Zhang Y, Bobba F, Xi X, Hla S W and Iavarone M 2019 The Effects of Atomic-Scale Strain Relaxation on the Electronic Properties of Monolayer MoS_2 *ACS Nano* **13** 8284-91

[41] Liu C X, Qi X L, Dai X, Fang Z and Zhang S C 2008 Quantum anomalous hall effect in Hg1-yMnyTe quantum wells *Phys. Rev. Lett.* **101** 146802

[42] Chang C Z, Zhang J, Feng X, Shen J, Zhang Z, Guo M, Li K, Ou Y, Wei P, Wang L L, Ji Z Q, Feng Y, Ji S, Chen X, Jia J, Dai X, Fang Z, Zhang S C, He K, Wang Y, Lu L, Ma X C and Xue Q K 2013 Experimental observation of the quantum anomalous Hall effect in a magnetic topological insulator *Science* **340** 167-70

[43] Mermin N D and Wagner H 1966 Absence of Ferromagnetism or Antiferromagnetism in One- or Two-Dimensional Isotropic Heisenberg Models *Phys. Rev. Lett.* **17** 1133-6

[44] Hohenberg P C 1967 Existence of Long-Range Order in One and Two Dimensions *Phy. Rev.* **158** 383-6

[45] Qi X-L, Hughes T L and Zhang S-C 2008 Topological field theory of time-reversal invariant insulators *Phys. Rev. B* **78** 195424

[46] He K and Xue Q K 2019 Quantum anomalous Hall heterostructures *Natl. Sci. Rev.* **6** 202-4

[47] Lee C, Katmis F, Jarillo-Herrero P, Moodera J S and Gedik N 2016 Direct measurement of proximity-induced magnetism at the interface between a topological insulator and a ferromagnet *Nat. Commun.* **7** 12014

[48] Jiang Z, Chang C Z, Tang C, Wei P, Moodera J S and Shi J 2015 Independent Tuning of Electronic Properties and Induced Ferromagnetism in Topological Insulators with Heterostructure Approach *Nano Lett.* **15** 5835-40

[49] Alegria L D, Ji H, Yao N, Clarke J J, Cava R J and Petta J R 2014 Large anomalous Hall effect in ferromagnetic insulator-topological insulator heterostructures *Appl. Phys. Lett.* **105** 053512

[50] Sun H-H and Jia J-F 2017 Majorana zero mode in the vortex of an artificial topological superconductor *Sci. China Phys., Mech. & Astron.* **60** 057401

[51] He Q L, Pan L, Stern A L, Burks E C, Che X, Yin G, Wang J, Lian B, Zhou Q, Choi E S, Murata K, Kou X, Chen Z, Nie T, Shao Q, Fan Y, Zhang S C, Liu K, Xia J and Wang K L 2017 Chiral Majorana fermion modes in a quantum anomalous Hall insulator-superconductor structure *Science* **357** 294-9

[52] Kayyalha M, Xiao D, Zhang R, Shin J, Jiang J, Wang F, Zhao Y F, Xiao R, Zhang L, Fijalkowski K M, Mandal P, Winnerlein M, Gould C, Li Q, Molenkamp L W, Chan M H W, Samarth N and Chang C Z 2020 Absence of evidence for chiral Majorana modes in quantum anomalous Hall-superconductor devices *Science* **367** 64-7

[53] Xu Y, Yan B, Zhang H J, Wang J, Xu G, Tang P, Duan W and Zhang S C 2013 Large-gap quantum spin Hall insulators in tin films *Phys. Rev. Lett.* **111** 136804

[54] Bergeron H, Lebedev D and Hersam M C 2021 Polymorphism in Post-Dichalcogenide Two-Dimensional Materials *Chem. Rev.* **121** 2713-75

[55] Xiao Y, Zhou M, Liu J, Xu J and Fu L 2019 Phase engineering of two-dimensional transition metal dichalcogenides *Sci. China Mater.* **62** 759-75

[56] Chandran M 2019 Chapter Six - Synthesis, Characterization, and Applications of Diamond Films. In Carbon-Based Nanofillers and Their Rubber Nanocomposites; Yaragalla, S., Mishra, R., Thomas, S., Kalarikkal, N., Maria, H. J., Eds.; *Elsevier* pp 183-224

[57] McCulloch D G, Wong S, Shiell T B, Haberl B, Cook B A, Huang X, Boehler R, McKenzie D R and Bradby J E 2020 Investigation of Room Temperature Formation of the Ultra-Hard Nanocarbons Diamond and Lonsdaleite *Small* **16** e2004695

[58] Duerloo K A, Li Y and Reed E J 2014 Structural phase transitions in two-dimensional Mo- and W-dichalcogenide monolayers *Nat. Commun.* **5** 4214

[59] Liu C C, Feng W and Yao Y 2011 Quantum spin Hall effect in silicene and two-dimensional germanium *Phys. Rev. Lett.* **107** 076802

[60] Wu S, Fatemi V, Gibson Q D, Watanabe K, Taniguchi T, Cava R J and Jarillo-Herrero P 2018 Observation of the quantum spin Hall effect up to 100 kelvin in a monolayer crystal *Science* **359** 76-9

[61] Tang S J, Zhang C F, Wong D, Pedramrazi Z, Tsai H Z, Jia C J, Moritz B, Claassen M, Ryu H, Kahn S, Jiang J, Yan H, Hashimoto M, Lu D H, Moore R G, Hwang C C, Hwang C, Hussain Z, Chen Y L, Ugeda M M, Liu Z, Xie X M, Devereaux T P, Crommie M F, Mo S K and Shen Z X 2017 Quantum spin Hall state in monolayer 1T '-WTe_2 *Nat. Phys.* **13** 683–7

[62] Chen P, Pai W W, Chan Y H, Sun W L, Xu C Z, Lin D S, Chou M Y, Fedorov A V and Chiang T C 2018 Large quantum-spin-Hall gap in single-layer 1T' WSe_2 *Nat. Commun.* **9** 2003

[63] Ugeda M M, Pulkin A, Tang S, Ryu H, Wu Q, Zhang Y, Wong D, Pedramrazi Z, Martin-Recio A, Chen Y, Wang F, Shen Z X, Mo S K, Yazyev O V and Crommie M F 2018 Observation of topologically protected states at crystalline phase boundaries in single-layer WSe_2 *Nat. Commun.* **9** 3401

[64] Yang H, Kim S W, Chhowalla M and Lee Y H 2017 Structural and quantum-state phase transition in van der Waals layered materials *Nat. Phys.* **13** 931-7

[65] Zhu F F, Chen W J, Xu Y, Gao C L, Guan D D, Liu C H, Qian D, Zhang S C and Jia J F 2015 Epitaxial growth of two-dimensional stanene *Nat. Mater.* **14** 1020–5

[66] Deng J, Xia B, Ma X, Chen H, Shan H, Zhai X, Li B, Zhao A, Xu Y, Duan W, Zhang S C, Wang B and Hou J G 2018 Epitaxial growth of ultraflat stanene with topological band inversion *Nat. Mater.* **17** 1081-6

[67] Chen W, Xie X, Zong J, Chen T, Lin D, Yu F, Jin S, Zhou L, Zou J, Sun J, Xi X and Zhang Y 2019 Growth and Thermo-driven Crystalline Phase Transition of Metastable Monolayer 1T'-WSe_2 Thin Film *Sci. Rep.* **9** 2685

[68] Wada M, Murakami S, Freimuth F and Bihlmayer G 2011 Localized edge states in two-dimensional topological insulators: Ultrathin Bi films *Phys. Rev. B* **83** 121310(R)

[69] Murakami S 2011 Two-dimensional topological insulators and their edge states *J. Phys.: Conf. Ser.* **302** 012019

[70] Teichert F, Zienert A, Schuster J and Schreiber M 2014 Strong localization in defective carbon nanotubes: a recursive Green's function study *New J. Phys.* **16** 123026

[71] Tang P Z, Chen P C, Cao W D, Huang H Q, Cahangirov S, Xian L D, Xu Y, Zhang S C, Duan W H and Rubio A 2014 Stable two-dimensional dumbbell stanene: A quantum spin Hall insulator *Phys. Rev. B* **90** 121408(R)

[72] Gou J, Kong L J, Li H, Zhong Q, Li W B, Cheng P, Chen L and Wu K H 2017 Strain-induced band engineering in monolayer stanene on Sb(111) *Phy. Rev. Mater.* **1** 054004

[73] Zang Y Y, Jiang T, Gong Y, Guan Z Y, Liu C, Liao M H, Zhu K J, Li Z, Wang L L, Li W, Song C L, Zhang D, Xu Y, He K, Ma X C, Zhang S C and Xue Q K 2018 Realizing an Epitaxial Decorated Stanene with an Insulating Bandgap *Adv. .Funct. Mater.* **28** 201802723

[74] Chou B H, Huang Z Q, Hsu C H, Chuang F C, Liu Y T, Lin H and Bansil A 2014 Hydrogenated ultra-thin tin films predicted as two-dimensional topological insulators *New J. Phys.* **16** 115008

[75] Auwärter W 2019 Hexagonal boron nitride monolayers on metal supports: Versatile templates for atoms, molecules and nanostructures *Surf. Sci. Rep.* **74** 1-95

[76] Farwick Zum Hagen F H, Zimmermann D M, Silva C C, Schlueter C, Atodiresei N, Jolie W, Martinez-Galera A J, Dombrowski D, Schroder U A, Will M, Lazic P, Caciuc V, Blugel S, Lee T L, Michely T and Busse C 2016 Structure and Growth of Hexagonal Boron Nitride on Ir(111) *ACS Nano* **10** 11012-26

[77] Janod E, Tranchant J, Corraze B, Querre M, Stoliar P, Rozenberg M, Cren T, Roditchev D, Phuoc V T, Besland M P and Cario L 2015 Resistive Switching in Mott Insulators and Correlated Systems *Adv. Funct. Mater.* **25** 6287-305

[78] Mo X L, Chen G R, Cai Q J, Fan Z Y, Xu H H, Yao Y, Yang J, Gu H H and Hua Z Y 2003 Preparation and electrical/optical bistable property of potassium tetracyanoquinodimethane thin films *Thin Solid Films* **436** 259-63

[79] Kagawa F, Miyagawa K and Kanoda K 2009 Magnetic Mott criticality in a kappa-type organic salt probed by NMR *Nat. Phys.* **5** 880-4

[80] Sasaki T, Yoneyama N, Kobayashi N, Ikemoto Y and Kimura H 2004 Imaging phase separation near the Mott boundary of the correlated organic superconductors kappa-(BEDT-TTF)2X *Phys. Rev. Lett.* **92** 227001

[81] de Souza M, Bruhl A, Strack C, Wolf B, Schweitzer D and Lang M 2007 Anomalous lattice response at the Mott transition in a quasi-2D organic conductor *Phys. Rev. Lett.* **99** 037003

[82] Muller J, Brandenburg J and Schlueter J A 2009 Magnetic-field induced crossover of superconducting percolation regimes in the layered organic Mott system kappa-(BEDT-TTF)$_2$Cu[N(CN)$_2$]Cl *Phys. Rev. Lett.* **102** 047004

[83] Kumai R, Okimoto Y and Tokura Y 1999 Current-induced insulator-metal transition and pattern formation in an organic charge-transfer complex *Science* **284** 1645-7

[84] Sasaki T, Yoneyama N, Suzuki A, Kobayashi N, Ikemoto Y and Kimura H 2005 Real Space Imaging of the Metal–Insulator Phase Separation in the Band Width Controlled Organic Mott System κ-(BEDT-TTF)$_2$Cu[N(CN)$_2$]Br *J. Phys. Soc. Japan* **74** 2351-60

[85] Sabeth F, Iimori T and Ohta N 2012 Insulator-Metal Transitions Induced by Electric Field and Photoirradiation in Organic Mott Insulator Deuterated kappa-(BEDT-TTF)$_2$Cu[N(CN)$_2$]Br *J Am. Chem. Soc.* **134** 6984-6

[86] Yamaguchi S and Potember R S 1995 STM tip induced phase transition of copper tetracyanoquinodimethane (CuTCNQ) *Mol. Cryst. Liq. Crys. A* **267** 241-8

[87] Jeong J, Aetukuri N, Graf T, Schladt T D, Samant M G and Parkin S S P 2013 Suppression of Metal-Insulator Transition in VO2 by Electric Field-Induced Oxygen Vacancy Formation *Science* **339** 1402-5

[88] Lee D, Chung B, Shi Y, Kim G Y, Campbell N, Xue F, Song K, Choi S Y, Podkaminer J P, Kim T H, Ryan P J, Kim J W, Paudel T R, Kang J H, Spinuzzi J W, Tenne D A, Tsymbal E Y, Rzchowski M S, Chen L Q, Lee J and Eom C B 2018 Isostructural metal-insulator transition in VO2 *Science* **362** 1037-40

[89] Xue W, Xu X-H and Liu G 2019 Solid-State Electrochemical Process and Performance Optimization of Memristive Materials and Devices *Chemistry* **1** 44-68

[90] Thomsen H 1950 Martin Knudsen. 1871-1949 *ICES J. Mar. Sci.* **16** 155-9

[91] Kooser K, Ha D T, Itala E, Laksman J, Urpelainen S and Kukk E 2012 Size selective spectroscopy of Se microclusters *J. Chem. Phys.* **137** 044304

[92] Lüth H 2010 *Solid Surfaces, Interfaces and Thin Films*: Springer

[93] Wilson R 2009 *Surface Analysis– The Principal Techniques,* pp 613-47

[94] Goose J E, First E L and Clancy P 2010 Nature of step-edge barriers for small organic molecules *Phys. Rev. B* **81** 205310

[95] Zhang X N, Barrena E, de Oteyza D G and Dosch H 2007 Transition from layer-by-layer to rapid roughening in the growth of DIP on SiO2 *Surf. Sci.* **601** 2420-5

[96] Schwoebel R L and Shipsey E J 1966 Step Motion on Crystal Surfaces *J. Appl. Phys.* **37** 3682-6

[97] Li S-C, Han Y, Jia J-F, Xue Q-K and Liu F 2006 Determination of the Ehrlich-Schwoebel barrier in epitaxial growth of thin films *Phys. Rev. B* **74** 195428

[98] Zheng H, Xie M H, Wu H S and Xue Q K 2008 Kinetic energy barriers on the GaN(0001) surface: A nucleation study by scanning tunneling microscopy *Phys. Rev. B* **77** 045303

[99] Krug J, Politi P and Michely T 2000 Island nucleation in the presence of step-edge barriers: Theory and applications *Physical Review B* **61** 14037-46

[100] Bauer E 1958 Phänomenologische Theorie der Kristallabscheidung an Oberflächen. I *Z. Kristallogr.* **110** 372-94

[101] Zou X, Liu Y and Yakobson B I 2013 Predicting dislocations and grain boundaries in two-dimensional metal-disulfides from the first principles *Nano Lett.* **13** 253-8

[102] Komsa H P and Krasheninnikov A V 2017 Engineering the Electronic Properties of Two-Dimensional Transition Metal Dichalcogenides by Introducing Mirror Twin Boundaries *Adv. Electron. Mater.* **3** 1600468

[103] Whitesides G M, Mathias, J.P. , Seto, C.T. 1991 Molecular self-assembly and nanochemistry—a chemical strategy for the synthesis of nanostructures *Science* **254** 1312

[104] Theobald J A, Oxtoby N S, Phillips M A, Champness N R and Beton P H 2003 Controlling molecular deposition and layer structure with supramolecular surface assemblies *Nature* **424** 1029-31

[105] Canas-Ventura M E, Xiao W, Wasserfallen D, Mullen K, Brune H, Barth J V and Fasel R 2007 Self-assembly of periodic bicomponent wires and ribbons *Angew. Chem.* **46** 1814-8

[106] Furukawa S, Tahara K, De Schryver F C, Van der Auweraer M, Tobe Y and De Feyter S 2007 Structural transformation of a two-dimensional molecular network in response to selective guest inclusion *Angew. Chem.* **46** 2831-4

[107] de Wild M, Berner S, Suzuki H, Yanagi H, Schlettwein D, Ivan S, Baratoff A, Guentherodt H-J and Jung T A 2002 A Novel Route To Molecular Self-Assembly: Self-Intermixed Monolayer Phases *ChemPhysChem* **3** 881-5

[108] Wakayama Y 2016 On-surface molecular nanoarchitectonics: From self-assembly to directed assembly *Jpn J. Appl. Phys.* **55** 1102AA

[109] Yokoyama T, Yokoyama S, Kamikado T, Okuno Y and Mashiko S 2001 Selective assembly on a surface of supramolecular aggregates with controlled size and shape *Nature* **413** 619-21

[110] Novoselov K S, Geim A K, Morozov S V, Jiang D, Katsnelson M I, Grigorieva I V, Dubonos S V and Firsov A A 2005 Two-dimensional gas of massless Dirac fermions in graphene *Nature* **438** 197-200

[111] N'Diaye A T, Bleikamp S, Feibelman P J and Michely T 2006 Two-dimensional Ir cluster lattice on a graphene moire on Ir(111) *Phys. Rev. Lett.* **97** 215501

[112] Kobayashi K 1996 Moire pattern in scanning tunneling microscopy: Mechanism in observation of subsurface nanostructures *Phys. Rev. B Condens. Matter* **53** 11091-9

[113] Kidambi P R, Blume R, Kling J, Wagner J B, Baehtz C, Weatherup R S, Schloegl R, Bayer B C and Hofmann S 2014 In Situ Observations during Chemical Vapor Deposition of Hexagonal Boron Nitride on Polycrystalline Copper *Chem. Mater.* **26** 6380-92

[114] Liu D S H, Hilse M and Engel-Herbert R 2021 Sticking coefficients of selenium and tellurium *J. Vac. Sci. Tech. A* **39** 023413

[115] Gerd Binnig and Rohrer H 1986 Scanning tunneling microscopy *IBM J. Res. Dev.* **30** 355–69

[116] Eigler D M and Schweizer E K 1990 Positioning single atoms with a scanning tunnelling microscope *Nature* **344** 524-6

[117] Wortmann D, Heinze S, Kurz P, Bihlmayer G and Blugel S 2001 Resolving complex atomic-scale spin structures by spin-polarized scanning tunneling microscopy *Phys. Rev. Lett.* **86** 4132-5

[118] Wiesendanger R, Brgler D, Tarrach G, Schaub T, Hartmann U, Gntherodt H J, Shvets I V and Coey J M D 1991 Recent advances in scanning tunneling microscopy involving magnetic probes and samples *Appl. Phys. A Solids Surf.* **53** 349-55

[119] Stroscio J and Kaiser W 1993 *Methods of Experimental Physics*: Academic Press pp 1-459

[120] Chen C J 2008 *Introduction to Scanning Tunneling Microscopy*: Oxford Science Publications

[121] Leggett G J 2009 *Surface Analysis– The Principal Techniques,* pp 479-562

[122] Tersoff J and Hamann D R 1983 Theory and Application for the Scanning Tunneling Microscope *Phys. Rev. Lett.* **50** 1998-2001

[123] Tersoff J and Hamann D R 1985 Theory of the scanning tunneling microscope *Phys. Rev. B Condens. Matter* **31** 805-13

[124] Bardeen J 1961 Tunnelling from a Many-Particle Point of View *Phys. Rev. Lett.* **6** 57-9

[125] Tersoff J and Hamann D R 1985 Theory of the scanning tunneling microscope *Phys. Rev. B* **31** 805-13

[126] Krane N, Lotze C and Franke K J 2018 Moiré structure of MoS2 on Au(111): Local structural and electronic properties *Surf. Sci.* **678** 136-42

[127] Guo Y, Pan F, Ye M, Wang Y, Pan Y, Zhang X, Li J, Zhang H and Lu J 2016 Interfacial properties of stanene–metal contacts *2D Mater.* **3** 035020

[128] Zhang S, Wang C G, Li M Y, Huang D, Li L J, Ji W and Wu S 2017 Defect Structure of Localized Excitons in a WSe_2 Monolayer *Phys. Rev. Lett.* **119** 046101

[129] Huang Y, Ling C, Liu H, Wang S and Geng B 2014 Versatile Electronic and Magnetic Properties of SnSe2 Nanostructures Induced by the Strain *J. Phys. Chem. C* **118** 9251-60

[130] Liu M, Shi J, Li Y, Zhou X, Ma D, Qi Y, Zhang Y and Liu Z 2017 Temperature-Triggered Sulfur Vacancy Evolution in Monolayer MoS_2/Graphene Heterostructures *Small* **13** 1602967

[131] Lee H J, Lee J H and Ho W 2005 Vibronic transitions in single metalloporphyrins *Chemphyschem* **6** 971-5

[132] Nazin G V, Wu S W and Ho W 2005 Tunneling rates in electron transport through double-barrier molecular junctions in a scanning tunneling microscope *Proc. Natl. Acad. Sci. USA* **102** 8832-7

[133] Pradhan N A, Liu N and Ho W 2005 Vibronic spectroscopy of single C60 molecules and monolayers with the STM *J. Phys. Chem. B* **109** 8513-8

[134] Ugeda M M, Bradley A J, Shi S F, da Jornada F H, Zhang Y, Qiu D Y, Ruan W, Mo S K, Hussain Z, Shen Z X, Wang F, Louie S G and Crommie M F 2014 Giant bandgap renormalization and excitonic effects in a monolayer transition metal dichalcogenide semiconductor *Nat. Mater.* **13** 1091-5

[135] Vion D, Orfila P F, Joyez P, Esteve D and Devoret M H 1995 Miniature electrical filters for single electron devices *J. Appl. Phys.* **77** 2519-24

[136] Wiebe J, Wachowiak A, Meier F, Haude D, Foster T, Morgenstern M and Wiesendanger R 2004 A 300 mK ultra-high vacuum scanning tunneling microscope for spin-resolved spectroscopy at high energy resolution *Rev. Sci. Instrum.* **75** 4871-9

[137] Grobis M, Wachowiak A, Yamachika R and Crommie M F 2005 Tuning negative differential resistance in a molecular film *Appl. Phys. Lett.* **86** 204102

[138] Joshi S, Bischoff F, Koitz R, Ecija D, Seufert K, Seitsonen A P, Hutter J, Diller K, Urgel J I, Sachdev H, Barth J V and Auwarter W 2014 Control of molecular organization and energy level alignment by an electronically nanopatterned boron nitride template *ACS Nano* **8** 430-42

[139] Franke K J, Schulze G, Henningsen N, Fernandez-Torrente I, Pascual J I, Zarwell S, Ruck-Braun K, Cobian M and Lorente N 2008 Reducing the molecule-substrate coupling in C60-based nanostructures by molecular interactions *Phys. Rev. Lett.* **100** 036807

[140] Kamlapure A, Saraswat G, Ganguli S C, Bagwe V, Raychaudhuri P and Pai S P 2013 A 350 mK, 9 T scanning tunneling microscope for the study of superconducting thin films on insulating substrates and single crystals *Rev. Sci. Instrum.* **84** 123905

[141] Dynes R C, Narayanamurti V and Garno J P 1978 Direct Measurement of Quasiparticle-Lifetime Broadening in a Strong-Coupled Superconductor *Phys. Rev. Lett.* **41** 1509-12

[142] Fischer Ø, Kugler M, Maggio-Aprile I, Berthod C and Renner C 2007 Scanning tunneling spectroscopy of high-temperature superconductors *Rev. Mod. Phy.* **79** 353-419

[143] Abrikosov A A 1957 The magnetic properties of superconducting alloys *J. Phys. Chem.Solids* **2** 199-208

[144] Hess H F, Robinson R B, Dynes R C, Valles J M, Jr. and Waszczak J V 1989 Scanning-tunneling-microscope observation of the Abrikosov flux lattice and the density of states near and inside a fluxoid *Phys. Rev. Lett.* **62** 214-6

[145] Overhauser A W and Daemen L L 1989 Zero-bias tunneling anomaly at a vortex core *Phys. Rev. Lett.* **62** 1691-3

[146] Caroli C, De Gennes P G and Matricon J 1964 Bound Fermion states on a vortex line in a type II superconductor *Phys. Lett.* **9** 307-9

[147] Zhang Y M, Fan J Q, Wang W L, Zhang D, Wang L L, Li W, He K, Song C L, Ma X C and Xue Q K 2018 Observation of interface superconductivity in a $SnSe_2$/epitaxial graphene van der Waals heterostructure *Phys. Rev. B* **98** 220508(R)

[148] Holm R and Meissner W 1932 Messungen mit Hilfe von flssigem Helium. XIII *Z. Phys.* **74** 715-35

[149] Hohenberg P and Kohn W 1964 Inhomogeneous Electron Gas *Phys. Rev.* **136** B864-B71

[150] Kohn W and Sham L J 1965 Self-Consistent Equations Including Exchange and Correlation Effects *Phys. Rev.* **140** A1133-A8

[151] Perdew J P, Burke K and Ernzerhof M 1996 Generalized Gradient Approximation Made Simple *Phys. Rev. Lett.* **77** 3865-8

[152] Grimme S, Ehrlich S and Goerigk L 2011 Effect of the Damping Function in Dispersion Corrected Density Functional Theory *J. Comput. Chem.* **32** 1456-65

[153] Zhang Y K and Yang W T 1998 Comment on "Generalized gradient approximation made simple" *Phys. Rev. Lett.* **80** 890

[154] Becke A D 1993 A new mixing of Hartree–Fock and local density-functional theories *J. Chem. Phys.* **98** 1372-7

[155] Kim K and Jordan K D 1994 Comparison of Density Functional and MP2 Calculations on the Water Monomer and Dimer *J. Phys. Chem.* **98** 10089-94

[156] Stephens P J, Devlin F J, Chabalowski C F and Frisch M J 1994 Ab Initio Calculation of Vibrational Absorption and Circular Dichroism Spectra Using Density Functional Force Fields *J. Phys. Chem.* **98** 11623-7

[157] Kresse G and Furthmuller J 1996 Efficient iterative schemes for ab initio total-energy calculations using a plane-wave basis set *Phys. Rev. B Condens. Matter* **54** 11169-86

[158] Blochl P E 1994 Projector augmented-wave method *Phys. Rev. B Condens. Matter* **50** 17953-79

[159] Grimme S, Antony J, Ehrlich S and Krieg H 2010 A consistent and accurate ab initio parametrization of density functional dispersion correction (DFT-D) for the 94 elements H-Pu *J. Chem. Phys.* **132** 154104

[160] VandeVondele J, Krack M, Mohamed F, Parrinello M, Chassaing T and Hutter J 2005 QUICKSTEP: Fast and accurate density functional calculations using a mixed Gaussian and plane waves approach *Comput. Phys. Commun.* **167** 103-28

[161] Hutter J, Iannuzzi M, Schiffmann F and VandeVondele J 2014 CP2K: atomistic simulations of condensed matter systems *Wiley Interdiscip. Rev.-Comput. Mol. Sci.* **4** 15-25

[162] Goedecker S, Teter M and Hutter J 1996 Separable dual-space Gaussian pseudopotentials *Phys. Rev. B* **54** 1703-10

[163] Krack M 2005 Pseudopotentials for H to Kr optimized for gradient-corrected exchange-correlation functionals *Theor. Chem. Acc.* **114** 145-52

[164] VandeVondele J and Hutter J 2007 Gaussian basis sets for accurate calculations on molecular systems in gas and condensed phases *J. Chem. Phys.* **127** 114105

[165] Momma K and Izumi F 2011 VESTA 3for three-dimensional visualization of crystal, volumetric and morphology data *J. Appl. Crystallogr.* **44** 1272-6

[166] Choudhuri I, Bhauriyal P and Pathak B 2019 Recent Advances in Graphene-like 2D Materials for Spintronics Applications *Chem. Mater.* **31** 8260-85

[167] Rasmussen F A and Thygesen K S 2015 Computational 2D Materials Database: Electronic Structure of Transition-Metal Dichalcogenides and Oxides *J. Phys. Chem. C* **119** 13169-83

[168] Novoselov K S, Mishchenko A, Carvalho A and Castro Neto A H 2016 2D materials and van der Waals heterostructures *Science* **353** aac9439

[169] Ge J F, Liu Z L, Liu C, Gao C L, Qian D, Xue Q K, Liu Y and Jia J F 2015 Superconductivity above 100 K in single-layer FeSe films on doped SrTiO3 *Nat. Mater.* **14** 285-9

[170] Yin X, Tang C S, Wu D, Kong W, Li C, Wang Q, Cao L, Yang M, Chang Y H, Qi D, Ouyang F, Pennycook S J, Feng Y P, Breese M B H, Wang S J, Zhang W, Rusydi A and Wee A T S 2019 Unraveling High-Yield Phase-Transition Dynamics in Transition Metal Dichalcogenides on Metallic Substrates *Adv. Sci.* **6** 1802093

[171] Dong X, Lai W and Zhang P 2021 Semiconductor to topological insulator transition induced by stress propagation in metal dichalcogenide core–shell lateral heterostructures *Mater. Horiz.* **8** 1029-36

[172] Bae S H, Lu K, Han Y, Kim S, Qiao K, Choi C, Nie Y, Kim H, Kum H S, Chen P, Kong W, Kang B S, Kim C, Lee J, Baek Y, Shim J, Park J, Joo M, Muller D A, Lee K and Kim J 2020 Graphene-assisted spontaneous relaxation towards dislocation-free heteroepitaxy *Nat. Nanotechnol.* **15** 272-6

[173] Raynor G V and Smith R W 1958 The Transition Temperature of the Transition between Grey and White Tin *Proc. R. Soc. Lon. Ser.-A* **244** 101-9

[174] Shao Z B, Zhang Z Y, Yuan H, Sun H G, Cao Y, Zhang X, Li S J, Gedeon H, Xiang T, Xue Q K and Pan M H 2018 Scanning tunneling microscopic observation of enhanced superconductivity in epitaxial Sn islands grown on $SrTiO_3$ substrate *Sci. Bull.* **63** 1332-7

[175] Barfuss A, Dudy L, Scholz M R, Roth H, Hopfner P, Blumenstein C, Landolt G, Dil J H, Plumb N C, Radovic M, Bostwick A, Rotenberg E, Fleszar A, Bihlmayer G, Wortmann D, Li G, Hanke W, Claessen R and Schafer J 2013 Elemental topological insulator with tunable Fermi level: strained alpha-Sn on InSb(001) *Phys. Rev. Lett.* **111** 157205

[176] Xu C Z, Chan Y H, Chen Y G, Chen P, Wang X X, Dejoie C, Wong M H, Hlevyack J A, Ryu H J, Kee H Y, Tamura N, Chou M Y, Hussain Z, Mo S K and Chiang T C 2017 Elemental Topological Dirac Semimetal: alpha-Sn on InSb(111) *Phys. Rev. Lett.* **118** 146402

[177] Falson J, Xu Y, Liao M, Zang Y, Zhu K, Wang C, Zhang Z, Liu H, Duan W, He K, Liu H, Smet J H, Zhang D and Xue Q K 2020 Type-II Ising pairing in few-layer stanene *Science* **367** 1454-7

[178] Zhao C, Qin J, Xia B, Yang B, Zheng H, Wang S, Liu C, Li Y, Guan D and Jia J 2020 Combining quantum spin hall effect and superconductivity in few-layer stanene *arXiv:2006.09834v1* arXiv.org e-Print archive. https://arxiv.org/abs/2006.09834 (accessed April 19, 2021)

[179] Zhang R W, Ji W X, Zhang C W, Li P and Wang P J 2016 Prediction of flatness-driven quantum spin Hall effect in functionalized germanene and stanene *Phys Chem Chem Phys* **18** 28134-9

[180] Xu C Z, Chan Y H, Chen P, Wang X X, Flototto D, Hlevyack J A, Bian G, Mo S K, Chou M Y and Chiang T C 2018 Gapped electronic structure of epitaxial stanene on InSb(111) *Phys. Rev. B* **97** 035122

[181] Zheng X H, Zhang J F, Tong B and Du R R 2019 Epitaxial growth and electronic properties of few-layer stanene on InSb (111) *2d Mater.* **7** 011001

[182] Dong X, Zhang L, Yoon M and Zhang P 2021 The role of substrate on stabilizing new phases of two-dimensional tin *2D Mater.* **8** 045003

[183] Schulz F, Liljeroth P and Seitsonen A P 2019 Benchmarking van der Waals-treated DFT: The case of hexagonal boron nitride and graphene on Ir(111) *Phy. Rev. Mater.* **3** 084001

[184] Meng L, Wang Y L, Zhang L Z, Du S X, Wu R T, Li L F, Zhang Y, Li G, Zhou H T, Hofer W A and Gao H J 2013 Buckled Silicene Formation on Ir(111) *Nano Lett.* **13** 685-90

[185] Qian G-R, Dong X, Zhou X-F, Tian Y, Oganov A R and Wang H-T 2013 Variable cell nudged elastic band method for studying solid–solid structural phase transitions *Comput. Phys. Commun.* **184** 2111-8

[186] Zhang C, Chen Y, Johnson A, Li M Y, Li L J, Mende P C, Feenstra R M and Shih C K 2015 Probing Critical Point Energies of Transition Metal Dichalcogenides: Surprising Indirect Gap of Single Layer WSe2 *Nano Lett.* **15** 6494-500

[187] Zeng M, Xiao Y, Liu J, Yang K and Fu L 2018 Exploring Two-Dimensional Materials toward the Next-Generation Circuits: From Monomer Design to Assembly Control *Chem. Rev.* **118** 6236-96

[188] Bae S H, Kum H, Kong W, Kim Y, Choi C, Lee B, Lin P, Park Y and Kim J 2019 Integration of bulk materials with two-dimensional materials for physical coupling and applications *Nat. Mater.* **18** 550-60

[189] Zhao A L, Li H, Hu X J, Wang C, Zhang H, Lu J G, Ruan S C and Zeng Y J 2020 Review of 2D group VA material-based heterostructures *J. Phys. D Appl. Phys.* **53** 293002

[190] Neupane G P, Zhou K, Chen S S, Yildirim T, Zhang P X and Lu Y R 2019 In-Plane Isotropic/Anisotropic 2D van der Waals Heterostructures for Future Devices *Small* **15** 1804733

[191] Sokolikova M S, Sherrell P C, Palczynski P, Bemmer V L and Mattevi C 2019 Direct solution-phase synthesis of 1T' WSe2 nanosheets *Nat. Commun.* **10** 712

[192] Apte A, Kochat V, Rajak P, Krishnamoorthy A, Manimunda P, Hachtel J A, Idrobo J C, Syed Amanulla S A, Vashishta P, Nakano A, Kalia R K, Tiwary C S and Ajayan P M 2018

Structural Phase Transformation in Strained Monolayer $MoWSe_2$ Alloy *ACS Nano* **12** 3468-76

[193] Ma Y, Liu B, Zhang A, Chen L, Fathi M, Shen C, Abbas A N, Ge M, Mecklenburg M and Zhou C 2015 Reversible Semiconducting-to-Metallic Phase Transition in Chemical Vapor Deposition Grown Monolayer WSe_2 and Applications for Devices *ACS Nano* **9** 7383-91

[194] Liu L W, Ge Z Z, Yan C H, Moghadam A D, Weinert M and Li L 2018 Termination-dependent edge states of MBE-grown WSe_2 *Phys. Rev. B* **98** 235304

[195] Shao Z B, Fu Z G, Li S J, Cao Y, Bian Q, Sun H G, Zhang Z Y, Gedeon H, Zhang X, Liu L J, Cheng Z W, Zheng F W, Zhang P and Pan M H 2019 Strongly Compressed Few-Layered $SnSe_2$ Films Grown on a $SrTiO_3$ Substrate: The Coexistence of Charge Ordering and Enhanced Interfacial Superconductivity *Nano Lett.* **19** 5304-12

[196] Le Quang T, Cherkez V, Nogajewski K, Potemski M, Dau M T, Jamet M, Mallet P and Veuillen J Y 2017 Scanning tunneling spectroscopy of van der Waals graphene/semiconductor interfaces: absence of Fermi level pinning *2D Mater.* **4** 035019

[197] Voiry D, Mohite A and Chhowalla M 2015 Phase engineering of transition metal dichalcogenides *Chem. Soc. Rev.* **44** 2702-12

[198] Wang Y, Xiao J, Zhu H Y, Li Y, Alsaid Y, Fong K Y, Zhou Y, Wang S Q, Shi W, Wang Y, Zettl A, Reed E J and Zhang X 2017 Structural phase transition in monolayer $MoTe_2$ driven by electrostatic doping *Nature* **550** 487–91

[199] Hsu W T, Lu L S, Wang D, Huang J K, Li M Y, Chang T R, Chou Y C, Juang Z Y, Jeng H T, Li L J and Chang W H 2017 Evidence of indirect gap in monolayer WSe_2 *Nat. Commun.* **8** 929

[200] Hanbicki A T, Currie M, Kioseoglou G, Friedman A L and Jonker B T 2015 Measurement of high exciton binding energy in the monolayer transition-metal dichalcogenides WS_2 and WSe2 *Solid State Commun.* **203** 16-20

[201] Liu H J, Jiao L, Xie L, Yang F, Chen J L, Ho W K, Gao C L, Jia J F, Cui X D and Xie M H 2015 Molecular-beam epitaxy of monolayer and bilayer WSe2: a scanning tunneling microscopy/spectroscopy study and deduction of exciton binding energy *2D Mater.* **2** 034004

[202] Shimada T, Ohuchi F S and Parkinson B A 1994 Work Function and Photothreshold of Layered Metal Dichalcogenides *Jpn J. Appl. Phys. 1* **33** 2696-8

[203] Wang S S, Rong Y M, Fan Y, Pacios M, Bhaskaran H, He K and Warner J H 2014 Shape Evolution of Monolayer MoS_2 Crystals Grown by Chemical Vapor Deposition *Chem. of Mater.* **26** 6371-9

[204] Liu H, Lazzaroni P and Di Valentin C 2018 Nature of Excitons in Bidimensional WSe_2 by Hybrid Density Functional Theory Calculations *Nanomaterials (Basel)* **8** 481

[205] Gonzalez J M and Oleynik I I 2016 Layer-dependent properties of SnS_2 and $SnSe_2$ two-dimensional materials *Phys. Rev. B* **94** 125443

[206] Qian X, Liu J, Fu L and Li J 2014 Solid state theory. Quantum spin Hall effect in two-dimensional transition metal dichalcogenides *Science* **346** 1344-7

[207] Nayak A P, Pandey T, Voiry D, Liu J, Moran S T, Sharma A, Tan C, Chen C H, Li L J, Chhowalla M, Lin J F, Singh A K and Akinwande D 2015 Pressure-dependent optical and vibrational properties of monolayer molybdenum disulfide *Nano Lett.* **15** 346-53

[208] Kretschmer S, Komsa H P, Boggild P and Krasheninnikov A V 2017 Structural Transformations in Two-Dimensional Transition-Metal Dichalcogenide MoS_2 under an Electron Beam: Insights from First-Principles Calculations *J. Phys. Chem. Lett.* **8** 3061-7

[209] Song S, Keum D H, Cho S, Perello D, Kim Y and Lee Y H 2016 Room Temperature Semiconductor-Metal Transition of MoTe2 Thin Films Engineered by Strain *Nano Lett.* **16** 188-93

[210] Lin Y C, Dumcenco D O, Huang Y S and Suenaga K 2014 Atomic mechanism of the semiconducting-to-metallic phase transition in single-layered MoS_2 *Nat. Nanotechnol.* **9** 391-6

[211] Fang Y Q, Dong Q, Pan J, Liu H Y, Liu P, Sun Y Y, Li Q J, Zhao W, Liu B B and Huang F Q 2019 Observation of superconductivity in pressurized 2M WSe_2 crystals *J. Mater. Chem. C* **7** 8551-5

[212] Li H, Li Y, Aljarb A, Shi Y and Li L J 2018 Epitaxial Growth of Two-Dimensional Layered Transition-Metal Dichalcogenides: Growth Mechanism, Controllability, and Scalability *Chem. Rev.* **118** 6134-50

[213] Fei Z Y, Palomaki T, Wu S F, Zhao W J, Cai X H, Sun B S, Nguyen P, Finney J, Xu X D and Cobden D H 2017 Edge conduction in monolayer WTe_2 *Nat. Phys.* **13** 677–82

[214] Dong X, Hu Y, Ren S and Zhang P 2020 Spatially Resolved Investigation of Mixed Valence and Insulator-to-Metal Transition in an Organic Salt *J. Phys. Chem. Lett.* **11** 8352-7

[215] Pham V D, Ghosh S, Joucken F, Pelaez-Fernandez M, Repain V, Chacon C, Bellec A, Girard Y, Sporken R, Rousset S, Dappe Y J, Narasimhan S and Lagoute J 2019 Selective control of molecule charge state on graphene using tip-induced electric field and nitrogen doping *Npj 2d Mater. Appl.* **3** 5

[216] Pia A D, Lisi S, Luca O, Warr D A, Lawrence J, Otrokov M M, Aliev Z S, Chulkov E V, Agostino R G, Arnau A, Papagno M and Costantini G 2018 TCNQ Physisorption on the Topological Insulator Bi2 Se3 *Chemphyschem* **19** 2405-10

[217] Fernández-Torrente I, Franke K J and Pascual J I 2008 Structure and electronic configuration of tetracyanoquinodimethane layers on a Au(1 1 1) surface *Int. J. Mass. Spectrom.* 269–73

[218] Franke K J, Schulze G, Henningsen N, Fernandez-Torrente I, Pascual J I, Zarwell S, Ruck-Braun K, Cobian M and Lorente N 2008 Reducing the molecule-substrate coupling in C(60)-based nanostructures by molecular interactions *Phys. Rev. Lett.* **100** 036807

[219] Wickenburg S, Lu J, Lischner J, Tsai H Z, Omrani A A, Riss A, Karrasch C, Bradley A, Jung H S, Khajeh R, Wong D, Watanabe K, Taniguchi T, Zettl A, Neto A H C, Louie S G and Crommie M F 2016 Tuning charge and correlation effects for a single molecule on a graphene device *Nat. Commun.* **7** 13553

[220] Pradhan N A, Liu N, Silien C and Ho W 2005 Atomic scale conductance induced by single impurity charging *Phys. Rev. Lett.* **94** 076801

[221] Fernandez-Torrente I, Kreikemeyer-Lorenzo D, Strozecka A, Franke K J and Pascual J I 2012 Gating the Charge State of Single Molecules by Local Electric Fields *Phys. Rev. Lett.* **108** 036801

[222] Brar V W, Decker R, Solowan H M, Wang Y, Maserati L, Chan K T, Lee H, Girit C O, Zettl A, Louie S G, Cohen M L and Crommie M F 2011 Gate-controlled ionization and screening of cobalt adatoms on a graphene surface *Nat. Phys.* **7** 43-7

[223] Wu S W, Nazin G V, Chen X, Qiu X H and Ho W 2004 Control of relative tunneling rates in single molecule bipolar electron transport *Phys. Rev. Lett.* **93** 236802

[224] Blowey P J, Rochford L A, Duncan D A, Warr D A, Lee T L, Woodruff D P and Costantini G 2017 Probing the interplay between geometric and electronic structure in a two-dimensional K-TCNQ charge transfer network *Faraday Discuss.* **204** 97-110

[225] Jonkman H T and Kommandeur J 1972 Uv Spectra and Their Calculation of Tcnq and Its Monovalent and Divalent Anion *Chem. Phys. Lett.* **15** 496

[226] Vegter J G and Kommandeur J 1974 Properties of Simple Alkali-Tetracyanoquinodimethan (Tcnq) Salts .2. Optical-Properties of M+Tcnq- Salts *Phys. Rev. B* **9** 5150-4

[227] Umbach T R, Fernandez-Torrente I, Ruby M, Schulz F, Lotze C, Rurali R, Persson M, Pascual J I and Franke K J 2013 Atypical charge redistribution over a charge-transfer monolayer on a metal *New J. Phy.* **15** 083048

[228] Hu Y, Adhikari D, Tan A, Dong X, Zhu T, Wang X, Mitchell T, Yao Z, Dias R P, Kim R, Ali A H, Zhang J, Huang Y, Hu F, Yang R, Li Z, Armstrong J N, Wang J, M. Liu J B, Zurek E, Ganapathy S, Grossman J C, Zhang P P and Ren S 2020 Laser-induced cooperative transition in molecular electronic crystal *Submitted*

[229] Potember R S, Poehler T O and Cowan D O 1979 Electrical Switching and Memory Phenomena in Cu-Tcnq Thin-Films *Appl. Phys. Lett.* **34** 405-7

[230] Oyamada T, Tanaka H, Matsushige K, Sasabe H and Adachi C 2003 Switching effect in Cu : TCNQ charge transfer-complex thin films by vacuum codeposition *Appl. Phys. Lett.* **83** 1252-4

[231] Hoagland J J, Wang X D and Hipps K W 1993 Characterization of Cu-Cutcnq-M Devices Using Scanning Electron-Microscopy and Scanning Tunneling Microscopy *Chem. Mater.* **5** 54-60

[232] Sakamoto T, Sunamura H, Kawaura H, Hasegawa T, Nakayama T and Aono M 2003 Nanometer-scale switches using copper sulfide *Appl. Phys. Lett.* **82** 3032-4

[233] Gu Z Z, Wu H M, Wei Y and Liu J Z 1993 Mechanism Generating Switching Effects in Cu-Tcnq and Ag-Tcnq Films *J. Phys. Chem.-Us* **97** 2543-5

[234] Pustogow A, McLeod A S, Saito Y, Basov D N and Dressel M 2018 Internal strain tunes electronic correlations on the nanoscale *Sci. Adv.* **4** eaau9123

[235] Zhou Y, Zhang B, Chen X, Gu C, An C, Zhou Y, Cai K, Yuan Y, Chen C, Wu H, Zhang R, Park C, Xiong Y, Zhang X, Wang K and Yang Z 2018 Pressure-Induced Metallization and Robust Superconductivity in Pristine 1T-SnSe2 *Adv. Electron. Mater.* **4** 1800155

[236] Zeng J W, Liu E, Fu Y J, Chen Z Y, Pan C, Wang C Y, Wang M, Wang Y J, Xu K, Cai S H, Yan X X, Wang Y, Liu X W, Wang P, Liang S J, Cui Y, Hwang H Y, Yuan H T and Miao F 2018 Gate-Induced Interfacial Superconductivity in 1T-$SnSe_2$ *Nano Lett.* **18** 1410-5

[237] Song Y P, Liang X W, Guo J G, Deng J, Gao G Y and Chen X L 2019 Superconductivity in Li-intercalated 1T-$SnSe_2$ driven by electric field gating *Phy. Rev. Mater.* **3** 054804

[238] Wang S Z, Zhang Y M, Fan J Q, Ren M Q, Song C L, Ma X C and Xue Q K 2020 Charge density waves and Fermi level pinning in monolayer and bilayer $SnSe_2$ *Phys. Rev. B* **102** 241408(R)

[239] Mao Y H, Ma X C, Wu D X, Lin C, Shan H, Wu X J, Zhao J, Zhao A D and Wang B 2020 Interfacial Polarons in van der Waals Heterojunction of Monolayer $SnSe_2$ on $SrTiO_3$ (001) *Nano Lett.* **20** 8067-73

[240] Walker S M, de la Torre A, Bruno F Y, Tamai A, Kim T K, Hoesch M, Shi M, Bahramy M S, King P D and Baumberger F 2014 Control of a two-dimensional electron gas on $SrTiO_3$(111) by atomic oxygen *Phys. Rev. Lett.* **113** 177601

[241] Biswas A, Rossen P B, Yang C H, Siemons W, Jung M H, Yang I K, Ramesh R and Jeong Y H 2011 Universal Ti-rich termination of atomically flat $SrTiO_3$ (001), (110), and (111) surfaces *Appl. Phys. Lett.* **98** 051904

[242] Kawasaki M, Takahashi K, Maeda T, Tsuchiya R, Shinohara M, Ishiyama O, Yonezawa T, Yoshimoto M and Koinuma H 1994 Atomic Control of the $SrTiO_3$ Crystal Surface *Science* **266** 1540-2

[243] Koster G, Kropman B L, Rijnders G J H M, Blank D H A and Rogalla H 1998 Quasi-ideal strontium titanate crystal surfaces through formation of strontium hydroxide *Appl. Phys. Lett.* **73** 2920-2

[244] Noguera C 2000 Polar oxide surfaces *J. Phys.Condense. Matter* **12** R367-R410

[245] Russell B C and Castell M R 2007 (13×13)R13.9°and(7×7)R19.1°reconstructions of the polar$SrTiO_3$(111)surface *Phys. Rev. B* **75** 155433

[246] Russell B C and Castell M R 2008 Surface of Sputtered and Annealed Polar $SrTiO_3$(111): TiO_x-Rich (n × n) Reconstructions *J. Phys. Chem. C* **112** 6538-45

[247] Marks L D, Chiaramonti A N, Rahman S U and Castell M R 2015 Transition from Order to Configurational Disorder for Surface Reconstructions on $SrTiO_3$(111) *Phys. Rev. Lett.* **114** 226101

[248] Feng J, Zhu X and Guo J 2013 Reconstructions on $SrTiO_3$(111) surface tuned by Ti/Sr deposition *Surf. Sci.* **614** 38-45

[249] Torrelles X, Cantele G, De Luca G M, Di Capua R, Drnec J, Felici R, Ninno D, Herranz G and Salluzzo M 2019 Electronic and structural reconstructions of the polar (111) $SrTiO_3$ surface *Phys. Rev. B* **99** 205421

[250] Riva M, Franceschi G, Schmid M and Diebold U 2019 Epitaxial growth of complex oxide films: Role of surface reconstructions *Phys. Rev. Res.* **1** 033059

[251] Goniakowski J, Finocchi F and Noguera C 2008 Polarity of oxide surfaces and nanostructures *Rep. Prog. Phys.* **71** 016501

[252] Salluzzo M, Gariglio S, Torrelles X, Ristic Z, Di Capua R, Drnec J, Sala M M, Ghiringhelli G, Felici R and Brookes N B 2013 Structural and electronic reconstructions at the $LaAlO_3$/$SrTiO_3$ interface *Adv. Mater.* **25** 2333-8

[253] Liang Y, Wang Y, Liu L, Guo Q, Wang W, Yang H and Guo J 2018 Chemical intermixing at oxide heterointerfaces with polar discontinuity *Appl. Phys. Lett.* **112** 231601

[254] Walker S M, Bruno F Y, Wang Z, de la Torre A, Ricco S, Tamai A, Kim T K, Hoesch M, Shi M, Bahramy M S, King P D and Baumberger F 2015 Carrier-Density Control of the $SrTiO_3$(001) Surface 2D Electron Gas studied by ARPES *Adv. Mater.* **27** 3894-9

[255] Vlachos D, Kamaratos M, Foulias S D, Argirusis C and Borchardt G 2004 Ni ultrathin film development on $SrTiO_3$(100) surface *Surf. Sci.* **550** 213-22

[256] Zagonel L F, Baeurer M, Bailly A, Renault O, Hoffmann M, Shih S J, Cockayne D and Barrett N 2009 Orientation-dependent work function of in situ annealed strontium titanate *J. Phys.-Condens. Mat.* **21** 314013

[257] Ma T Y, Jacobs R, Booske J and Morgan D 2020 Understanding the interplay of surface structure and work function in oxides: A case study on $SrTiO_3$ *Apl. Mater.* **8** 071110

[258] Dong X, Yan C, Tomer D, Li C H and Li L 2016 Spiral growth of few-layer MoS2 by chemical vapor deposition *Appl. Phys. Lett.* **109** 051604

[259] Zhang Y, Yao Y Y, Sendeku M G, Yin L, Zhan X Y, Wang F, Wang Z X and He J 2019 Recent Progress in CVD Growth of 2D Transition Metal Dichalcogenides and Related Heterostructures *Adv. Mater.* **31** 1901694

[260] Lasek K, Li J, Kolekar S, Coelho P M, Guo L a, Zhang M, Wang Z and Batzill M 2021 Synthesis and characterization of 2D transition metal dichalcogenides: Recent progress from a vacuum surface science perspective *Surf. Sci. Rep.* **76** 100523

[261] Choi W, Choudhary N, Han G H, Park J, Akinwande D and Lee Y H 2017 Recent development of two-dimensional transition metal dichalcogenides and their applications *Mater. Today* **20** 116-30

[262] Seyler K L, Zhong D, Huang B, Linpeng X, Wilson N P, Taniguchi T, Watanabe K, Yao W, Xiao D, McGuire M A, Fu K C and Xu X 2018 Valley Manipulation by Optically Tuning the Magnetic Proximity Effect in WSe_2/CrI_3 Heterostructures *Nano Lett.* **18** 3823-8

[263] Noland J A 1954 Optical Absorption of Single-Crystal Strontium Titanate *Phys. Rev.* **94** 724

[264] Sitaputra W, Sivadas N, Skowronski M, Xiao D and Feenstra R M 2015 Oxygen vacancies on SrO-terminated$SrTiO_3$(001)surfaces studied by scanning tunneling spectroscopy *Phys. Rev. B* **91** 205408

[265] Wu J, Hu Z, Jin Z, Lei S, Guo H, Chatterjee K, Zhang J, Yang Y, Li B, Liu Y, Lai J, Vajtai R, Yakobson B, Tang M, Lou J and Ajayan P M 2016 Spiral Growth of $SnSe_2$ Crystals by Chemical Vapor Deposition *Adv. Mater. Interfaces* **3** 1600383

[266] Javed Y, Mirza S M and Rafiq M A 2021 Effect of Pressure on Mechanical and Thermal Properties of $SnSe_2$ *Int. J. Thermophys.* **42** 146

[267] Yan R, Zhang Q, Li W, Calizo I, Shen T, Richter C A, Hight-Walker A R, Liang X, Seabaugh A, Jena D, Grace Xing H, Gundlach D J and Nguyen N V 2012 Determination of graphene work function and graphene-insulator-semiconductor band alignment by internal photoemission spectroscopy *Appl. Phys. Lett.* **101** 022105

[268] Lei B, Pan Y, Hu Z, Zhang J, Xiang D, Zheng Y, Guo R, Han C, Wang L, Lu J, Yang L and Chen W 2018 Direct Observation of Semiconductor-Metal Phase Transition in Bilayer

Tungsten Diselenide Induced by Potassium Surface Functionalization *ACS Nano* **12** 2070-7